Precision Quantum Chemistry via Full Configuration Interaction and Slater Basis Sets

by

Alexander Stark

A dissertation submitted in partial fulfillment
of the requirements for the degree of
Doctor of Philosophy
(Chemistry and Scientific Computing)
in the University of Michigan
2026

Doctoral Committee:

Professor Paul M. Zimmerman, Chair
Professor Eitan Geva
Professor Theodore Goodson III
Professor John Kieffer

Alexander Stark

alstark@umich.edu

ORCID iD: 0000-0002-6830-2713

© Alexander Stark 2026

Dedication

This dissertation is dedicated to Kat who has always been there for me throughout my graduate school experience. As well as my friends and family who have also provided much love and support.

"People think of education as something they can finish"

-Issac Asimov

Acknowledgements

I would like to thank all of the people who have provided me mentorship, opportunities, and companionship throughout my time in graduate school. First, I would like to personally thank Paul Zimmerman for being and excellent mentor, his guidance throughout my PhD struck the perfect balance of being helpful but also challenging me so I could improve. I would also like to thank my committee members Eitan Geva, Theodore Goodson III, and John Kieffer for the insightful input they gave me at different milestones in my journey. The useful dialogue and mentorship of other members in the Zimmerman group were especially helpful in general, but also particularly from Hanjie Jiang, Khoi Dang, and Jeffrey Hatch. I would also like to thank members of the Zimmerman group with which I have become friends and enjoy casual conversation with as well such as Soumik Das, Vaibhav Khanna, Paras Boruah, Srijita Dutta, Bishnu Rakshit, and Hamidur Rahman. I would also like to thank David Braun for the continued computational cluster support.

I would like to thank the great friends I have also made from other groups such as Ryan Van Daele who has become a close friend for our philosophical dialogue, adventures, and all of the great memories we made over these 5 years. Also, Mike Gatazka for the adventures we have been on together and the games we have played together. I would also like to thank my other friends who I met a U of M and with which I have made many memories like Jake O'Hara, Rebecca Parham, Rebecca Dawley, Katie Kolozsvari, Ian Bain, and Cara Waters. I also must thank my friends from high school and my undergraduate Rocco Dishman and Ibrahim Issac for continuing to stay in touch and having many thought-provoking conversations.

Last but not least, I would like to thank my partner Kat Fraus for supporting me through the toughest times throughout my journey. Also, my prospective in-laws Sarah, Bob, Caroline, and Nick, my brother Johnathan Stark and my parents Carla and Rogelio Saavedra. Thank you all for the love and support you have shown me.

Table of Contents

Dedication ii

Acknowledgements iii

List of Tables vii

List of Figures ix

List of Appendices xiii

Abstract xiv

Chapter 1 Introduction 1

1.1 Electronic Structure Theory 1

1.1.1 The Schrödinger Equation and Born-Oppenheimer Approximation 1

1.1.2 Basis Sets and Molecular Orbitals 2

1.1.3 Pauli Exclusion and Slater Determinants 4

1.1.4 Matrix Representation of the Schrödinger Equation 4

1.1.5 Variational Principle and Electron Correlation 5

1.1.6 Relativistic Effects 6

1.2 Configuration Interaction Methods 8

1.2.1 Natural Orbitals 8

1.2.2 Full Configuration Interaction 8

1.2.3 Select Configuration Interaction 9

1.3 Density Functional Theory 10

1.3.1 Kohn-Sham Formalism 10

1.3.2 Inverse Density Functional Theory 11

1.3.3 Orbital-Averaging Inversion 12
1.4 Conclusion 13
Chapter 2 Numerical Integration of Slater Basis Functions Over Prolate Spheroidal Grids 14
2.1 Introduction 14
2.2 Theory 16
2.2.1 PS Coordinates 16
2.2.2 Treatment of a Third Center 19
2.2.3 Implementation 20
2.3 Computational Details 21
2.4 Results and Discussion 27
2.5 Conclusion 33
Chapter 3 Efficient Configuration Interaction Composite Scheme for Quantitative Thermochemistry of Transition Metal Containing Diatomics 34
3.1 Introduction 34
3.2 Theory 37
3.2.1 Variational Step 37
3.2.2 Perturbative Step 37
3.2.3 Parallelization 38
3.2.4 Bond Dissociation Energy Procedure 38
3.3 Computational Details 42
3.4 Results and Discussion 43
3.5 Conclusion 50
Chapter 4 The Kohn-Sham Potential and Bonding at a Conical Intersection 52
4.1 Introduction 52
4.2 Methods 55
4.2.1 Inversion Procedure 55

4.2.2 Theta 56
4.2.3 Methodology 57
4.2.4 Computational Details 58
4.3 Results and Discussion 58
4.3.1 H_3 58
4.3.2 NH_3 61
4.4 Conclusion 64
Chapter 5 Final Remarks 66
5.1 Conclusion 66
5.2 Future Directions 67
Appendices 69
Bibliography 95

List of Tables

Table 2.1: RMSE (Ha) of integrals for SO_2 using BP and PS integration with TZ, QZ, and 5Z basis sets. Basis sets TZ, QZ, 5Z are described in the computational details. 24

Table 2.2: Convergence of Hartree-Fock SCF runs with BP integration. Each number indicates the eigenvalue threshold needed to control numerical stability of the overlap matrix inversion. If the value is 0 (green) all threshold values tested allow for SCF convergence. Higher values indicate instability at this step, due to lower accuracy of the overlap matrix elements. Oscillatory cases (orange) oscillated around the energy obtained through the PS method with a difference less than 0.1 Ha but did not converge. Energies which varied by more than 0.1 Ha are marked in red. In comparison, PS integration converged for all cases with the smallest eigenvalue threshold. 27

Table 2.3: Heat-Bath configuration interaction (HBCI) correlation energies (Ha) for various molecules in TZ, QZ, and 5Z basis sets. 30

Table 2.4: Two states of CH_2 ($^1A_1$ and $^3B_1$), at various correlated levels of theory. Geometries for $^1A_1$ and $^3B_1$ CH_2 were obtained from ref. 141 The bases used for the GTO calculations are the cc-pVXZ basis sets, while the STO bases are the same as referenced in Table 2.2. The energy reported under CBS was obtained in the complete basis set limit. Units are in kcal/mol. 31

Table 3.1: The percentage of total configurations which contribute to the wavefunction are given for different basis sets and numbers of frozen electrons. The ScH(val) was run in the cc-pVQZ basis with the valence electrons unfrozen. The ScH(core) was run from cc-pVDZ through cc-pVQZ with electrons down to the Ne core correlated. All HBCI calculations were run with $\varepsilon var = 1.25 \times 10 - 4$ Ha. 47

Table 3.2: Total energies, TZ, and correction contributions for the Sc and ScH systems are given in Ha. BDEs are given in the bottom half of the table (in kcal/mol), differences between the Sc and ScH corrections are also given (in kcal/mol). 49

Appendix Table A.1: Slater basis exponents for TZ, QZ, and 5Z basis functions applied to molecules in Figures 2.3, 2.4, 2.5, 2.7 and A.1 and Tables 2.1, 2.2, 2.3, and 2.4. 69

Appendix Table A.2: Geometries in Ångstrom for systems used in Figures 2.3, 2.4, 2.5, 2.7 and Tables 2.1, 2.2, and 2.3 as well as the large bond distance OF_2 structure used to obtain Figure A.1. Geometries with 3 or greater atoms were optimized using DFT with a ωB97X functional in a cc-pVQZ basis, unless specified elsewhere. The 1,3 propanediyl system was optimized with the B3LYP functional in a 6-31G* basis. 74

Appendix Table A.3: Grid sizes used for Figures 2.3 and 2.4 (left) and Figure 2.5 (right). All combinations of radial and angular number of points were considered (left). Each row of values represents parameters for a single calculation in the generation of Figure 2.5 (right). 77

Appendix Table C.1: Slater basis set exponents and associated functions for H_3 and NH_3. 84

Appendix Table C.2: Geometries for the H_3 and NH_3 systems in Å. 85

List of Figures

Figure 1.1: Comparison of Slater and Gaussian-type orbital functions, where $\xi = 1$ for the STO. 3

Figure 1.2: The relationship between relativistic and non-relativistic velocity with varying momentum. Velocity units are a fraction of the speed of light. 7

Figure 2.1: The Prolate Spheroidal grid on a cartesian grid with spheroids at constant μ (red), hyperboloids at constant ν (blue), and planes at constant ϕ (green). 18

Figure 2.2: The process of reorienting the grid around the third center, (A) is the initial spacing of the grid with the third center being located at one of the volume elements, (B) moves the μ and ν grid lines closest to the third center so that the third center coordinates align with the grid lines, and (C) splits the grid further around the third center for greater accuracy. 20

Figure 2.3: Overlap, kinetic energy, and 2-center Coulomb repulsion RMSE (Ha) analyzed for ClF and OF_2 using the PS method in a TZ basis. 22

Figure 2.4: Electron-nuclear attraction and 3-center Coulomb repulsion RMSE (Ha) analyzed for ClF and OF_2 using the PS method in a TZ basis. The grid selection and legend are the same as in Figure 2.3. 23

Figure 2.5: Comparison of the RMSE (Ha) of the electron-nuclear attraction elements for different divisions of the third center within the PS integration grid. A single split ($\$N_\{SP\} = 2\$$) gives significant advantages over no splitting, and $\$N_\{SP\} > 2\$$ gives marginal improvements. 23

Figure 2.6: Six 2-center Coulomb integrals plotted along 16 vector directions[92] as the two centers are separated. The legend indicates unit vectors for all 16 directions tested, all basis functions used have the exponent $\zeta = 1$, and all basis functions were chosen to have $m = 0$.... 24

Figure 2.7: HONO and LUNO orbitals and occupation numbers for the singlet and triplet states of 1,3-propanediyl as well as the singlet-triplet gap for the vertical excitation. iFCI uses the STO QZ basis while CCSD(T) uses a GTO basis, cc-pVQZ. 26

Figure 3.1: Process for correcting BDEs in valence calculations in a finite basis, through addition of independent semi-core and complete basis set limit corrections. 39

Figure 3.2: Process for obtaining the CBS correction, A, B and AB denote both single atoms and the diatomic. 40

Figure 3.3: Semi-core correlation extrapolation for ScH with varying ε_{var}, all points are linearly fit. 41

Figure 3.4: Process for obtaining the semi-core correction, A, B and AB denote both single atoms and the diatomic. 42

Figure 3.5: Hartree-Fock energies (Ha) for the ScH system with relativistic effects and RI approximation toggled, basis sizes ranging from DZ-QZ are evaluated. 44

Figure 3.6: Hartree-Fock MOs of the ScH system showing HOMO and HOMO-1 orbitals for 1eX2C and nonrelativistic calculations across basis sets. 45

Figure 3.7: Basis set extrapolation HBCI energies for ScH where one procedure uses the HF as reference orbitals (left) and the other uses orbitals generated via CASSCF(2,1) as reference. Both calculations are correlated to the Ne core. 46

Figure 3.8: FCI extrapolation for Sc (top) and ScH (bottom) as well as CBS extrapolation for both systems (middle). Energies are in Hartree. 48

Figure 4.1: Unit vectors with the directionality of the non-adiabatic coupling and difference gradient vectors for H_3 (top-left). Conical intersection constructed using standard model equation with three circles indicating geometries around the CI (top). Plots showing energies for H_3 geometries around a CI obtained by using equation 4.6 and setting a desired radius for the circle, here the radii are 0.1, 0.05, and 0.01Å (top-right and bottom). 56

Figure 4.2: The classical turning surface of the H_2 system as equilibrium bond distance (0.74Å) and 2 times equilibrium bond distance (1.48Å). 58

Figure 4.3: The Kohn-Sham potential for H_3 at $\theta = \frac{10\pi}{20},\frac{7\pi}{20},\frac{3\pi}{20},\frac{0\pi}{20}$ along the YZ plane in which the geometry also exists. The coorinates are in a.u. and the H_3 geometry can be found in the SI (Table C.2). 59

Figure 4.4: The first 2 Kohn-Sham orbitals obtained from the inversion procedure for the $\theta = 0$ and $\theta = \frac{\pi}{2}$ states of H_3. Isovalue of 0.05 was used and occupation numbers are given. 60

Figure 4.5: Classical turning surface for H_3, points which do not exceed a tolerance of 0.015 Ha of the ionization potential (-0.275 Ha) and points which have density greater than $1 \times 10 - 4$ are included. The coordinates are in a.u. 61

Figure 4.6: The Kohn-Sham potential for NH_3 at $\theta = \frac{10\pi}{20},\frac{7\pi}{20},\frac{3\pi}{20},\frac{0\pi}{20}$ along the YZ plane in which the geometry also exists. The coordinates are in a.u. and the NH_3 geometry can be found in the SI (Table C.2). ... 62

Figure 4.7: Kohn-Sham orbitals 3-6 obtained from the inversion procedure for the $\theta = 0$ and $\theta = \frac{\pi}{2}$ states of NH_3. The coordinates are in a.u., an isovalue of 0.05 was used and occupation numbers are given. 63

Figure 4.8: Classical turning surface for NH_3, points which do not exceed a tolerance of 0.015 Ha of the ionization potential (-0.328 Ha) and points which have density greater than 1×10^{-5} are included. The coordinates are in a.u. 63

Appendix Figure A.1: Comparison of the RMSE (Ha) of the electron-nuclear attraction elements for different divisions of the third center within the PS integration grid. Calculations performed on the OF_2 system with one OF bond as a 41.41Å distance. 78

Appendix Figure A.2: All combinations of 2-center Coulomb integrals plotted along 16 vector directions[92] as the two centers are separated. The legend indicates unit vectors for all 16 directions tested, all basis functions used have the exponent $\zeta = 1$, and all basis functions were chosen to have $m = 0$. 79

Appendix Figure A.3: FCI Extrapolation energies for methylene in the TZ, QZ, and 5Z basis for both the $^1A_1$ and $^3B_1$ states using STOs..... 80

Appendix Figure A.4: FCI Extrapolation energies for methylene in the cc-pVTZ (TZ), cc-pVQZ (QZ), and cc-pV5Z (5Z) basis for both the $^1A_1$ and $^3B_1$ states using GTOs..... 81

Appendix Figure B.1: FCI Extrapolation for neutral Sc (top) and ScH (bottom) in the cc-pwCVTZ (left) and cc-pwCVQZ (right) basis sets, energies are in Hartree. 82

Appendix Figure B.2: CBS Extrapolation for neutral Sc (left) and ScH (right) using the cc-pwCVXZ basis (X=T,Q), energies are in Hartree. 83

Appendix Figure C.1: The Kohn-Sham potential for H_3 at different theta along the YZ plane in which the geometry also exists. The coorinates are in a.u. 86

Appendix Figure C.2: The Kohn-Sham potential for NH_3 at different theta along the YZ plane in which the geometry also exists. The coordinates are in a.u. 87

Appendix Figure C.3: KSO2 for the H_3 system with varying theta..... 88

Appendix Figure C.4: KSO4 for the NH_3 system with varying theta..... 89

Appendix Figure C.5: KSO5 for the NH_3 system with varying theta..... 90

Appendix Figure C.6: KSO6 for the NH_3 system with varying theta..... 91

Appendix Figure C.7: Classical turning surface for H_3, the points are at a tolerance of 0.015 Ha of the ionization potential (-0.275 Ha) and points which density greater than 1×10^{-4} are included. The coordinates are in a.u. 92

Appendix Figure C.8: Classical turning surface for NH_3, the points are at a tolerance of 0.015 Ha of the ionization potential (-0.328 Ha) and points which density greater than 1×10^{-5} are included. The coordinates are in a.u. 93

Appendix Figure C.9: The first 3 natural orbitals obtained from HBCI for the Ψ_0 and Ψ_1 states of H_3. An isovalue of 0.05 was used and occupancies are given. 94

Appendix Figure C.10: Natural orbitals 3-7 obtained from HBCI for the Ψ_0 and Ψ_1 states of NH_3. An isovalue of 0.05 was used and occupancies are given. 94

List of Appendices

Appendix A: Supporting Information for Chapter 2 69

A.1 Slater Basis sets 69

A.2 Geometries 74

A.3 PS Grid Sizes 77

A.4 Long Bond Distance N_{SP} 78

A.5 Full 2-Center Coulomb Displacement 79

A.6 FCI Extrapolation for CH_2 in GTO and STO Basis Sets 80

Appendix B: Supplemental Information for Chapter 3 82

B.1 FCI Extrapolation cc-pwCVTZ 82

B.2 CBS Extrapolation cc-pwCVTZ 83

Appendix C: Supplemental Information for Chapter 4 84

C.1 Basis Sets 84

C.2 Geometries 85

C.3 Full Scan KS Potentials 86

C.4 Full Scan KS Orbitals 88

C.5 Full Scan Classical Turning Surfaces 92

C.6 Natural Orbitals 94

Abstract

Quantum mechanics has made possible unprecedented progress in the understanding of the underlying physics of chemical processes in the last century. In theory, the solutions to many of the most complex problems are known; in practice, however, many of these problems remain unsolved due to the necessity of theoretical approximation. This thesis investigates advancements made in the methods, and applications of said methods, to complex electronic structure problems. The first chapter includes background covering the fundamentals of quantum mechanics and introduces some important methods which are utilized in later chapters.

Chapter 2 discusses the integration of Slater functions which are notoriously difficult to integrate due to the absence of analytical expressions for some integral quantities associated with the Hamiltonian. This method utilizes advancements from SlaterGPU, a library which significantly increases the speed of grid evaluation through GPU parallelization. Hamiltonian matrix elements are integrated over in a Slater basis on a prolate spheroidal grid with three centers, which yields a ~3 order of magnitude reduced RMSE for 2-center integrals compared to the standard Becke Partitioning. With the use of the Resolution-of-the-Identity approximation we can apply this method to polyatomic systems. Results using self-consistent field and full configuration interaction wavefunctions applied to numerous 3-atom systems, as well as propanediyl, illustrate the generality of the method.

Chapter 3 details the application of a composite Heat-Bath Configuration Interaction method to the ScH system. Challenges with the incorporation of relativistic and semi-core correlation contributions were explored and found to impact CBS extrapolation convergence. As a consequence of these findings, the procedure considers semi-core and relativistic contributions to the correlation energy as separate correction terms. The RI approximation is also found to be insufficient when using the cc-pVQZ-RIFIT auxiliary basis, producing errors of ~20 mHa for ScH. The ScH bond dissociation energy is found to be 54.9 kcal/mol using the method outlined in section 3.2.4 and is within thermochemical accuracy (+/-3 kcal/mol). An alternative approach,

which directly incorporates semi-core correlation, is also applied to ScH which results in a BDE of 54.8 kcal/mol (Expt.: 55.0 kcal/mol).

Chapter 4 reveals the Kohn-Sham (KS) potential at conical intersections (CI) using an inversion procedure based on prior work by Khanna et al.[1] The dissociative nature of equilateral H_3 and NH_3 at a CI is analyzed using the KS potential, KS orbitals, and classical turning surfaces at different linear combinations of the two adiabatic states (theta). The CTS is sufficient to describe the bonding character; however, the KS orbitals provide more insight into the bonding and antibonding character which is contributed by each orbital individually. It is concluded that the CTS at a CI for certain values of theta is dissociative and looks similar to the CTS for a dissociating system away from a CI. The manner in which the KS potential changes with theta can be different between systems, where there is in-plane rotation (perpendicular to the geometric plane) of the KS potential in the H_3 system, and out-of-plane (parallel to the geometric plane) rotation of the KS potential in the NH_3 system.

Chapter 1
Introduction

In the 1920s, Erwin Schrödinger introduced wavefunctions which describe the quantum nature of reality. In modern day, Schrödinger's formulation is routinely used and, in principle, can exactly describe the electronic structure of chemical systems. In practice, however, an exact description (in a finite basis) requires a combinatorially scaling number of terms growing with system size. This thesis examines the accuracy and development of cutting-edge electronic-structure methodologies. Chapter 2 covers advances in the accuracy of Hamiltonian integral evaluation in a Slater basis set using a prolate spheroidal (PS) grid. Chapter 3 applies a composite Heat-Bath Configuration Interaction (HBCI) method to transition metal (TM) systems to obtain accurate bond dissociation energies (BDE). Chapter 4 makes use of an inverse DFT (invDFT) procedure to obtain Kohn-Sham (KS) potentials at a conical intersection, requiring the use of full configuration interaction (FCI) wavefunctions to obtain accurate densities. Before discussing the aforementioned works, we first introduce elementary aspects of electronic structure theory.[2,3]

1.1 Electronic Structure Theory

1.1.1 The Schrödinger Equation and Born-Oppenheimer Approximation

The time-independent non-relativistic Schrödinger equation, which will be referred to henceforth as the Schrödinger equation[4], is defined as

$$\widehat{H}|\Psi\rangle = E|\Psi\rangle \tag{1.1}$$

Where $\widehat{H}$ is the Hamiltonian operator, E is the observable, and $|\Psi\rangle$ is the wavefunction. This equation can be solved via the application of the Hamiltonian operator to the wavefunction to obtain the observable E. This is possible only because the state of a quantum mechanical system can be completely specified by the wavefunction. The observable E corresponds to the non-relativistic energy of a given system and can be written as the sum of kinetic and potential energies

$$\widehat{H} = -\sum_{i=1}^{N}\frac{1}{2}\nabla_i^2 - \sum_{A=1}^{M}\frac{1}{2M_A}\nabla_A^2 - \sum_{A=1}^{M}\sum_{i=1}^{N}\frac{Z_A}{r_{iA}} + \sum_{A=1}^{M}\sum_{B>A}^{M}\frac{Z_A Z_B}{r_{AB}} + \sum_{i=1}^{N}\sum_{j>i}^{N}\frac{1}{r_{ij}} \quad (1.2)$$

Where indices i,j and A,B correspond to electrons and nuclei respectively, r is the position of a particle (electron or nucleus), ∇^2 corresponds to the Laplacian, Z is the nuclear charge, and M is the ratio of the mass of nucleus A to the mass of an electron. The terms on the right-hand side of equation 1.2 can be interpreted from left to right as the electronic kinetic energy, nuclear kinetic energy, electron-nuclear attraction, nuclear-nuclear repulsion, and electron-electron repulsion. Born and Oppenheimer soon after the advent of the Schrödinger equation realized that in most cases the nuclear and electronic motion are mostly uncoupled (nuclei are ~3 orders of magnitude more massive). This allows one to rewrite equation 1.2 under the assumption that the nuclei are static, resulting in the electronic Hamiltonian.

$$\widehat{H}_{elec} = -\sum_{i=1}^{N}\frac{1}{2}\nabla_i^2 - \sum_{A=1}^{M}\sum_{i=1}^{N}\frac{Z_A}{r_{iA}} + \sum_{i=1}^{N}\sum_{j>i}^{N}\frac{1}{r_{ij}} \quad (1.3)$$

The terms which deal solely with the nuclei are removed, as the nuclear kinetic energy becomes 0 and the nuclear potential energy is constant. All methods used in this work will make use of the Born-Oppenheimer (BO) approximation.[5] In Chapter 4, conical intersections will be probed where electronic and nuclear motion become heavily coupled causing a breakdown of the BO approximation.

1.1.2 Basis Sets and Molecular Orbitals

The observable discussed in section 1.1.1 is obtained through integration of the operator over the associated basis functions it is acting on. Generic one- and two-electron integral quantities take the form

$$\int \chi_i(r_1)\hat{O}(r_1)\chi_j(r_1)dr_1 \quad (1.4)$$

$$\iint \chi_i(r_1)\chi_j(r_1)\hat{O}(r_1,r_2)\chi_k(r_2)\chi_l(r_2)dr_1dr_2 \quad (1.5)$$

Where $\hat{O}$ is a generic operator, r_1 and r_2 are the positions of electrons 1 and 2, and χ is a basis function. Atom-centered basis functions are ubiquitous in electronic structure theory as electrons are typically located in the vicinity of nuclei due to their opposing charges, with the distribution decaying radially from a nucleus (the origin). A basis that arises as a solution to the Schrödinger equation for the hydrogen atom is the Slater basis function[6]

$$\chi_{nlm}(r,\theta,\phi) = Nr^{n-1}e^{-\xi r}Y^{lm}(\theta,\phi) \tag{1.6}$$

Where N is a normalization factor, r is the radial component, θ and ϕ are angular components, ξ determines the diffuseness of the function, Y is a spherical harmonic function, and n, l, m are quantum numbers. Not all integral quantities have known analytical solutions in a Slater basis due to the cusp, so quantities are computed on a grid.[7]

To remove the cusp and obtain analytical expressions for desired integral quantities, Slater functions are usually approximated by atom-centered Gaussian functions[8] defined as

$$\chi_{nlm}(r,\theta,\phi) = Nr^{n-1}e^{-\xi r^2}Z^{lm}(r,\theta,\phi) \tag{1.7}$$

Where Z^{lm} are real solid harmonics. The exponential decay with r^2 eliminates the cusp at the nucleus, which, along with the Gaussian product rule, enables rapid evaluation of integral quantities at the cost of accuracy near the cusp and at long range.[9]

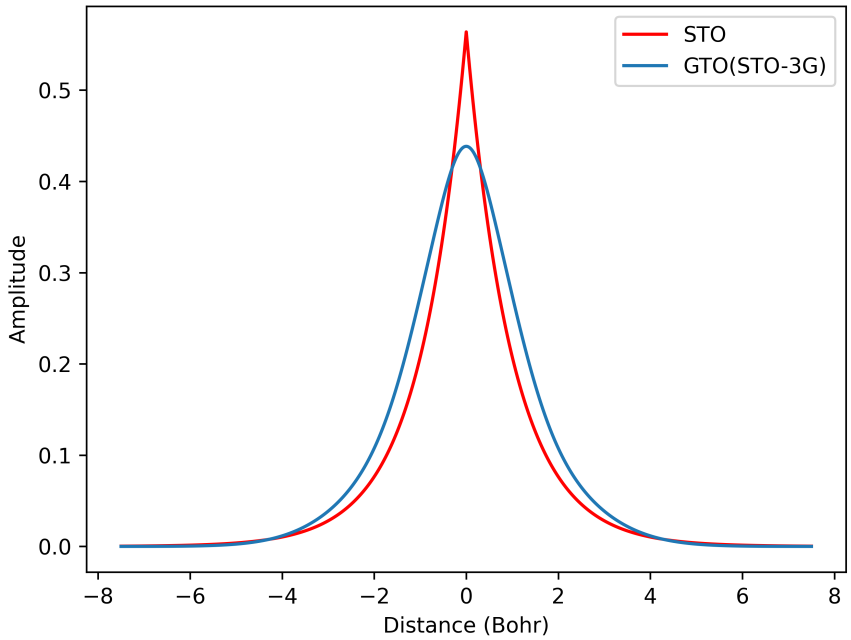

Figure 1.1: Comparison of Slater and Gaussian-type orbital functions, where $\xi = 1$ for the STO.

Figure 1.1 illustrates that Gaussian functions underestimate the cusp and decay relative to Slater functions. The desirable density produced by the STO will be of interest in Chapter 4, where accurate densities are necessary to obtain accurate exchange-correlation potentials, and Chapter 2, in which Slater functions are evaluated over a grid to assess the accuracy of the proposed integration method.

Atomic orbitals (AO) provide a sufficient electronic description for systems composed of one atom. In most chemical systems, electrons distribute throughout a molecule via bonding, which necessitates a better description of electron distribution in the form of molecular orbitals (MO). MOs can be constructed as linear combinations of AOs, providing a delocalized description.

$$\phi_\mu = \sum_i c_{i\mu}\chi_i \tag{1.8}$$

Where χ is an AO and c is an MO coefficient. MOs are widely used in electronic structure theory and can offer physical insight into the electronic structure of polyatomics. As the number of basis functions one uses increases (if done systematically while avoiding linear dependencies), so does the quality of description and the accuracy of observables.

1.1.3 Pauli Exclusion and Slater Determinants

An important postulate of quantum mechanics is the Pauli Exclusion principle, which states that a wavefunction for indistinguishable fermions must be antisymmetric with respect to exchange of any two fermions. In other words, the sign of the wavefunction will flip with the exchange of two spin orbitals. This is conveniently represented by the determinant of occupied spin orbitals or the Slater determinant[10]

$$\psi = \frac{1}{\sqrt{N!}}\begin{vmatrix} \phi_1(x_1) & \phi_2(x_1) & \cdots & \phi_N(x_1) \\ \phi_1(x_2) & \phi_2(x_2) & \cdots & \phi_N(x_2) \\ \vdots & \vdots & \ddots & \vdots \\ \phi_1(x_N) & \phi_2(x_N) & \cdots & \phi_N(x_N) \end{vmatrix} \tag{1.9}$$

Where x represents a spin and spatial component for a given electron in the spin orbital. The Slater determinant defines N electrons in N spin orbitals, properly accounting for the exchange of a particular electron configuration. When one optimizes these spin orbitals to minimize the energy this is known as self-consistent field (SCF); optimizing the ground state configuration with the Hamiltonian mentioned in section 1.1.1 is known as Hartree-Fock (HF). If M basis functions exist with N electrons, there exist 2M choose N Slater determinants, which will be shown to impact the scaling of post-HF methods.

1.1.4 Matrix Representation of the Schrödinger Equation

To solve the Schrödinger equation in practice, one can start by representing the wavefunction as a linear combination of atomic orbitals (MOs) (although this is not the only choice).

$$|\phi_\nu\rangle = \sum_j c_{j\nu}\chi_j \tag{1.10}$$

Where ν is an index over MOs and j is an index over AOs. These coefficients form a matrix describing the wavefunction, so after multiplying the Hartree-Fock equation through by $\langle\chi_i|$

$$\hat{F}|\phi_\nu\rangle = E_\nu|\phi_\nu\rangle \xrightarrow{\langle\chi_i|} \sum_j F_{ij}\, c_{j\nu} = E_\nu \sum_j S_{ij}\, c_{j\nu} \longrightarrow \boldsymbol{FC = ESC} \tag{1.11}$$

Where the overlap matrix S should be an identity matrix in an orthonormalized basis, making the expression effectively $FC = EC$. In practice, the many-body problem cannot be solved directly, and instead an optimization procedure is used where an electron is acted upon iteratively by a mean field of other electrons, which is exactly what the Fock matrix, F, represents. One can solve the Roothaan-Hall equations[11,12] (equation 1.11) until a self-consistent field (SCF) is achieved, which optimizes the orbitals in the Slater determinant, as mentioned in the previous section. A similar expression arises if one instead uses a linear combination of Slater determinants, also known as configuration state functions (CSFs), as a basis.

1.1.5 Variational Principle and Electron Correlation

The Schrödinger equation can be modified by taking the inner product of both sides; since the energy eigenvalues are scalar, we obtain the energy functional

$$E[\psi] = \frac{\langle\psi|\hat{H}|\psi\rangle}{\langle\psi|\psi\rangle} \tag{1.12}$$

If the wavefunction is perturbed by $|\delta\rangle$, and equation 1.12 is expanded in terms of this perturbation, one will find first and second order corrections to the energy. These first-order energy corrections disappear when an eigenstate of $|\psi\rangle$ coincides with an eigenstate of $|\psi\rangle + |\delta\rangle$, meaning some eigenstates correspond to stationary points on the energy surface. If we take our wavefunction as a linear combination of normalized antisymmetric N-electron functions, and subtract from both sides the ground state energy, an inequality results

$$\langle\psi|\hat{H}|\psi\rangle - E_0 = \sum_n |c_n|^2\,(E_n - E_0) \geq 0 \tag{1.13}$$

This can be interpreted as the HF energy being an upper bound to the exact energy. The HF energy can be minimized through optimization of orbitals; however, the energy can also be minimized systematically towards the exact energy via the incorporation of other electronic configurations. The variational principle then allows us to define the correlation energy as

$$E_{corr} = E_{exact} - E_{HF} \tag{1.14}$$

Two types of correlation exist, strong (static) and weak (dynamic)[13], both arising from deficiencies in the ability of the HF to describe electronic motion. Dynamic correlation results from electrons being optimized in a mean field of other electrons rather than having an expression for the electron instantaneously interacting with all others as would be the case in a real system. Static correlation arises from the consideration of only one electron configuration, when many may be required for an adequate description. Both types of correlation can be handled by including more configurations in the description of the system. Static and dynamic correlation are especially important in Chapter 3 as TM systems require adequate consideration for both types of correlation.

1.1.6 Relativistic Effects

In equations 1.2 and 1.3, the non-relativistic kinetic energy operator for electrons is given by the Laplacian, since the gradient is proportional to the momentum of an object, the classical non-relativistic kinetic energy is given as

$$T_{classical} = \frac{p^2}{2m} \tag{1.15}$$

Where p is the momentum and m is the mass. The equivalent quantum operator is

$$\hat{T}_{quantum} = \frac{\hat{p}^2}{2m} = -\frac{\hbar^2}{2m}\nabla^2 \tag{1.16}$$

When electrons travel at low velocities, the $p = mv$ approximation holds; at high velocities though, such as a core electron in a transition metal, this approximation breaks down. (Figure 1.2)

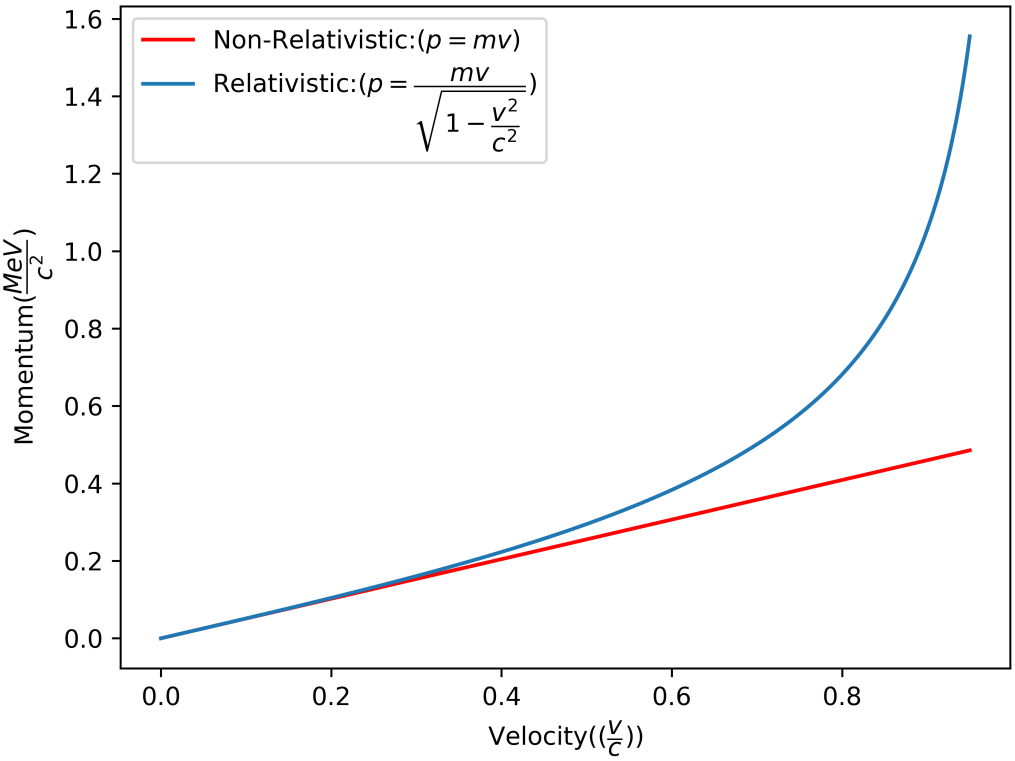

Figure 1.2: The relationship between relativistic and non-relativistic velocity with varying momentum. Velocity units are a fraction of the speed of light.

In relativistic quantum chemical calculations, the Dirac Hamiltonian[14,15] is solved, which takes into consideration positronic and electronic energy. The potential component here is V and the off-diagonal parts of the Dirac Hamiltonian represent the kinetic coupling.

$$\hat{H}_{Dirac}\begin{bmatrix}\Psi_L\\ \Psi_S\end{bmatrix} = \begin{bmatrix}V + mc^2 & c\sigma\cdot\hat{p}\\ c\sigma\cdot\hat{p} & V - mc^2\end{bmatrix}\begin{bmatrix}\Psi_L\\ \Psi_S\end{bmatrix} = E\begin{bmatrix}\Psi_L\\ \Psi_S\end{bmatrix} \tag{1.17}$$

Where V is the potential, mc^2 is the rest energy, $\hat{p}$ is the momentum, and σ are the pauli matrices. This is a 4-component matrix where Ψ_L and Ψ_S both have a spin-up and spin-down component associated with them. This increases the problem size substantially;[16] as a result, methods have been created to simplify obtaining relativistic corrections. In this vein is the exact-2-component (X2C)[17–20] method, which will be utilized in Chapter 3. X2C works by exactly relating the large and small components in a finite basis, where the wavefunction is represented by C

$$X = C_S C_L^{-1} \tag{1.18}$$

The transformation matrix X is then used to construct a unitary transformation, which is applied to the Dirac Hamiltonian, resulting in the relativistically corrected Hamiltonian. This allows one

to work in a smaller component space, by simply choosing the electronic quadrants (C_S and C_L) of the $(2N)^2$ Dirac eigenvector matrix (quadrants associated with positronic solutions are discarded). The X2C method can be made to neglect spin-orbit effects if the Pauli spin matrices are not applied to the momentum in Dyall's modified Hamiltonian,[21] in this work, only scalar relativistic effects will be considered. The X2C method is variational as it couples the variational 4-component Dirac Hamiltonian exactly; although this is only the case if 2-electron contributions are considered. In Chapter 3, the X2C correction is only applied to the core Hamiltonian and problems with variationality will be presented.

1.2 Configuration Interaction Methods

1.2.1 Natural Orbitals

Natural orbitals (NO)[22–24] were developed by Löwdin in 1956 specifically to solve the issues of interpretation and efficiency of MOs in configuration interaction. MO basis functions do not describe correlation optimally as they are constructed from a single Slater determinant. If one wants to study a system at a dissociated geometry or a transition metal (as is done in Chapter 3) NOs provide a better description than MOs. Natural orbitals are obtained by first constructing the 1-particle reduced density matrix (1-RDM)[25] from a correlated wavefunction

$$\gamma_{ij} = \langle \Psi | \hat{a}_i^\dagger \hat{a}_j | \Psi \rangle \tag{1.19}$$

Where $\hat{a}^\dagger$ is the creation operator, and $\hat{a}$ is the annihilation operator. The 1-RDM can be interpreted as representing the electron density in the MO basis. Diagonalization of the 1-RDM results in eigenpairs which correspond to the NOs. This new set of orbitals better describes electron correlation as a result of the wavefunction containing correlated terms.[26–28] This allows one to perform a cheaper configuration interaction calculation to obtain NOs, which will greatly improve the efficiency of a subsequent calculation. Multireference character can be determined, as the NO coefficients can be non-integer since they are not composed of a single determinant. If the NO occupation numbers are similar to orbital occupation numbers from HF, this suggests that a system is generally well described with a single configuration where non-integer occupation numbers indicate some degree of correlation.

1.2.2 Full Configuration Interaction

The concept of configuration interaction[29,30] follows from the variational principle; if more configurations are included, the total energy approaches the exact solution in a basis. If we desire the most accurate/quantitative description of a system, then all configurations should be incorporated into the wavefunction, which is known as full configuration interaction (FCI). If all possible configurations are considered, the wavefunction becomes

$$\Psi = c_0\psi_0 + \sum_{i,a} c_i^a \psi_i^a + \sum_{\substack{i<j \\ a<b}} c_{ij}^{ab} \psi_{ij}^{ab} + \cdots \tag{1.20}$$

On the right-hand side, the first term represents the reference wavefunction; this is just the ground state configuration in HF. The second term accounts for all possible single excitations, and the third term accounts for all possible double excitations. The problem with FCI is the scaling, where the number of configurations to include grows combinatorially with basis size and electron number

$$FCI_{configs} = \binom{N}{n_\alpha}\binom{N}{n_\beta} \tag{1.21}$$

This scaling makes the method intractable for everything besides small systems. A couple of the largest calculations that have been achieved are 26 electrons in 23 orbitals ($\sim 1.0 \times 10^{12}$ configurations) and 88 electrons in 100 2-spinor orbitals ($\sim 1.0 \times 10^{15}$ configurations) with intense computational effort.[31,32] Post-HF methods are typically trying to recover as much of this full Hilbert space to attain desired accuracy while keeping the method tractable.

1.2.3 Select Configuration Interaction

Select Configuration Interaction (SCI)[33–45] attempts to reduce the problem space of FCI. In the first step (variational step), SCI recovers correlation by selecting configurations from the full Hilbert space based upon "importance" and adding them to the wavefunction. It seems, and rightly so, that a search through the full Hilbert space would result in high computational costs; however, many of the excited configurations of interest are at relatively low excitation levels in the Hilbert space which reduces the scale of the search significantly in practice. The SCI step recovers most of the static correlation, while the remaining dynamic correlation is considered with perturbation theory (SCI+PT). With SCI+PT methods usually Epstein-Nesbet PT (EN-PT)[46] is employed due to the consideration it gives to the full Hamiltonian

$$E_{EN} = \sum_k \frac{(\sum_i H_{ki} c_i)^2}{E_{var} - H_{kk}} \tag{1.22}$$

Where E_{var} is the variational energy, k is the index over configurations external to the variational

space, I is the index over configurations contained in the variational wavefunction, and c_i are coefficients relating to the variational configurations.

Heat-Bath Configuration Interaction (HBCI)[42–45,47] is a specific SCI+PT method and is used throughout all the works contained here. The variational step of HBCI works by using an energy importance metric based on the connection of an existing variational element with one external to the space by

$$|H_{ki}c_i| > \varepsilon_{var} \tag{1.23}$$

ε_{var} is a user-defined variational threshold, singly and doubly excited configurations are generated from the existing variational space and compared to the variational threshold. Configurations which are above the threshold are added into the wavefunction, and those which are smaller than the threshold are discarded. The new wavefunction is then used as the existing variational space and the process continues iteratively. In our implementation, these iterations continue until the number of newly added configurations is less than 1% of the total variational space.

A modified version of EN-PT is then applied with another user-defined threshold ε_{PT}

$$\Delta E_{PT} \approx \sum_k \frac{\left(\sum_i^{(\varepsilon_{PT})} H_{ki}\, c_i\right)^2}{E_{var} - H_{kk}} \tag{1.24}$$

The user-defined threshold ε_{PT} should be set at least a couple orders of magnitude lower than ε_{var} to ensure the correction is in the perturbative regime (typically, 10^{-7} Ha or lower). The off-diagonal external configuration couplings and their associated diagonal external elements are used to provide a non-variational correction. In PT the corrections are known to reduce the energy below the exact solution.[48]

1.3 Density Functional Theory

1.3.1 Kohn-Sham Formalism

Wavefunction theory utilizes the wavefunction to obtain observable information, but the wavefunction is also directly related to the density. Based on the Hohenberg-Kohn theorem (and more general formulations) it can be proven that the wavefunction maps to a unique density, and vice versa.[49,50] This allows one to instead use the density to solve for observable information; the Kohn-Sham (KS)[51] formalism exists to this end.

$$\left[-\frac{\nabla^2}{2} + v_{KS}(r)\right]\varphi_i = \varepsilon_i \varphi_i \tag{1.25}$$

The terms in the bracket are kinetic and potential energy, ε are the KS eigenvalues, and φ are KS orbitals. The KS potential energy v_{KS} can be expanded in terms of component potentials

$$v_{KS}(r) = v_{ext}(r) + v_H(r) + v_{xc}(r) \tag{1.26}$$

v_{ext} is the external potential, v_H is the Hartree potential, and v_{xc} is the exchange-correlation (XC) potential. The operators in this equation are set up such that the particles in the system are treated as non-interacting (one-body terms) and these quantities can be calculated exactly, aside from v_{xc}, which contains quantum interactions. The external potential arises from interactions between the electrons and nuclei and the Hartree potential encodes the classical coulomb interactions. The Hartree term is considered non-interacting because the interactions are 1-body in a mean field, while the external potential is non-interacting due to the BO approximation (nuclei are treated as fixed point charges). The exact form that v_{xc} takes is unknown; this is the term that functionals seek to approximate. Hypothetically, if one knew the v_{xc} exactly, then exact solutions would result from the KS equations, making it desirable to understand what form v_{xc} takes.[52–57]

1.3.2 Inverse Density Functional Theory

Inverse density functional theory (invDFT) aims to recover the XC potential provided a density, which is different from DFT, where the XC potential is given (approximated), and one finds the optimal density (KS orbitals).[58] An early implementation of invDFT was developed using work from van Leeuwen and Baerends,[59–61] where the KS equations are used to form an orbital averaging expression which is solved incrementally until the KS orbitals produce a density which matches the reference density to some threshold. This procedure approximates the potential from a known density, meaning it is not exact. Other procedures, such as the optimized effective potential (OEP),[62–67] have been shown to be ill-posed[68] (does not have a unique solution that depends continuously on input parameters) in finite basis sets producing non-unique XC potentials. To this end, the Kanungo-Zimmerman-Gavini[69] procedure was developed, which solves a constrained optimization problem in a complete basis producing an exact potential. Even with KZG, it is still desirable to obtain XC potentials from finite basis sets, as they are widely used in electronic structure theory.

The Ryabinkin-Kohut-Staroverov (RKS)[70] method aims to produce accurate XC potentials in finite basis sets, specifically a Gaussian basis. This method works by directly taking the wavefunction from a correlated method, constructing the 1- and 2-RDM, and iteratively solving for the KS orbitals. Further contributions by Tribedi et al.,[71] which expand upon this work, modify

the procedure to accommodate a Slater basis set. Another method developed by Rask et al.[72] facilitates the determination of KS orbitals which, as will be seen in section 1.3.3, can be used as a reference in invDFT methods. KS orbitals are obtained by minimizing the difference in the densities while also balancing the minimization of the kinetic energy. The space of invDFT has seen much growth in recent years, enabling further probes into the role of exchange and correlation in progressively more complex systems, as illustrated in Chapter 4.

1.3.3 Orbital-Averaging Inversion

The following procedure is the inverse DFT engine, which will be used in Chapter 4, adapted from Khanna et al.[1] and the energy balance from RKS.[70] It works by using the 1- and 2-RDM from a highly correlated wavefunction calculation, such as HBCI. This density is then used to optimize the KS density through the minimization equation formulated by Rask et al.[72]

$$\Phi_{KS} = arg\ min\left(\int |\rho_{WF}(r) - \rho_{KS}(r)|^n dr + \lambda\langle\Phi_{KS}|\hat{T}|\Phi_{KS}\rangle\right) \tag{1.27}$$

Where n controls the optimization surface, $\hat{T}$ is the KS kinetic energy, and λ is a parameter which is chosen to balance the minimization of the density difference and KS kinetic energy[73]. This minimization works without using the KS equations directly and instead optimizes the KS orbitals via orbital rotation, maintaining orthogonality of the guess. Equation 1.27 does not solve for KS eigenvalues, but they are a necessary parameter to specify for use in the energy balance expression.

To solve for the eigenvalues, we project the KS equation for an occupied orbital onto a virtual orbital and substitute the OA expression.[59–61]

$$\int \varphi_a^*(r)\left[-\frac{1}{2}\nabla^2 + \frac{\sum_{j=1}^{N} n_j\left(\varepsilon_j|\varphi_j(r)|^2 + \frac{1}{2}\varphi_j^*(r)\nabla^2\varphi_j(r)\right)}{\rho(r)}\right]\varphi_i(r)dr = \varepsilon_i\delta_{ai} = 0 \tag{1.28}$$

Where δ is the Dirac delta function, and i and a are indices over occupied and virtual orbitals, respectively. Since occupied and virtual orbitals are in different sets, the Dirac delta evaluates to 0, and we can construct a linear system of equations to solve for the eigenvalues.

$$E = (B^T B)^{-1} B^T R \tag{1.29}$$

Where B is a matrix of elements obtained from equation 1.28, E are the eigenvalues, and R is the residual. The residual is minimized by least squares from equation 1.29.

It is well known that to get the $-\frac{1}{r}$ decay of v_{xc}, the HOMO energy and the negative ionization potential (IP) energy must be equivalent.[74–76] This is enforced through the analog of equation 1.28 by taking the inner product of the KS equation for the HOMO orbital, in this case, the Dirac delta is 1, and one can set $\varepsilon_{HOMO} = -IP$. After obtaining the eigenvalues, one can directly solve for v_{xc} by using the energy balance equation[70]

$$v_{xc}(r) = v_{KS}^{WF}(r) + \bar{\varepsilon}^{KS}(r) - \bar{\varepsilon}^{WF}(r) + \frac{\tau^{WF}(r)}{\rho^{WF}(r)} - \frac{\tau^{KS}(r)}{\rho^{KS}(r)} \tag{1.30}$$

Where $\bar{\varepsilon}$ is the average local orbital energy, and $\frac{\tau}{\rho}$ is the kinetic energy density. Since the orbital averaging expression is divided by density, v_{xc} can become numerically unstable when the density becomes small. As a result of the WF and KS densities being fit, both XC potentials should have the same decay, thus we can enforce the equality of $v_{xc} = v_{xc}^{Slater}$ below a certain density threshold.[71] This procedure results in XC potentials in a Slater basis which match very nicely with exact XC potentials. This decay equivalence is not enforced in the procedure discussed in Chapter 4.

1.4 Conclusion

The remaining chapters in this work explore developing new methodology using some of these concepts (Chapter 2) and tweaking existing methodology to get quantitative information for interesting/difficult chemical systems (Chapters 3 and 4). The methods/concepts described in section 1.1.2, such as Slater basis sets and integral quantities, will be analyzed on a prolate spheroidal grid in Chapter 2. Chapter 3 will rely heavily on configuration interaction methods to obtain greater quantitative accuracy for TM systems than existing methods, requiring background from sections 1.2 and 1.1.6. Finally, Chapter 4 will expand upon concepts and methodology from section 1.3, where the near-exact KS potential at a conical intersection will be obtained and analyzed for the first time.

Chapter 2

Numerical Integration of Slater Basis Functions Over Prolate Spheroidal Grids

This chapter is adapted from previously published work.[77] In this chapter, a new method of obtaining accurate integral quantities related to the Hamiltonian via numerical integration over a prolate spheroidal (PS) grid is presented. This work builds upon SlaterGPU and uses the features for fast and efficient grid evaluation. Analysis of the accuracy of the new grid is conducted in relation to the Becke partitioning, which was used in the initial implementation of SlaterGPU.

2.1 Introduction

Electronic structure theory can provide insight into a countless number of chemical systems. Practical methods for molecules most often rely on wavefunctions built upon atom-centered, single-electron basis functions. Certain asymptotic properties of exact wavefunctions can be captured in the single-particle basis set,[78] such as cusps at the nuclei that are consistent with the Kato conditions.[79,80] At long distances, wavefunctions decay as simple exponentials. These two ideas lead naturally to Slater type orbitals (STOs),[78] which have the form

$$\chi_{nlm}(r,\theta,\phi) = Nr^{n-1}e^{-\xi r}Y^{lm}(\theta,\phi) \tag{2.1}$$

N is a normalization factor, ξ is the exponent defining each basis function, n, l, m are the principal quantum numbers, and Y^{lm} are spherical harmonics.[79,81] STOs are known to provide accurate descriptions of polarizability, intermolecular interactions, and nuclear shielding, as these properties are sensitive to cusp or decay of the wavefunction.[82–84] The widespread use of Slater functions as electronic structure basis sets, however, has been significantly hindered due to the requirement for numerical integration.

While STOs correctly describe physical properties, their features—such as steepness near the nucleus and long tails—make them difficult to numerically integrate. While some Slater

[77] Stark, A. et al. Numerical Integration of Slater Basis Functions Over Prolate Spheroidal Grids. *Journal of Computational Chemistry* **2026**. https://doi.org/10.1002/jcc.70291

integrals are available analytically,[85–87] the electronic Hamiltonian for polyatomics requires Slater integrals which have no known analytical form. Gaussian Type Orbitals (GTOs), in contrast, are generally analytically integrable[8,88–91] but cannot precisely capture nuclear cusps or long-range decays. Improved integration protocols could start to bridge the practicality gap between STOs and GTOs, making STOs more readily usable in a wide range of electronic structure theories. This work therefore builds upon our recent efforts[92] to provide highly accurate Slater integrals, especially for their use in wavefunction simulations.

Integration of Slater functions has often been performed using atom-centered integration grids, for instance as done in the Amsterdam density functional (ADF) program,[1,93–96] and more recently through the SlaterGPU library.[92] These integrals use products of radial and angular grids on each atom, where the grid weights are adjusted to avoid overcounting in regions where the grids are overlapping. While various partitioning methods are possible,[97] Becke's method of fuzzy Voronoi cells[98] is probably the most well-known, due to its widespread use in the integration of quantities related to density functional theory (DFT).[99,100] Becke partitioning (BP) in ADF has produced integrals required for the GW approximation.[101–105] In SlaterGPU, BP has been used in RKS calculations to produce Kohn–Sham potentials.[71]

Two of the authors recently introduced SlaterGPU,[92] an algorithm for accelerating STO integrations on graphics processing units (GPUs). This GPU library uses parallel numerical integration with efficient vector operators based on mixed-precision arithmetic to keep execution costs low. Equally important to the parallelized code was the use of the resolution-of-the-identity (RI)[106–108] approximation to reduce the complexity of Coulomb integrals. Coulomb integration with RI can be performed in three dimensions in an STO basis, saving a great amount of computational time compared to six-dimensional integration. Altogether, the original SlaterGPU implementation provided a practical means to perform electronic structure computations at the Hartree–Fock (HF), Complete Active Space Self-Consistent Field (CASSCF), and full configuration interaction (FCI) levels for double- and triple-zeta STO basis sets. The atomic Becke/Voronoi grids of SlaterGPU, however, are insufficiently precise to treat larger basis sets (e.g., for pentuple-zeta, polarized basis sets).

The quality of numerical integration scheme is tied closely to the coordinate system and quadrature that together form the integration grid.[98] Becke showed that an orthogonal curvilinear coordinate system known as prolate spheroidal (PS) coordinates can be effective for integrals

involving two centers.[109] PS coordinates have an origin between two foci and are composed of a radial part μ and two angular parts ν and ϕ, where μ is composed of spheroids that encompass these foci, ν is composed of hyperboloids, and ϕ is a plane on the focal axis. An interesting property of PS coordinates is that the μ, ν degrees of freedom are closely related to r_1, r_2, the distances to the two nuclei that define the coordinate system. Close to the nucleus, $r_1$and r_2 are quadratic in μ, ν, meaning that Slater functions become Gaussians ($exp[-\xi r] \longrightarrow exp[-\xi a(\mu^2 + \nu^2)]$). This coordinate transformation reduces the steepness of the STOs near the nuclei in the PS coordinate space, without compromising the Slater shape expected by the Hamiltonian.

While PS coordinates are a natural generalization of spherical coordinates from atoms to diatomics, there is no general procedure to handle cases with more than two atoms within this coordinate system. Fortunately, under the RI approximation, only 3-center integrals are required, so a complete generalization to many-center integration is not required. A path forward to use PS coordinates in practical STO integrations for molecules is therefore conceivable, as long as a careful choice of grid discretization around the third center is made.

The SlaterGPU library and its extension to PS coordinates are designed to generate all of the terms necessary for a nonrelativistic electronic Hamiltonian expressed in atom-centered Slater orbitals, for example, for HF, DFT, and post-self-consistent-field (SCF) methods. The goal of this work is to show that polyatomic systems can be handled within the PS coordinate system, with sufficient accuracy and efficiency to allow for the evaluation of larger basis sets. Not only will this allow increased accuracy in post-SCF correlated methods, it also will be useful in deriving Kohn–Sham orbitals and exchange-correlation potentials to high accuracy.[71,72]

2.2 Theory

2.2.1 PS Coordinates

PS coordinates are an orthogonal curvilinear coordinate system in three dimensions (μ, ν, ϕ). The coordinates are defined with respect to two foci, which in this case will be positions of two basis functions. If the two foci are defined in Cartesian coordinates at the points $(0,0,a)$ and $(0,0,-a)$ then the relation between Cartesian and PS coordinates is defined by

$$x = a \sinh\mu \sin\nu \cos\phi \tag{2.2}$$

$$y = a \sinh\mu \sin\nu \sin\phi \tag{2.3}$$

$$z = a \cosh\mu \cos\nu \tag{2.4}$$

Any two-center integral can be performed after rotation and translation of this grid, assuming distance $2a$ between the centers (integration with more than two atoms is discussed later on). Radial distances from the foci are

$$r_1 = a(\cosh\mu + \cos\nu) \tag{2.5}$$

$$r_2 = a(\cosh\mu - \cos\nu) \tag{2.6}$$

As pointed out by Becke[109] for small r_1 or r , a Taylor expansion shows that each of these distances is quadratic in μ, ν. Slater functions therefore can be efficiently integrated due to the avoidance of the cusp near the nucleus, while maintaining the correct physical cusp shape.

The ν and ϕ coordinates span $0 \leq \nu \leq \pi$ and $0 \leq \phi \leq 2\pi$. The ν coordinate moves between the two foci, and the ϕ coordinate rotates around the central axis with cylindrical symmetry. The μ coordinate spans $0 \leq \mu \leq \infty$, and therefore is mapped onto a finite range in practice (Figure 2.1).

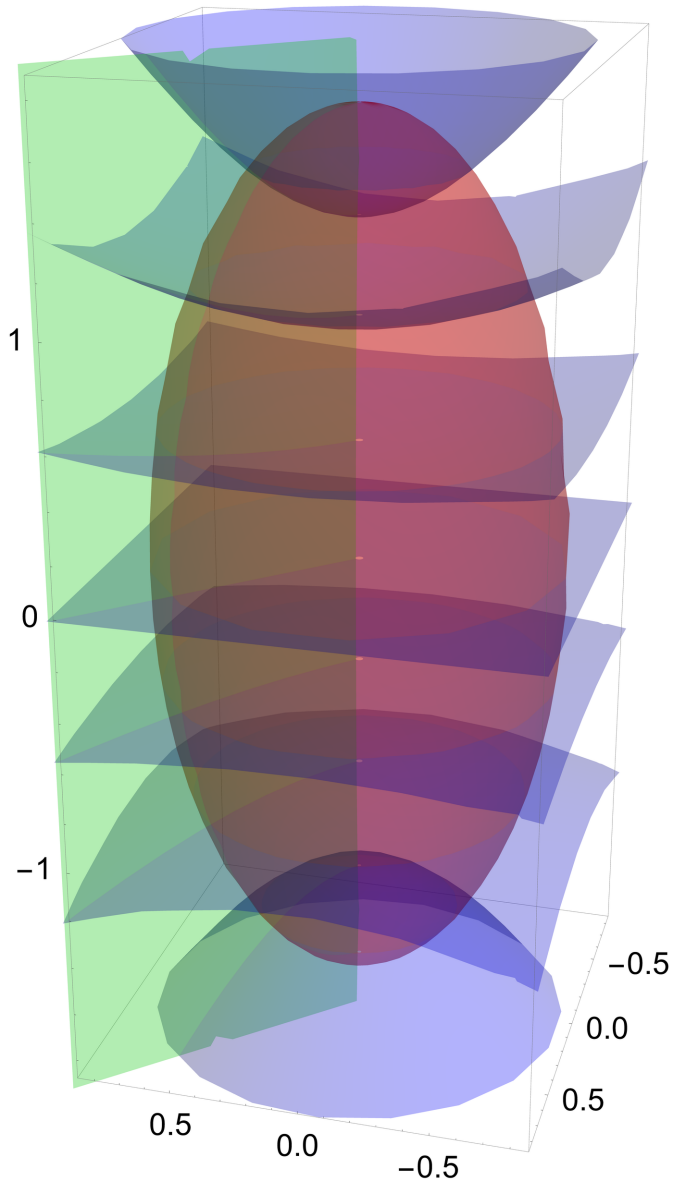

Figure 2.1: The Prolate Spheroidal grid on a cartesian grid with spheroids at constant μ (red), hyperboloids at constant ν (blue), and planes at constant ϕ (green).

The PS grid must be discretized to perform numerical integration, as Slater functions will be evaluated at discrete points. Uniform grids in the ν and ϕ coordinates are plausible, though the μ coordinate deserves more consideration. For example, the μ grid points should be more concentrated near the nuclei, where the most rapid changes in basis functions occur. Therefore for $0 < t_1 < 1$ we have

$$\mu = C_1 \tanh^{-1}(t_1) \tag{2.7}$$

where C_1 and the maximum value of t_1 together fix the maximum value of μ. The t_1 coordinates, when uniformly divided, lead to more μ points near the nuclei. Here, the ν and ϕ grid points are

also spaced evenly. Related discretization methods for other coordinate systems can be found in refs. 92,109–111.

Having introduced a method to divide PS coordinate space into discrete volume elements, quadrature within each volume element completes the integration scheme. Due to the way the grid is constructed—where grid discretization places nuclei only at the edges of each volume element—quadrature points will never be evaluated at a nucleus. This can be done using Gauss-Legendre quadrature for all dimensions, which approximates an integral over a volume element without placing points on boundaries.[112] Gauss–Legendre quadrature is exact for polynomials of $2n-1$ order, allowing rapid convergence with size of quadrature grid.

A generic integral involving a pair of Slater functions has the form

$$\int_0^{2\pi}\int_0^{\pi}\int_0^{\infty}\chi_a(\mu,\nu,\phi)\hat{O}(\mu,\nu,\phi)\chi_b(\mu,\nu,\phi)d\mu d\nu d\phi \tag{2.8}$$

Applying discretization and quadrature to this generic integral yields

$$\sum_{i=1}^{M}\sum_{i=j}^{Q}\chi_a(x_{ij})\hat{O}(x_{ij})\chi_b(x_{ij})w(x_{ij}) \tag{2.9}$$

where functions will be evaluated at points x_{ij}, $\hat{O}$ is the operator of interest, $w(x_{ij})$ is the weight function associated with the quadrature, Q is the number of quadrature points within a volume element, and M is the number of volume elements. The weights are

$$w(x_{ij}) = G(\mu_{ij})G(\nu_{ij})G(\phi_{ij})\Delta V \tag{2.10}$$

where $G(\mu_{ij}), G(\nu_{ij}), G(\phi_{ij})$ are the weights from the Gaussian quadrature. The volume element is determined by the spatial extent of the discretized cells.

$$\Delta V = a^3 \sinh\mu_{ij} \sin\nu_{ij} \left(\sinh^2\mu_{ij} + \sin^2\nu_{ij}\right)\Delta\mu_{ij}\Delta\nu_{ij}\Delta\phi_{ij} \tag{2.11}$$

This two-center integration scheme will be shown below to be highly effective.

2.2.2 Treatment of a Third Center

Two-center integration using PS coordinates is efficient since volume elements can be naturally distributed based on the positions of the two centers. Quadrature is also facilitated around these centers due to the grid lines at $\mu = 0$ and $\nu = 0$ or π. The third center, however, will sit somewhere in an arbitrarily sized volume element, with no particular location relative to the PS grid lines (Figure 2.2A). To achieve accurate quadrature, the grid lines should be placed to intersect the third nucleus, and the volume elements subdivided. Our grid lines are therefore shifted to

accommodate the third center, specifically by moving the nearest volume element borders in μ and ν (the position of ϕ is trivial, as the three centers will be placed within the same plane before generating the grid). After the grid lines are moved, the 8 volume elements surrounding the third center are then further divided (Figure 2.2$B \rightarrow C$). Figure 2.2 shows a single division surrounding the third center, where 4 cells are divided in half along μ and ν. Including the ϕ degree of freedom, the 8 neighboring cells become 64 cells. This division can be increased to create more cells as necessary to achieve higher precision. The parameter N_{SP} defines how many cells are used to discretize around the third center.

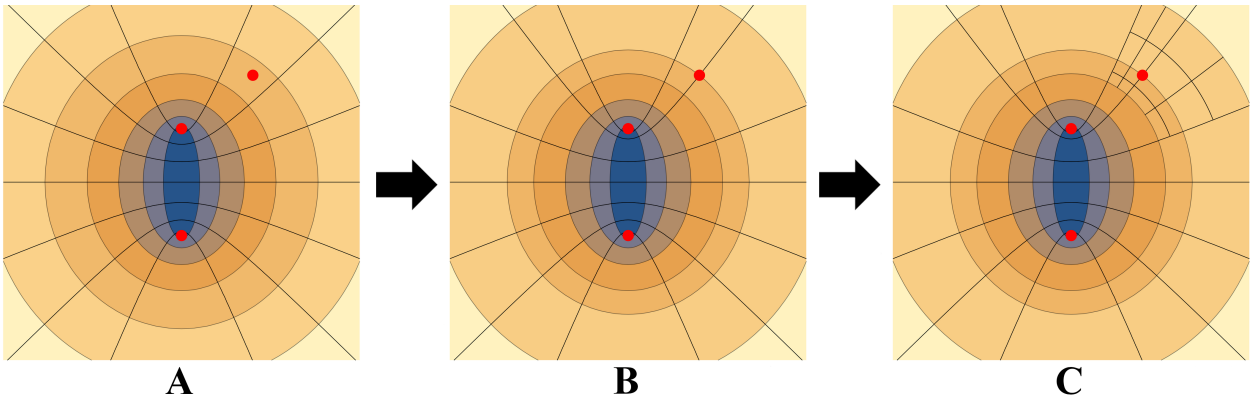

Figure 2.2: The process of reorienting the grid around the third center, (A) is the initial spacing of the grid with the third center being located at one of the volume elements, (B) moves the μ and ν grid lines closest to the third center so that the third center coordinates align with the grid lines, and (C) splits the grid further around the third center for greater accuracy.

2.2.3 Implementation

The integration grid is set up by enumerating over the discrete volume elements and their weights. First, the angular grid lines are defined for ν and ϕ by dividing π and 2π by N_ν and N_ϕ, respectively. The radial component that determines μ (cf. Equation 2.12) is divided in the t_1 transform uniformly through

$$\Delta t_1 = \frac{1}{N_\mu + 1} \tag{2.12}$$

where N is the number of μ grid separations. Once the initial 2-center grid is constructed, the third center is considered in the grid. The third center is placed at $\phi = 0$ for alignment within the ϕ grid line. Next, the μ and ν grid lines closest to the third center are moved to intersect the third center, as shown in Figure 2.2. Finally, each volume element defined by the above grid lines is divided up via three-dimensional quadrature to give the full integration grid (Algorithms 2.1 and 2.2).

Algorithm 2.1: Coordinate grid discretization: N , N , and N_ϕ, are the number of divisions over a coordinate. μ, ν, and ϕ represent a point in the center of a volume element and $d\mu$, $d\nu$, and $d\phi$ are the distance from one edge of the volume element to the other edge of the volume element.

```
dx, dν, dϕ calculated based on user input
for i in N_μ do
    t_i, t_{i−1} ← dt, i
    μ_i, μ_{i−1} ← t_i, t_{i−1}
    μ, dμ ← μ_i, μ_{i−1}
    for j in N_ν do
        ν ← dν, j
        for k in N_ϕ do
            ϕ ← dϕ, k
            Save to Grid[μ, ν, ϕ, dμ, dν, dϕ]
```

Algorithm 2.2: Quadrature grid initialization: Q_μ, Q_ν, and Q_ϕ are the quadrature points of a respective coordinate and w_μ, w_ν, and w_ϕ are the associated weights.

```
for n in volume elements do
    Read in volume element μ_n, ν_n, ϕ_n, dμ_n, dν_n, dϕ_n
    for i in Q_μ points do
        μ_ni ← Q_iμ, μ_n, dμ_n
        Read in w_iμ
        for j in Q_ν points do
            ν_nj ← Q_jμ, μ_n, dμ_n
            Read in w_jν
            for k in Q_ϕ points do
                ϕ_nk ← Q_kμ, μ_n, dμ_n
                Read in w_kϕ
                Qpoints[x, y, z] ← μ_ni, ν_nj, ϕ_nk
                weight[w] ← w_iμ, w_jν, w_kϕ
```

2.3 Computational Details

Most results in this work utilize an all-electron triple-zeta basis set with polarization functions (denoted TZ), while others utilize quadruple- and pentuple-zeta basis sets (denoted QZ and 5Z, respectively). Basis sets were constructed to be even tempered (with exponents $\zeta = \alpha\beta^n$, $n = 0, -1, \cdots, -N$) where N depends on the angular momentum and row on the periodic table. Auxiliary functions were generated in a combinatorial fashion from the original basis by adding

together the angular momentum ℓ as well as the exponents of all pairs of functions on each atom. For each channel ℓ, the minimum and maximum summed exponents (ζ_{max} and ζ_{min}) were selected to define the range for the auxiliary basis. The auxiliary basis is then generated through an even-tempered procedure with ζ_{max} and ζ_{min} as its limits.[113–116] Finally, all m degrees of freedom for each ℓ were enumerated. The basis sets are provided in Table A.1.

Figures 2.3-2.6 and Table 2.1 all analyze integral matrices directly. Figures 2.3-2.5 and Table 2.1 do so through analysis of the root mean square error (RMSE) which is defined by

$$RMSE = \sqrt{\frac{\sum_{i=1}^{n}\left(g_i^{ref} - g_i\right)^2}{n}} \tag{2.13}$$

g_i are matrix elements in the integral matrices, g^{ref} is a matrix produced from an accurate calculation with a large grid, and g is a matrix produced from some less accurate calculation.

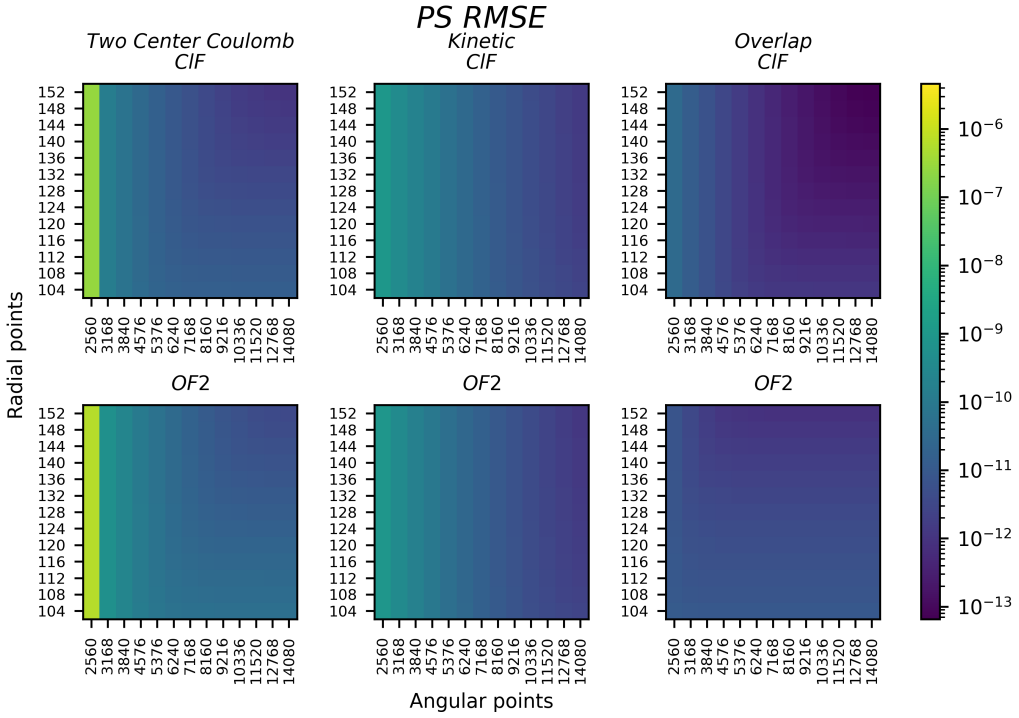

Figure 2.3: Overlap, kinetic energy, and 2-center Coulomb repulsion RMSE (Ha) analyzed for ClF and OF_2 using the PS method in a TZ basis.

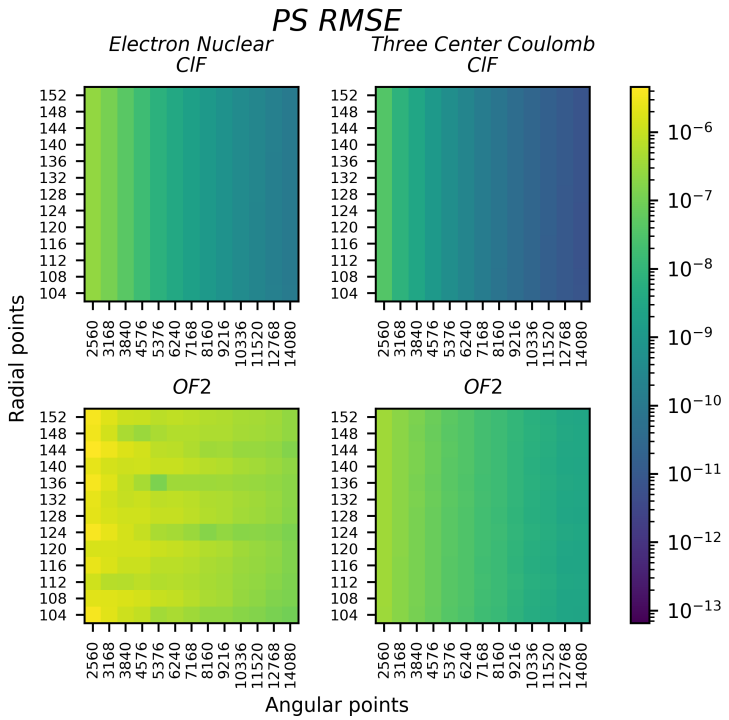

Figure 2.4: Electron-nuclear attraction and 3-center Coulomb repulsion RMSE (Ha) analyzed for ClF and OF_2 using the PS method in a TZ basis. The grid selection and legend are the same as in Figure 2.3.

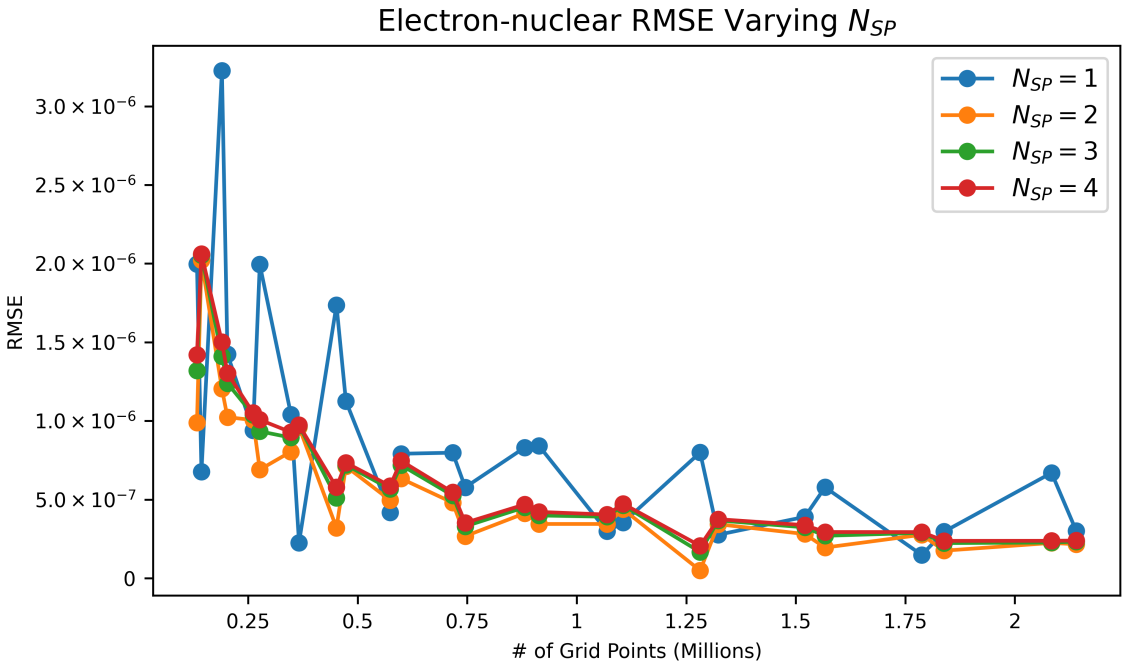

Figure 2.5: Comparison of the RMSE (Ha) of the electron-nuclear attraction elements for different divisions of the third center within the PS integration grid. A single split ($N_{SP} = 2$) gives significant advantages over no splitting, and $N_{SP} > 2$ gives marginal improvements.

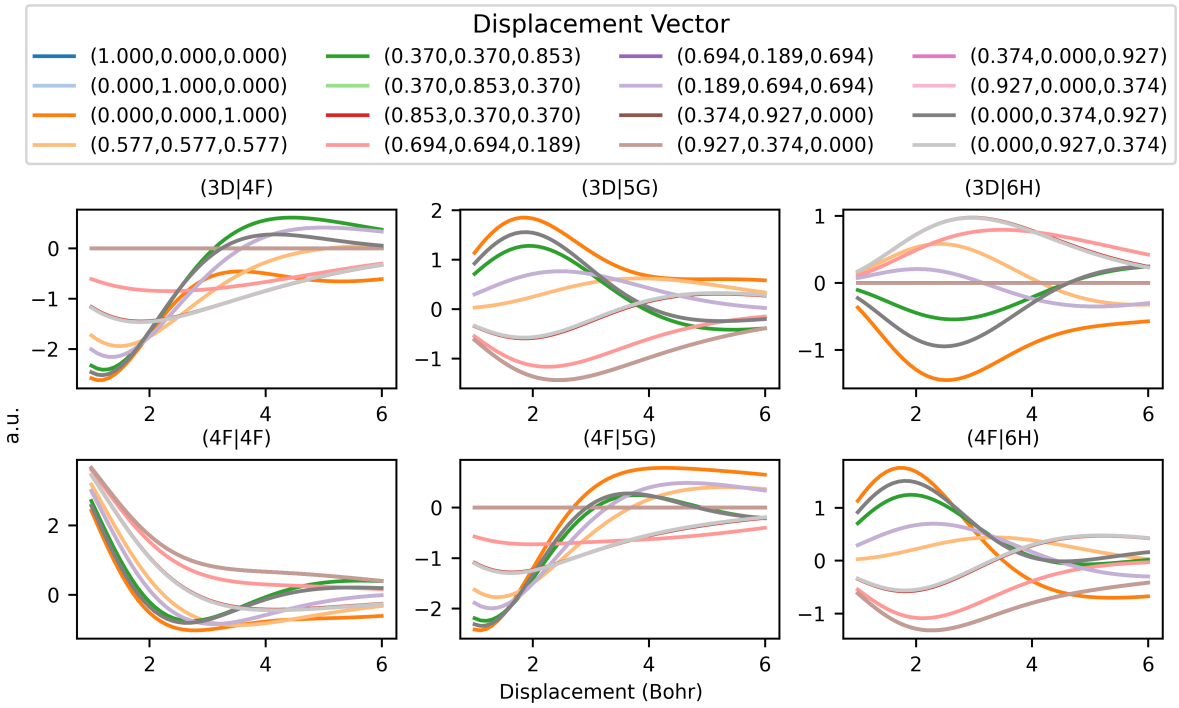

Figure 2.6: Six 2-center Coulomb integrals plotted along 16 vector directions[92] as the two centers are separated. The legend indicates unit vectors for all 16 directions tested, all basis functions used have the exponent $\zeta = 1$, and all basis functions were chosen to have $m = 0$.

Table 2.1: RMSE (Ha) of integrals for SO_2 using BP and PS integration with TZ, QZ, and 5Z basis sets. Basis sets TZ, QZ, 5Z are described in the computational details.

RMSE of integrals on SO_2						
	TZ		QZ		5Z	
	BP	PS	BP	PS	BP	PS
Overlap	1.3×10^{-08}	8.0×10^{-12}	7.6×10^{-09}	5.4×10^{-12}	1.3×10^{-08}	8.9×10^{-12}
Kinetic	4.6×10^{-07}	9.6×10^{-11}	3.1×10^{-07}	3.0×10^{-10}	3.0×10^{-07}	2.8×10^{-10}
Electron Nuclear	7.7×10^{-07}	3.0×10^{-07}	5.8×10^{-07}	3.1×10^{-07}	6.0×10^{-07}	3.2×10^{-07}
2-Center Coulomb	3.2×10^{-08}	4.9×10^{-11}	2.0×10^{-08}	6.8×10^{-11}	3.1×10^{-08}	8.1×10^{-11}
3-Center Coulomb	8.7×10^{-09}	6.6×10^{-09}	5.6×10^{-09}	1.3×10^{-08}	7.3×10^{-09}	1.6×10^{-08}

Coulomb integrals take the form

$$(ab|cd) = \iint \chi_a(\vec{r}_1)\chi_b(\vec{r}_1)\frac{1}{r_{12}}\chi_c(\vec{r}_2)\chi_d(\vec{r}_2)d\vec{r}_1 d\vec{r}_2 \tag{2.14}$$

Classical and nonclassical (exchange) Coulomb integrals are computed under the RI approximation, where 4-index integrals are determined as follows

$$(ab|cd) \approx \sum_{PQ}(ab|P)(PQ)^{-1}(Q|cd) \tag{2.15}$$

These two 3-index terms can be expressed as

$$(P|ab) = \iint \chi_P(r_1)\frac{1}{r_{12}}\chi_a(r_2)\chi_b(r_2)\,dr_1 dr_2 \tag{2.16}$$

and simplified to

$$(P|ab) = \int V_C^P(r)\chi_a(r)\chi_b(r)dr \tag{2.17}$$

More information on the form of this potential is discussed in the original SlaterGPU paper,[92] while alternatives for Coulomb resolution are in principle also possible.[117,118] The analytical 1-center Slater potential has been derived in a previous work,[119] this allows for direct use of the expression V_C^P without fitting the density to the Coulomb operator.

All CI computations in Table 2.3 were run in a neutral state (singlet spin for all, except doublet spin for NO, N_3, and NO_2). The geometries for the diatomic systems in the table were obtained from the Computational Chemistry Comparison and Benchmark DataBase (https://cccbdb.nist.gov/). Triatomic geometries were optimized using Q-Chem version 5.2,[120] geometries for specific species and information about methods used to obtain these geometries can be found in Table A.2.

Heat-bath configuration interaction (HBCI), used in Tables 2.3 and 2.4, is a select-CI approach that returns a close approximation to the full CI limit.[42–45] The energy thresholds ε_{var} and ε_{PT} control the extent of recovery of correlation through variational (ε_{var}) and perturbative (ε_{PT}) steps. These thresholds control convergence by screening electronic configurations based on estimating how much an external configuration may contribute to the total energy and adding in components with the highest importance. In Table 2.3 HBCI was performed using $\varepsilon_{var} = 1 \times 10^{-4}$ Ha and $\varepsilon_{PT} = 1 \times 10^{-7}$ Ha except in cases which possess greater than 15 valence electrons (N_2O, NO_2, OF_2, SO_2, CS_2), which used $\varepsilon_{var} = 5 \times 10^{-4}$ Ha and $\varepsilon_{PT} = 5 \times 10^{-7}$ Ha. The incremental full CI (iFCI) method, used in Figure 2.7, truncates the search for configurations in the Hilbert space further by defining localized molecular orbitals as base units for correlation. A many-body expansion combines these units to systematically recover correlation from a reference state (a valence bond, perfect-pairing wave function), ensuring convergence to full CI as the expansion level, n, is increased.[121–123] This allows for polynomial scaling of the iFCI method while maintaining a similar accuracy to HBCI. Here, $n = 3$ recovers the majority of the correlation energy and simplifies the computation of the 24-electron in 225 orbital all electron (core + valence) space. See refs. 121,124,125 for further details of this approach. The HBCI solver in the iFCI calculation uses energy thresholds of $\varepsilon_{var,doubles} = 5 \times 10^{-4}$ Ha, $\varepsilon_{var,singles} = 2.5 \times 10^{-4}$, and

$\varepsilon_{PT} = 1 \times 10^{-7}$ Ha. The frozen core approximation has been used in all calculations, besides in Table 2.4 and Figure 2.7, where all electrons were correlated. The CCSD(T) method[126,127] was also performed in Figure 2.7, applied to the same 1,3-propanediyl system, core correlation was included and a UHF reference was utilized.

LUNO

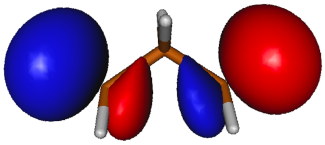

HONO

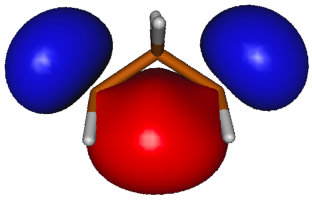

	iFCI ($n = 3$)	CCSD(T)
$LUNO\ n_{occ}\ S_0$	0.394	-
$HONO\ n_{occ}\ S_0$	1.59	-
$LUNO\ n_{occ}\ T_1$	0.993	-
$HONO\ n_{occ}\ T_1$	0.995	-
Singlet-Triplet Gap (kcal/mol)	13.4	11.8

Figure 2.7: HONO and LUNO orbitals and occupation numbers for the singlet and triplet states of 1,3-propanediyl as well as the singlet-triplet gap for the vertical excitation. iFCI uses the STO QZ basis while CCSD(T) uses a GTO basis, cc-pVQZ.

For comparisons to GTOs for the methylene and 1,3-propanediyl systems, the cc-pVXZ family was used, the cc-pVXZ-RIFIT auxiliary basis was utilized in calculations on methylene, no auxiliary basis was used for 1,3-propanediyl. Here X is T, Q, and 5 for polarized triple-, quadruple-, and pentuple-zeta basis sets, respectively. HBCI[45] was used as a representative electronic structure method, which closely approximates the full CI energy. The Nvidia HPC SDK 25.5 compiler suite with OpenACC was used to compile SlaterGPU and HBCI. The calculations using GTOs on the CH_2 system in Table 2.4 were run using Q-Chem version 5.2.[120] The CCSD(T) calculations used in Figure 2.7 were run using ORCA 6.0.1.[128–131]

When discretizing the initial PS grid, the scalar C_1 transforms the overall grid size, depending on the spacing between the nuclei. This is set to

$$C_1 = 2.3a^{1/4} \tag{2.18}$$

The angular components are left untransformed.

There are five variables (N_μ, N_ν, N_ϕ, quadrature points (Q), and third-center split (N_{SP})) which need to be chosen to specify the grid for PS integration. To demonstrate convergence with respect to grid size, we vary the radial grid size as well as the angular grid size but fix $Q = 4$ and

$N_{SP} = 3$ unless otherwise mentioned. Table A.3 shows the choice of grid sizes for the radial and angular grids used in Figures 2.3-2.5. For comparisons in Table 2.1 between the BP integration (with a grid composed of 5810 angular points and 120 radial points per atom) and the similarly sized PS grid (N_μ: 26 N_ν: 32 N_ϕ: 14 Q: 4 N_{SP}: 3), these results are compared to a large PS grid (N_μ: 80 N_ν: 70 N_ϕ: 50 Q: 4 N_{SP}: 3). Table 2.2 uses the same BP grid as Table 2.1. Figure 2.6 as well as Tables 2.2-2.4 use the same large PS grid as Table 2.1. The iFCI calculations on the 1,3-propanediyl system in Figure 2.7 use a PS grid with the following parameters N_μ: 80 N_ν: 60 N_ϕ: 40 Q: 4 N_{SP}: 4.

Table 2.2: Convergence of Hartree-Fock SCF runs with BP integration. Each number indicates the eigenvalue threshold needed to control numerical stability of the overlap matrix inversion. If the value is 0 (green) all threshold values tested allow for SCF convergence. Higher values indicate instability at this step, due to lower accuracy of the overlap matrix elements. Oscillatory cases (orange) oscillated around the energy obtained through the PS method with a difference less than 0.1 Ha but did not converge. Energies which varied by more than 0.1 Ha are marked in red. In comparison, PS integration converged for all cases with the smallest eigenvalue threshold.

Eigenvalue Cutoff for SCF Convergence (BP Integration)											
Mol	TZ	QZ	5Z	Mol	TZ	QZ	5Z	Mol	TZ	QZ	5Z
HF				CS				N_3			
C_2				SiO				N_2O			
N_2				ClF				NO_2			
CO				Cl_2				SFH			
NO				H_2O				OF_2			
O_2				HCN				SO_2			
HCl				OFH				CS_2			

Success | Oscillatory | Far from Convergent

2.4 Results and Discussion

As a starting point, two molecules were selected to demonstrate and benchmark the new PS integration method: ClF and OF_2. The 2- and 3-center integrals needed for the electronic Hamiltonian under the RI approximation were computed using a range of grid sizes. By varying the number of radial and angular discretization points, the convergence and numerical accuracy of PS integration will be discussed and then compared to integrals from the original SlaterGPU method.[92] The Slater basis for the initial tests is of triple-ζ quality, including s, p, and d angular

momentum functions and exponents ranging from 0.75 to 22.0. The auxiliary basis contains up to g functions.

Figures 2.3 and 2.4 show that the PS integration technique produces low errors and smooth convergence with respect to radial and angular discretization for all Hamiltonian elements for ClF. The most challenging cases are the electron-nuclear attraction integrals, due to the singularity at each nucleus. Regardless, the smallest integration grid for 2-center Coulomb (Figure 2.3) reaches an RMSE of order 10^{-7}, and increased grid discretization lowers errors to order 10^{-12} RMSE. These errors are lower than those of the original SlaterGPU method (a detailed comparison is given later on). The remaining integrals—the overlap, kinetic, electron nuclear and 3-center Coulomb integrals—all show excellent convergence. Obtaining RMSE below 10^{-10} does not require especially large grids. The largest grids investigated here show RMSEs around $10^{-13} - 10^{-14}$, which is close to what is possible with double precision arithmetic. These results confirm two-center integrals are well matched to numerical PS integration.[132,133]

For the three atom OF_2 system, the Coulomb and the electron-nuclear attraction integrals are somewhat more challenging for PS integration. This can be seen in comparison to the 2-center integrals for ClF in Figure 2.4, revealing decreased accuracy for the 3-center integrals. Increasing the grid sizes can systematically lower the RMSE, bringing the errors from the smallest to the largest grid from 10^{-6} to 10^{-8} for electron-nuclear attraction, and 10^{-7} to 10^{-9} for the 3-center Coulomb. As will be shown later on, these errors are sufficiently low to allow high-quality wavefunction simulations to be performed. Since the nonrelativistic electronic Hamiltonian under the RI approximation involves only integrals with up to three centers, these RMSE values are expected to also apply to polyatomic systems. That is, even for a polyatomic system, the grid does not need to be extended beyond three centers.

As discussed in Section 2.2.2 and motivated by Figure 2.4, additional discretization in the PS grid around the third center may be helpful for numerical accuracy. The N_{SP} parameter controls this discretization, so the errors in the electron-nuclear attraction integrals were analyzed for $1 \leq N_{SP} \leq 4$. Figure 2.5 shows that $N_{SP} = 2$ yields noticeable improvements, but $N_{SP} > 2$ has little utility, at least for the equilibrium geometry of the OF_2 molecule. Since the spacing between μ grid lines grows with μ, the volume elements around the third center grow at large distances. Therefore we expect that higher N_{SP} might have more utility for centers which are farther from each other. To test this hypothesis, a nonequilibrium geometry for OF_2 was created by moving one fluorine

atom to ~30 times its equilibrium bond distance. $N_{SP} = 3$ significantly improved accuracy over $N_{SP} = 2$, but $N_{SP} = 4$ provided little additional utility. For a molecule with long distances between atoms, the N_{SP} discretization scheme may therefore be useful up to about $N_{SP} = 3$. Quantities supporting these results are given in Figure A.1.

To test the applicability of PS integration on variation in the molecular geometry, a set of paths involving changing nuclear positions were considered. As the geometry changes, the integral values should be smooth and lacking any artifacts from the numerical integration scheme. To do this, two centers are defined: one at the origin and the other displaced by a unit vector in one of the 16 directions. The second center was moved in one of these vector directions until the distance between the centers was 6 Bohr. Figure 2.6 illustrates the value of a 2-center Coulomb integral along this path. All integral profiles are smooth, even for difficult cases with high angular momentum, for instance a pair with f and h functions ($\ell = 3$ and $\ell = 5$) on the bottom right corner of Figure 2.6. A larger list of basis combinations can be found in Figure A.2 that show related results with similar accuracy.

The analysis so far suggests that the PS integration scheme is able to accurately integrate 2- and 3-center quantities of the electronic Hamiltonian. Now, we compare the PS method with the original BP method of the SlaterGPU code. This comparison was performed with relatively similar grid sizes of ~700,000 points. The RMSE obtained for the electron-nuclear and 3-center Coulomb integrals when comparing BP and PS methods is within the same order of magnitude (Table 2.1). The overlap, kinetic, and 2-center Coulomb integrals have improvements in the error of up to three orders of magnitude for PS over BP integration. The improved accuracy of the PS method for 2-center integrals will now be shown to be important for SCF calculations.

The ability to precisely compute integrals with the PS integration method will be a significant advantage to practical electronic structure simulations. Therefore, a variety of polyatomic 2- and 3-atom molecules were examined to analyze the ability of the PS and BP methods to handle larger basis sets, including basis sets with relatively high angular momentum functions. The TZ, QZ, and 5Z basis sets include two d functions (TZ), three d and one f (QZ), and four d and two f (5Z), respectively. As integral accuracy is lower for BP compared to PS integration, there may be noticeable differences in practical electronic structure computations. As a simple test, self-consistent field (SCF) computations at the Hartree–Fock (HF) level were performed. The PS method allows for SCF convergence of all systems in all basis sets explored in

Table 2.2. The BP method, however, performs well for the TZ basis set but is less reliable for the larger basis sets.

To understand why the larger basis sets are much more challenging, we considered the smallest eigenvalues of the overlap matrix for the SO_2 system. For the TZ, QZ, and 5Z basis sets, these values are 1.3×10^{-5}, 9.8×10^{-8}, and 7.1×10^{-8}, respectively. The latter two values are close to the limit of the BP integration accuracy, meaning one or more degrees of freedom in the basis may be poorly behaved. The mixed precision used in the evaluation of BP integrals is believed to contribute to the degradation in performance.[92] PS integration, having accuracies of around 10^{-12} RMSE, experiences no difficulty through 5Z basis sets.

Further tests of the utility of the PS integrals were done for the same molecules in Table 2.2, this time using a correlated post-HF method. High-quality wavefunctions were computed using TZ, QZ, and 5Z basis sets at the HBCI level of theory.[42–45] HBCI provides a close approximation to full CI, recovering all static and dynamic correlation available to the basis. Given that all degrees of orbital freedom are accessed by HBCI, errors in the integrals can cause serious problems in the reliability of the CI procedure. The HBCI calculations in Table 2.3 illustrate the accuracy of the integrals and reference orbitals generated using the PS method. In particular, from TZ to QZ, additional correlation energies of −4.22 mHa/electron on average were found, and from QZ to 5Z, −1.29 mHa/electron, suggesting the relevance of high-quality basis sets for converging these wavefunctions. PS integrals, therefore, were instrumental in achieving accurate results from large Slater basis sets at a correlated level.

Table 2.3: Heat-Bath configuration interaction (HBCI) correlation energies (Ha) for various molecules in TZ, QZ, and 5Z basis sets.

E_{corr} (Ha) using PS integrals with increasing basis			
Mol	TZ	QZ	5Z
HF	-0.2558	-0.2821	-0.3005
C_2	-0.3629	-0.3861	-0.3895
N_2	-0.3646	-0.3960	-0.4091
CO	-0.3477	-0.3829	-0.3935
NO	-0.6962	-0.7309	-0.7487
O_2	-0.4641	-0.5138	-0.5299

HCl	-0.1910	-0.2373	-0.2417
CS	-0.3041	-0.3485	-0.3526
SiO	-0.3247	-0.3646	-0.3738
ClF	-0.4191	-0.4750	-0.4948
Cl_2	-0.3490	-0.4399	-0.4482
H_2O	-0.2517	-0.2821	-0.2912
HCN	-0.3402	-0.3730	-0.3811
OFH	-0.4834	-0.5374	-0.5632
N_3	-0.9796	-1.0304	-1.0537
N_2O	-0.6043	-0.6643	-0.6875
NO_2	-1.1706	-1.2314	-1.2607
SFH	-0.4117	-0.4731	-0.4940
OF_2	-0.7200	-0.7955	-0.8395
SO_2	-0.6140	-0.6965	-0.7196
CS_2	-0.4646	-0.5419	-0.5503

Having found that large Slater basis sets can be used in correlated wavefunction computations, we test the PS integration method further on two statically correlated systems. The first case is a well-studied benchmark[134–140] for electronic structure methods: the singlet-triplet spin gap of methylene (CH_2). The CH_2 transition between $^1A_1$ and $^3B_1$ states were obtained via extrapolation of a series of HBCI computations to the FCI limit with the following HBCI convergence parameters $\varepsilon_{var} = 2 \times 10^{-4}, 1 \times 10^{-4}, 0.5 \times 10^{-4}$ Ha and $\varepsilon_{PT} = 5 \times 10^{-7}$ Ha. Further details are available in Figures A.3 and A.4. The HBCI-STO results obtained are close to Diffusion Monte Carlo (DMC) and internally contracted multireference configuration interaction (CMRCI + Q). Both the HBCI-STO and HBCI-GTO calculations behave well and come within 0.36–0.72 and 0.15–0.51 kcal/mol of the experimental spin gap (Table 2.4).

Table 2.4: Two states of CH_2 ($^1A_1$ and $^3B_1$), at various correlated levels of theory. Geometries for $^1A_1$ and $^3B_1$ CH_2 were obtained from ref. 141 The bases used for the GTO calculations are the cc-pVXZ basis sets, while the STO bases are the same as referenced in Table 2.2. The energy reported under CBS was obtained in the complete basis set limit. Units are in kcal/mol.

Method	TZ	QZ	5Z	CBS^f	Expt.	Basis

HBCI-PS	11.1	9.93	9.72			Slater
HBCI-GTO	10.5	9.71	9.51			Slater
Expt.[a]					9.0	
Expt.[b]					9.36	
SF-CIS[c]	20.4					Gaussian
SF-CIS(D)[c]	14.1					Gaussian
EOM-SF-CCSD(dT)[d]		9.7				Gaussian
VMC[e]	9.92					Slater
DMC[e]	9.36					Slater
CMRCI+Q[f]				8.97		Gaussian
FCI[g]	11.1					Gaussian

[a] Ref. 134.

[b] Ref. 135.

[c] cc-pVTZ, all-electrons correlated.[136]

[d] aug-cc-pVQZ, all-electrons correlated.[137]

[e] TZ2P/Jastrow, all-electrons correlated.[138]

[f] Complete basis set limit, all-electrons correlated.[139]

[g] TZ2P frozen-core.[140]

PS integrals via SlaterGPU are applicable to molecular systems with more than three atoms, as the electronic Hamiltonian can be constructed by computing integrals over subsets of three centers at a time. As an example, incremental FCI (iFCI)[121] computations were run on 1,3-propanediyl to obtain the vertical singlet–triplet gap. iFCI is able to recover impressive amounts of correlation energy at polynomial scaling: all core and valence electrons were correlated within a 225 orbital active space (full CI). When comparing the singlet–triplet gap energies of the iFCI method with CCSD(T), we observe that the predicted energies for the vertical excitation differ by more than 1 kcal/mol. The predicted energy difference can be explained by the use of an unrestricted reference for CCSD(T), as spin contamination can be a problem for open-shell systems,[142,143] in this case likely causing a cancelation of errors. Based on the natural orbitals obtained from the iFCI calculation, the 1,3-propanediyl system has two radical centers located on carbons 1 and 3. Simultaneously, the natural orbital occupation numbers in the ground singlet state indicate the system has significant biradicaloid character (Figure 2.7).

2.5 Conclusion

Leveraging the advancements made in the original SlaterGPU paper,[92] this work reports an efficient numerical integration scheme to allow for high-accuracy construction of electronic structure matrix elements. The two-center PS integrals are around three orders of magnitude more accurate than the prior integration scheme (see Table 2.1), with the 3-center integrals being of similar accuracy. The increased accuracy of the overlap integrals in particular allows for the use of larger basis sets in practical electronic structure simulations, since the integrals generated via BP are inadequate for the convergence of QZ and 5Z basis SCF simulations (cf. Table 2.2). Examples of high precision CI computations demonstrate the practical utility of the new scheme (Tables 2.3 and 2.4, Figure 2.7).

The method presented excels in calculations which require an accurate description of the cusp and exponential wavefunction tails. This is notably beneficial in inverse DFT applications where the cusp conditions can greatly impact the exchange-correlation potential.[71,72] The PS scheme should allow for less numerical artifacts and improve the output obtained from the inverse Kohn–Sham problem.[1,144–150]

Chapter 3
Efficient Configuration Interaction Composite Scheme for Quantitative Thermochemistry of Transition Metal Containing Diatomics

Transition metal systems are notoriously difficult to study due to high static and dynamic correlation. This chapter focuses on developing a composite method using heat-bath configuration interaction (HBCI). Considerations which effect accuracy when making a composite procedure are discussed as well as factors which are specific to the HBCI method. The composite method is tested on the ScH system and is found to achieve TM thermochemical accuracy (+/- 3 kcal/mol of experiment). Two composite procedures are compared here, one which adds semi-core correlation as a correction (valence/cc-pVTZ) and one which directly incorporates semi-core correlation directly in all calculations (semi-core/cc-pwCVTZ). Differences between the corrections (CBS, relativistic, and semi-core) of the valence and semi-core composite methods are found to be similar in magnitude (~0.1-0.5 kcal/mol).

3.1 Introduction

First principles modeling can provide deep physical insight into species composed of main group and transition metal (TM) elements.[151] For thermochemical properties, wavefunction theories can approach or exceed chemical accuracy—defined as being within 1 kcal/mol of the experimental value—but only for main group elements.[152–154] For TMs, the difficulty in making accurate predictions is significantly greater, leading to the suggestion that chemical accuracy for TMs should be redefined as +/- 3 kcal/mol.[155] The challenges with quantum chemical predictions for TMs are multifold: the greater number of electrons concentrated in a small space, the wider possibilities for multiple low-lying charge and spin states, the higher likelihood for mixed-valence configurations to be relevant, and the more diverse bonding patterns that appear with valence d orbitals. Electronic structure methodologies that excel for closed-shell, single-configurational states[156–158] do not necessarily work across a diverse set of TM-containing species. Modeling techniques that take into account interactions between many electrons—including those in near-

degenerate configurations—are needed to make meaningful predictions with uniformly high accuracy.

Full configuration interaction (FCI) gives exact results in a given basis set, but is not feasible in most cases due to its exponentially scaling costs.[31,32,159–163] Practical electronic structure computations therefore truncate this wavefunction; for instance, coupled cluster (CC) methods use an exponential ansatz and excitation level limits to reduce complexity. When the wavefunction is well described with a single reference configuration, chemical accuracy is attainable with lower-excitation single reference methods such as CCSD(T).[154] Since many chemical species involving transition metals require multiple electron configurations to adequately describe the wavefunction, standard methods like CCSD(T) tend to break down in this limit.[156,164] Using higher-excitation-level approximations is a path forward, at substantially increased costs.[158]

In studies of TM diatomics, CC calculations have been performed up to CCSDTQ(P),[158] providing treatment of static correlation beyond simpler CC methods. Due to the severe computational cost ($O(N^{12})$ for CCSDTQ(P)) of high-excitation-level CC models,[165] composite methods have been developed to approximate large basis, full excitation level computations with a series of simpler computations. The correlation consistent composite approach (ccCA)[155,166] and related methods[165,167–174] are examples that work well for weakly correlated chemical species. Related approaches, such as super-ccCA[175] (s-ccCA), include higher-excitation-level coupled cluster models, such as CCSDTQP. The test set for the ccCA-TM method includes 17 TM species[155] (3 with strong multireference character) and reports a mean absolute deviation (MAD) that falls outside of TM chemical accuracy at 5.6 kcal/mol. The test set for the s-ccCA method includes 9 TM diatomics (7 with strong multireference character) and predicts BDEs to within TM chemical accuracy (0.56 kcal/mol MAD).[155,175] These studies noted that VC has strong multireference character; the MAD for this system is 1.35 kcal/mol, which leaves room for some improvement in the description of severely multireference TM systems.[169,176–179]

In addition to the above examples, Cr_2 has been a notoriously difficult system to describe with correlated wavefunction methods.[180] Work from Umrigar[181] has substantially improved the description of the chromium dimer potential energy curve through the use of a heat-bath configuration interaction (HBCI) and density matrix renormalization group (DMRG)[182,183] composite method. The composite method applied to the chromium dimer closely approached the experimental bond dissociation energy (to within 0.02 eV) and significantly refined the predicted

potential energy profile.[181,184] Many other examples used to tackle the chromium dimer problem are conveniently listed in refs. 181,185,186.

HBCI and DMRG can systematically approach the FCI limit by tightening their convergence parameters without enforced limits to excitation level. The former technique, HBCI, is a select CI method which combines a variational CI space selection with perturbation theory (SCI+PT)[33,34] and closely approximates the FCI result. Earlier SCI techniques such as configuration interaction by perturbatively selecting iteratively (CIPSI)[24,35–38,187–191], which was the first SCI+PT method, inspired later algorithms such as HBCI[42–45,47] and adaptive sampling configuration interaction (ASCI)[39–41,192–196]. These techniques in recent years have become more mature, making use of high-performance, parallel computing architectures. In this neighborhood of FCI-like approximations, Quantum Monte Carlo-FCI[197,198] (QMC-FCI) also strives to approach FCI results.

This work will employ a modern implementation of HBCI,[42–45,47] particularly a recent highly parallel algorithm created by our group.[45] HBCI includes electronic configurations that are important to describe static correlation at a variational level, including higher-excitation-level configurations that are necessary to quantitatively describe the wavefunction accurately in the case of TMs (~2% of configurations in the wavefunction go beyond 6+ excitations for ScH). The parallel implementation of HBCI developed by our group now permits larger CI calculations than previously attainable, providing an avenue to investigate small TM species to higher accuracy than before.[45] This is achieved by making effective use of distributed memory in modern supercomputing architectures through an optimized code that can scale to thousands of compute cores.

In the present study, the TM diatomic ScH will be examined. The insights emerging from this work will inform a composite HBCI method which targets TM systems that have severe multireference character based on the T_1, D_1, and %TDA diagnostics.[156,167,199,200] The accurate wavefunctions from HBCI provide insight into the characteristics of electronic states, which are important for determining the stability and subsequently the catalytic activity among other properties of interest for a material.[201] The densities of these systems are also computed and may make for an interesting exploration into accurate exchange-correlation potentials of TM-containing systems using methods developed in the Zimmerman group.[1,71,72]

3.2 Theory

HBCI operates by using a variational step to capture the dominant contributors to the wavefunction, followed by a perturbative step to recover dynamic correlation. Since HBCI has been introduced and developed in prior works, refs. 42–45 provide additional details for the interested reader. The key components of HBCI are nonetheless described here to give an overview of the method.

3.2.1 Variational Step

The variational step begins with a relatively small set of reference determinants (in our case via complete active space CI (CAS-CI)) to define the initial wavefunction and Hamiltonian. Upon diagonalization of this reference Hamiltonian, the initial set of CI coefficients (c_i) are available, and the determinant space is expanded iteratively. The threshold ε_{var} allows for adjustable accuracy through a user-defined threshold that determines which configurations are included, via

$$|H_{ki}c_i| > \varepsilon_{var} \tag{3.1}$$

where H_{ki} is the Hamiltonian element connecting the determinant with index k (outside of the current configuration space) to the variational space's determinant of index i, and c_i is the CI coefficient associated with the latter determinant. Any configurations that satisfy equation 3.1 are added to the wavefunction, which is then diagonalized to give c_i in the current variational space. The process of diagonalization followed by adding determinants is repeated until a satisfactory variational wavefunction is assembled.[42] Usually, ε_{var} is chosen to produce a relatively refined wavefunction, such that the remaining configurations fall into a perturbative regime.

3.2.2 Perturbative Step

A perturbative correction to the variational energy is then performed using a modified Epstein-Nesbet (EN-PT)[46,202] step,

$$\Delta E^{(2)} \approx \sum_k \frac{\left(\sum_i^{(\varepsilon_{PT})} H_{ki}\, c_i\right)^2}{E_{var} - H_{kk}} \tag{3.2}$$

Where H_{kk} is a Hamiltonian element located outside of the variational space and E_{var} is the variational energy. Compared to standard EN-PT, equation 3.2 only considers variational-external couplings that exceed threshold ε_{PT}, which is chosen to be a few orders of magnitude smaller than

ε_{var}. This is denoted by the restriction on the sum, $\sum_i^{(\varepsilon_{PT})}$ ..., which indicates that each term is added only if $|H_{ki}c_i| > \varepsilon_{PT}$. Given the much tighter threshold compared to the variational step, many more determinants are included in the PT step. The tight threshold, along with the requirement that the sums in the numerator are stored, makes the PT step the memory-limiting step of the HBCI algorithm.

3.2.3 Parallelization

Parallelization of our group's HBCI algorithm uses a combination of MPI and OpenMP techniques to distribute the variational and perturbative workloads across nodes. In particular, a 2D hash table over alpha and beta strings[45] allows for even distribution of pieces of the wavefunction and Hamiltonian. For the perturbative step, assigning hash ranges of the PT determinants to specific processes ensures that the sums in equation 3.2 do not require communication operators across nodes. This makes the PT step, which is the most memory and compute-expensive step, highly parallel. An additional advantage of using the hash table is the ability to store and work on segments of the PT space asynchronously, greatly reducing the memory requirements. During the variational step, communication between nodes is required to ensure duplicate determinants do not enter the wavefunction, and that the CI diagonalization procedure results in the same wavefunction on all nodes. This is achieved through periodic merging, sorting, and duplicate deletion across all MPI processes. With the combined MPI+OpenMP parallel setup, only one copy of the variational wavefunction is needed on each compute node. See ref. 45 for more detailed information on the inner workings of this HBCI algorithm.

3.2.4 Bond Dissociation Energy Procedure

Since HBCI spans the entire Hilbert space, it follows that as one reduces the ε_{var} cutoff values, one converges to the FCI energy. It has been assumed that given an ε_{var} which is small enough, the FCI energy is approached linearly with respect to the variational vs. perturbative energy. This extrapolation procedure is utilized in determining the BDE of the TM diatomics studied in this work. For the interested reader, a rationale for this extrapolation, as well as an alternative extrapolation function are discussed by Burton and Loos.[203]

While HBCI is significantly cheaper than FCI, it is still computationally intensive if one desires quantitative results. As such, the semi-core, complete basis set extrapolation, and

relativistic effects are treated as a correction through the procedure detailed in Figure 3.1. Relativistic effects are considered with a single HBCI calculation in the cc-pVTZ-DK basis using the 1eX2C method, and the correction is added to the reference TZ energy.

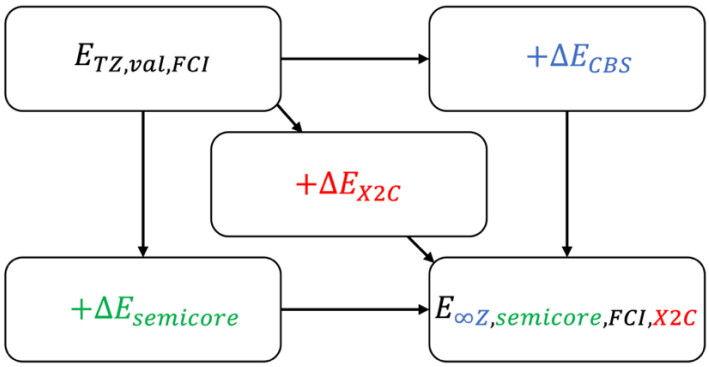

Figure 3.1: Process for correcting BDEs in valence calculations in a finite basis, through addition of independent semi-core and complete basis set limit corrections.

The complete basis set (CBS) limit correction is calculated using double through quadruple-zeta valence basis sets. Further, each system in each basis is extrapolated to the FCI limit at three ε_{var} values; these FCI extrapolated energies are used in the CBS extrapolation. CBS Extrapolation was performed using the X^{-3} method defined by Helgaker:[204,205]

$$E_{XZ} = E_{\infty Z} + AX^{-3} \tag{3.3}$$

Where X is a cardinal number based on the zeta value of a given basis set (DZ = 2, TZ = 3, …) and A is a fitting parameter where calculations in an array of basis sets can be run to approximate $E_{\infty Z}$.[206,207] The difference between the ∞Z and the TZ energies is determined for both the diatomic and single-atom ground-state systems.

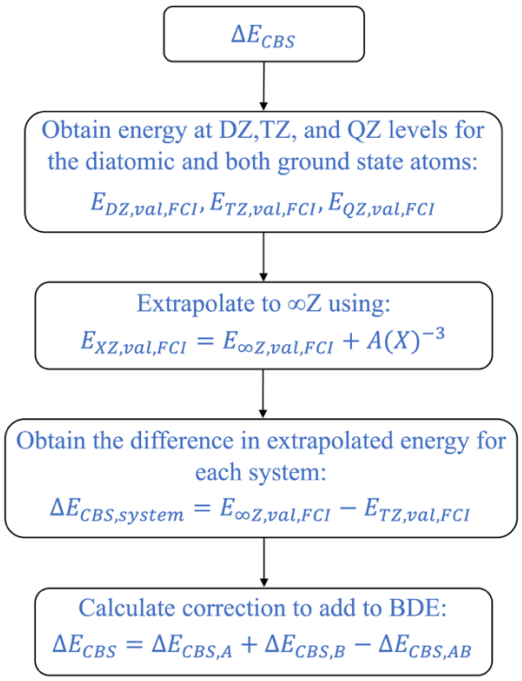

Figure 3.2: Process for obtaining the CBS correction, A, B and AB denote both single atoms and the diatomic.

While the core and semi-core electrons do not directly participate in changes to bonding, correlation between the valence and the semi-core electrons can have a significant effect on the energy required for dissociation; this is referred to as the semi-core correlation energy. In addition, correlating semi-core electrons can swiftly increase the computational cost. For this reason, the semi-core correlation energy from the variational step of HBCI ($E_{tot}(CVTZ) - E_{tot}(VTZ)$) is FCI extrapolated using 5 points and loose ε_{var} ($6 \times 10^{-4}\, Ha$, $7 \times 10^{-4}\, Ha$, $8 \times 10^{-4}\, Ha$, $9 \times 10^{-4}\, Ha$, $1 \times 10^{-3}\, Ha$) (Fig. 3.3); the configurations with leading coefficients are checked to ensure proper state targeting. The semi-core and valence energy for the diatomic and both ground-state single-atoms are computed at a core-correlated triple-zeta level. For ScH (Figure 3.3), the amount of semi-core correlation energy recovered heavily depends on the number of points used in the extrapolation.

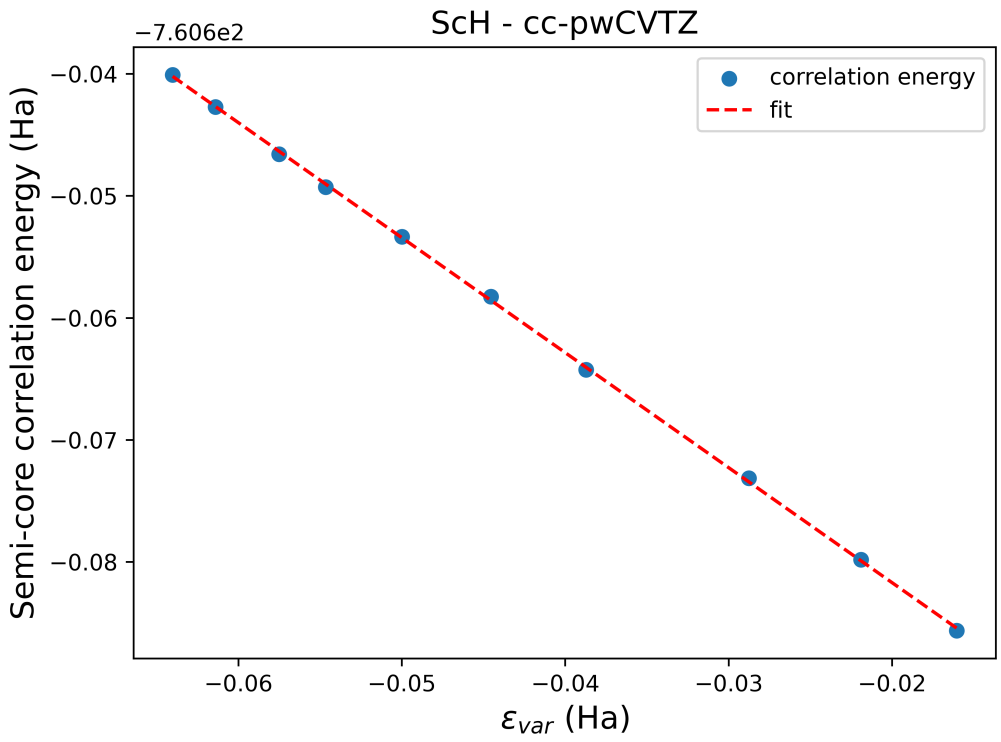

Figure 3.3: Semi-core correlation extrapolation for ScH with varying ε_{var}, all points are linearly fit.

3, 4, and 5-point extrapolations are tested for precision by extrapolating with different sets of points from the 10 shown in Figure 3.3. The 3-point extrapolations were taken at ε_{var} values of $[1 \times 10^{-3}\ Ha, 9 \times 10^{-4}\ Ha, 8 \times 10^{-4}\ Ha]$, $[9 \times 10^{-4}\ Ha, 8 \times 10^{-4}\ Ha, 7 \times 10^{-4}\ Ha]$, $[8 \times 10^{-4}\ Ha, 7 \times 10^{-4}\ Ha, 6 \times 10^{-4}\ Ha]$, $[7 \times 10^{-4}\ Ha, 6 \times 10^{-4}\ Ha, 5 \times 10^{-4}\ Ha]$, $[6 \times 10^{-4}\ Ha, 5 \times 10^{-4}\ Ha, 4 \times 10^{-4}\ Ha]$, $[5 \times 10^{-4}\ Ha, 4 \times 10^{-4}\ Ha, 3 \times 10^{-4}\ Ha]$, $[4 \times 10^{-4}\ Ha, 3 \times 10^{-4}\ Ha, 2 \times 10^{-4}\ Ha]$, $[3 \times 10^{-4}\ Ha, 2 \times 10^{-4}\ Ha, 1.25 \times 10^{-4}\ Ha]$. The 4-point extrapolations were taken at ε_{var} values of $[1 \times 10^{-3}\ Ha, 9 \times 10^{-4}\ Ha, 8 \times 10^{-4}\ Ha, 7 \times 10^{-4}\ Ha]$, $[9 \times 10^{-4}\ Ha, 8 \times 10^{-4}\ Ha, 7 \times 10^{-4}\ Ha, 6 \times 10^{-4}\ Ha]$, $[8 \times 10^{-4}\ Ha, 7 \times 10^{-4}\ Ha, 6 \times 10^{-4}\ Ha, 5 \times 10^{-4}\ Ha]$, $[7 \times 10^{-4}\ Ha, 6 \times 10^{-4}\ Ha, 5 \times 10^{-4}\ Ha, 4 \times 10^{-4}\ Ha]$, $[6 \times 10^{-4}\ Ha, 5 \times 10^{-4}\ Ha, 4 \times 10^{-4}\ Ha, 3 \times 10^{-4}\ Ha]$, $[5 \times 10^{-4}\ Ha, 4 \times 10^{-4}\ Ha, 3 \times 10^{-4}\ Ha, 2 \times 10^{-4}\ Ha]$, $[4 \times 10^{-4}\ Ha, 3 \times 10^{-4}\ Ha, 2 \times 10^{-4}\ Ha, 1.25 \times 10^{-4}\ Ha]$. The 5-point extrapolations were taken at ε_{var} values of $[1 \times 10^{-3}\ Ha, 9 \times 10^{-4}\ Ha, 8 \times 10^{-4}\ Ha, 7 \times 10^{-4}\ Ha, 6 \times 10^{-4}\ Ha]$, $[9 \times 10^{-4}\ Ha, 8 \times 10^{-4}\ Ha, 7 \times 10^{-4}\ Ha, 6 \times 10^{-4}\ Ha, 5 \times 10^{-4}\ Ha]$, $[8 \times 10^{-4}\ Ha, 7 \times 10^{-4}\ Ha, 6 \times 10^{-4}\ Ha, 5 \times 10^{-4}\ Ha, 4 \times 10^{-4}\ Ha]$, $[7 \times 10^{-4}\ Ha, 6 \times 10^{-4}\ Ha,$

$5 \times 10^{-4}\ Ha, 4 \times 10^{-4}\ Ha, 3 \times 10^{-4}\ Ha]$, $[6 \times 10^{-4}\ Ha, 5 \times 10^{-4}\ Ha, 4 \times 10^{-4}\ Ha, 3 \times 10^{-4}\ Ha, 2 \times 10^{-4}\ Ha]$, $[5 \times 10^{-4}\ Ha, 4 \times 10^{-4}\ Ha, 3 \times 10^{-4}\ Ha, 2 \times 10^{-4}\ Ha, 1.25 \times 10^{-4}\ Ha]$. The 3-point extrapolations varied in a range of 6.1 mHa, the 4-point extrapolations had a range of 2.3 mHa, and the 5-point extrapolations had a range of 1.8 mHa. The 5-point extrapolation allows for acceptable error and reasonable cost for larger TM systems.

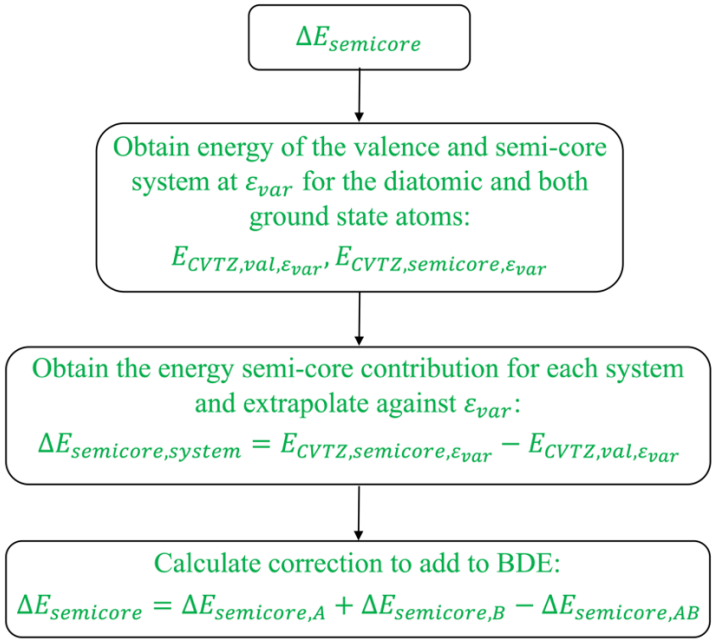

Figure 3.4: Process for obtaining the semi-core correction, A, B and AB denote both single atoms and the diatomic.

3.3 Computational Details

The ZEST software package was used to perform HBCI calculations, including CBS, relativistic, and semi-core corrections. Equilibrium bond distances were obtained from the Computational Chemistry Comparison and Benchmark DataBase (https://cccbdb.nist.gov/). All basis sets used in this work were obtained from Basis Set Exchange.[208–210]

Relativistic effects[15,211,212] such as scalar relativistic effects and spin-orbit interactions, significantly modify the electronic structure of transition metal species. Prior works[213] have shown that scalar relativistic effects can influence BDEs by ~3 Ha for Scandium, and even more for other TMs. In this work, an exact two-component (X2C)[17,19,214–216] model will be used to account for scalar relativistic effects. 1eX2C contributes one-electron relativistic corrections based on block diagonalization of the four-component Dirac equation, where the electronic part of the Dirac Hamiltonian is used. Spin-orbit effects are neglected in this model, though these could be

accounted for perturbatively through methods described in ref. 217. The ε_{var} and ε_{PT} used for correction were $1.25 \times 10^{-4}\ Ha$ and $1 \times 10^{-7}\ Ha$, respectively.

For the semi-core correction, the cc-pwCVTZ[218,219] basis was used for adequate description of core electrons. Semi-core correlation is necessary for these TM systems as core excitations contribute a significant amount of correlation energy; as such, all TMs are correlated to the Neon core, and light atoms have a frozen core extending to the previous row (S has a Neon core, O has a Helium core). In this work, for the analysis of ScH, the chosen variational epsilon thresholds for extrapolation are $1 \times 10^{-3}\ Ha$, $9 \times 10^{-4}\ Ha$, $8 \times 10^{-4}\ Ha$, $7 \times 10^{-4}\ Ha$, and $6 \times 10^{-4}\ Ha$.

NOs are a crucial part of the convergence process as they allow the basis to better describe the wavefunctions response to correlation; this makes the actual HBCI calculation faster and more efficient using the same or fewer determinants. The number of states selected for targeting in HBCI is 2 for diatomics and 4 for single-atom TMs because diatomic systems typically have greater splitting than single atoms. The ε_{var} threshold used to obtain NOs is $1.25 \times 10^{-4}\ Ha$.

Basis set extrapolation was performed with only the valence space unfrozen using the cc-pVXZ[219–221] basis sets. In this work, the CBS extrapolation defined in equation 3.3 is used to obtain the energy at ∞Z; this extrapolation technique requires 2 points. Other extrapolation procedures with different benefits are available and cited for the interested reader.[204,205,222]

HBCI computations were extrapolated to the FCI limit using a linear fit procedure. In this procedure, one varies the ε_{var} threshold of the HBCI calculation while keeping all other settings consistent. When a sufficient amount of the Hilbert space is recovered, the trend between variational and perturbative energy recovery is linear and can be extrapolated to the FCI energy to high accuracy. For the basis set extrapolation calculations, the FCI limit was obtained in each basis using three ε_{var} values of $1.25 \times 10^{-4}\ Ha$, $1.5 \times 10^{-4}\ Ha$, and $1.75 \times 10^{-4}\ Ha$, with an ε_{PT} of $1 \times 10^{-7}\ Ha$.

3.4 Results and Discussion

The results in this section detail the general (to wavefunction theory) and unique (to HBCI) challenges which arise when applying HBCI to these difficult TM systems. This task is nontrivial as it requires careful choice of basis, a choice of the semi-core electrons to unfreeze, whether the Resolution-of-the-Identity (RI) approximation is appropriate, and the choice of method for handling relativistic effects. There are also choices for HBCI specifically, such as what variational

threshold to choose for NO generation, thresholds for the variational and perturbative steps, and how many states are necessary to target. For the 1eX2C procedure, relativistic effects cannot be reliably incorporated into all calculations, as variationality becomes precarious (even in the correlation-consistent Dunning family of basis sets) (Figure 3.5).

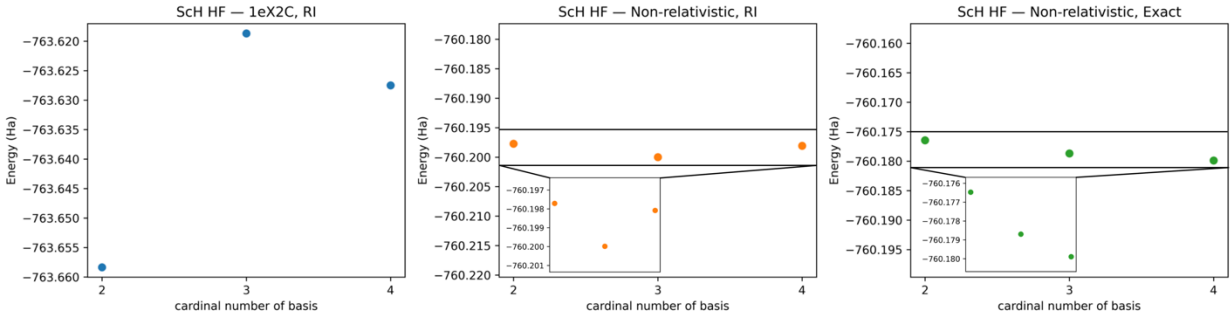

Figure 3.5: Hartree-Fock energies (Ha) for the ScH system with relativistic effects and RI approximation toggled, basis sizes ranging from DZ-QZ are evaluated.

In principle, X2C is variational so long as the electron repulsion integral (ERI) matrix is also transformed like the core Hamiltonian; however, this process can be more expensive due to the N^4 size of the ERI matrix. There are alternative methods for X2C which approximate the 2-electron terms[20,217,223,224], which is left for future implementation in the ZEST software package. The results in Figure 3.5 illustrate that considering relativistic effects can increase the complexity and hinder recovery of the CBS correction unless considered exactly, which further justifies the use of composite methods. Figure 3.6 illustrates how the 1eX2C method can reorder the valence space orbitals depending on the basis used. Particularly interesting is the HOMO in the DZ basis; the d orbital interacts with the s orbital of the hydrogen; meanwhile, for the TZ and QZ basis it becomes nonbonding. In contrast, the HOMO orbitals in the non-relativistic calculation are all nonbonding. Another feature lies in both TZ HOMO-1 orbitals, where they differ from those of the DZ and QZ, which will explain later the bias of CASSCF towards undesired states. In this method, 1-electron relativistic effects cannot be considered in all calculations as they will interfere with the CBS extrapolation, and so are considered via a single TZ calculation at $\varepsilon_{var} = 1.25 \times 10^{-4}\ Ha$ and $\varepsilon_{PT} = 1 \times 10^{-7}\ Ha$.

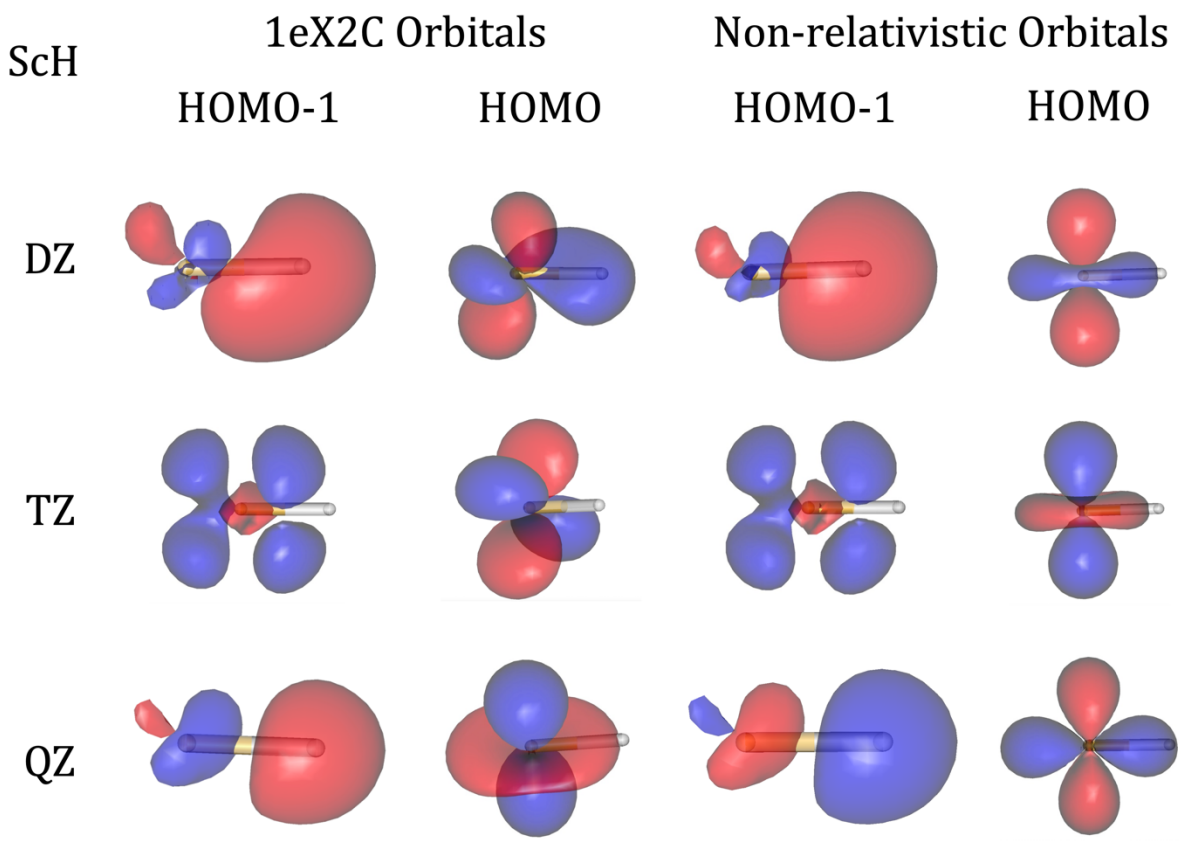

Figure 3.6: Hartree-Fock MOs of the ScH system showing HOMO and HOMO-1 orbitals for 1eX2C and nonrelativistic calculations across basis sets.

The RI approximation was also compared to exact 4-center integrals, and the Dunning auxiliary basis sets available for TMs were found to produce errors of ~20 mHa in the scandium atom at the cc-pVQZ level using the cc-pVQZ-RIFIT auxiliary basis (Figure 3.5). The ScH system is also seen to be poorly described using integrals generated by the auxiliary set, as the energy does not reliably decrease with basis size. One might find it intuitive to recover some correlation before generating the NOs in the HBCI step to help bias the system towards the correct state; however, it is seen here that problems such as root flipping can occur in CASSCF and hinder state targeting across basis sets. Even with exact 4-center integrals, differences between basis sets (DZ, TZ, QZ) chosen for CBS extrapolation can fall into local minima in CASSCF. This can interfere with the quality of the generated NOs and subsequently the HBCI calculation (Figure 3.7).

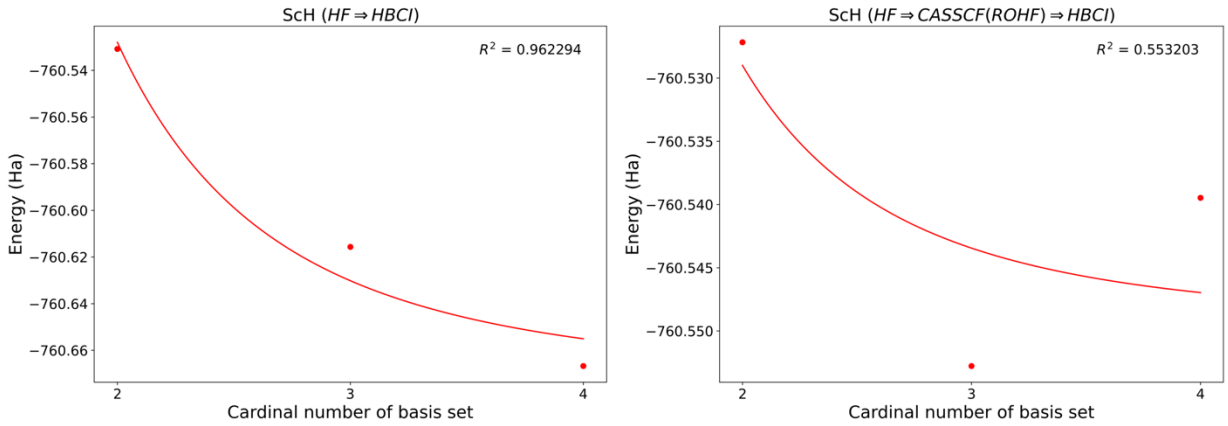

Figure 3.7: Basis set extrapolation HBCI energies for ScH where one procedure uses the HF as reference orbitals (left) and the other uses orbitals generated via CASSCF(2,1) as reference. Both calculations are correlated to the Ne core.

If HF orbitals are directly fed into HBCI, and the NO basis is generated, these errors arising from CASSCF are not present, suggesting it is important to consider a certain number of configurations before producing NOs for the orbitals to be consistent across basis sets. Since the NO basis depends upon the included configurations, the HBCI variational threshold used for NO generation must be kept constant across all calculations to ensure consistent formation of the NO basis. If the NOs sufficiently describe the space with a chosen threshold, they can reliably separate states with moderate degeneracy such as the $^1\Sigma^+$ or $^3\Delta$ states of ScH. If a system contains severe degeneracy, such as CrO in which the two lowest states are separated by roughly 1 mHa, then root flipping can occur. This problem can be corrected by running the calculation to target multiple states, and if the ground state NOs are not that of the true ground state, one can instead select state-specific NOs. Since the NOs are formed from determinants in only the variational space, the NO variational threshold can be set much lower compared to a calculation which applies the perturbative correction (the subsequent calculation in this case), resulting in a more accurate NO basis.

In the HF to HBCI procedure (Fig. 3.7 (left)), the basis set extrapolation is not to the desired accuracy, as the R^2 is 0.96 and the y-axis is plotted over >0.1 Ha. This can be explained by the correlation of electrons to the Ne core while using the cc-pVXZ basis. The X^{-3} extrapolation procedure requires a basis set which is paired with the amount of core correlation present, cc-pwCVXZ for semi-core and cc-pVXZ for valence only. An excitation analysis was also performed

on the ScH system, which is displayed in Table 3.1, detailing the number of electrons excited in each configuration included in the wavefunction. This shows directly that high excitation energetically significant configurations are required to accurately describe transition metal systems. The s-ccCA method uses CCSDTQP, but a significant percentage of configurations which contribute to the wavefunction (at $\varepsilon_{var} = 1.25 \times 10^{-4}$) are sextuple excitations or greater. The s-ccCA method considers CBS, relativistic effects, semi-core correlation, and zero-point vibrational energy (ZPVE), and they emphasize that what is missing from a more accurate description is the addition of more configurations/excitations.

Table 3.1: The percentage of total configurations which contribute to the wavefunction are given for different basis sets and numbers of frozen electrons. The ScH(val) was run in the cc-pVQZ basis with the valence electrons unfrozen. The ScH(core) was run from cc-pVDZ through cc-pVQZ with electrons down to the Ne core correlated. All HBCI calculations were run with $\varepsilon_{var} = 1.25 \times 10^{-4}$ Ha.

	Basis (ScH(core))			System(QZ)	
Excitations	DZ	TZ	QZ	ScH(val)	ScH(core)
1	0.0633	0.0499	0.0454	0.338	0.0454
2	5.23	7.33	10.1	27.2	10.1
3	27.6	25.5	23.3	43.5	23.3
4	59.6	61.7	62.2	28.9	62.2
5	4.49	3.08	2.40	0	2.40
6	2.97	2.34	2.01	0	2.01
7	0.0122	0.0055	0.0032	0	0.0032
8	0.0004	0.0002	0.0001	0	0.0001
9	0	0	0	0	0

The ScH system with the valence space correlated only has up to quadruple excitations, as the valence space is only occupied by 4 electrons. It is observed that for the ScH system, roughly 2% of energetically sufficient configurations which have 6+ excitations (above $1.25 \times 10^{-4} Ha$) contribute to the wavefunction, corroborating the interpretation of Welch et al.[175]

As a proof of concept the procedure detailed in the methods section was applied to the ScH system due to it being the smallest possible diatomic which includes a transition metal, and because it has relatively low correlation compared to other TM systems, as is seen in the SI of Jiang et al.[156] Hydrogen is not included in the analysis of the CBS scheme here, as it can be solved for exactly

and included in the BDE analysis later. The FCI extrapolation of each component of this system had an $R^2 > 0.999$, suggesting that the variational and perturbative threshold are satisfactory. The Helgaker X^{-3} basis set extrapolation procedure yielded similarly, an $R^2 > 0.99$ for ScH, indicating that the HBCI algorithm settled on the correct states in each basis set (Fig. 3.8). Scandium has an R^2 of 0.85; however, this is not an issue considering that the energies are plotted over a sub-mHa range. The QZ calculation is lower than the extrapolated value by ~60 μHa; as such, the QZ value is used here rather than the extrapolated value. This should not meaningfully impact the BDE analysis.

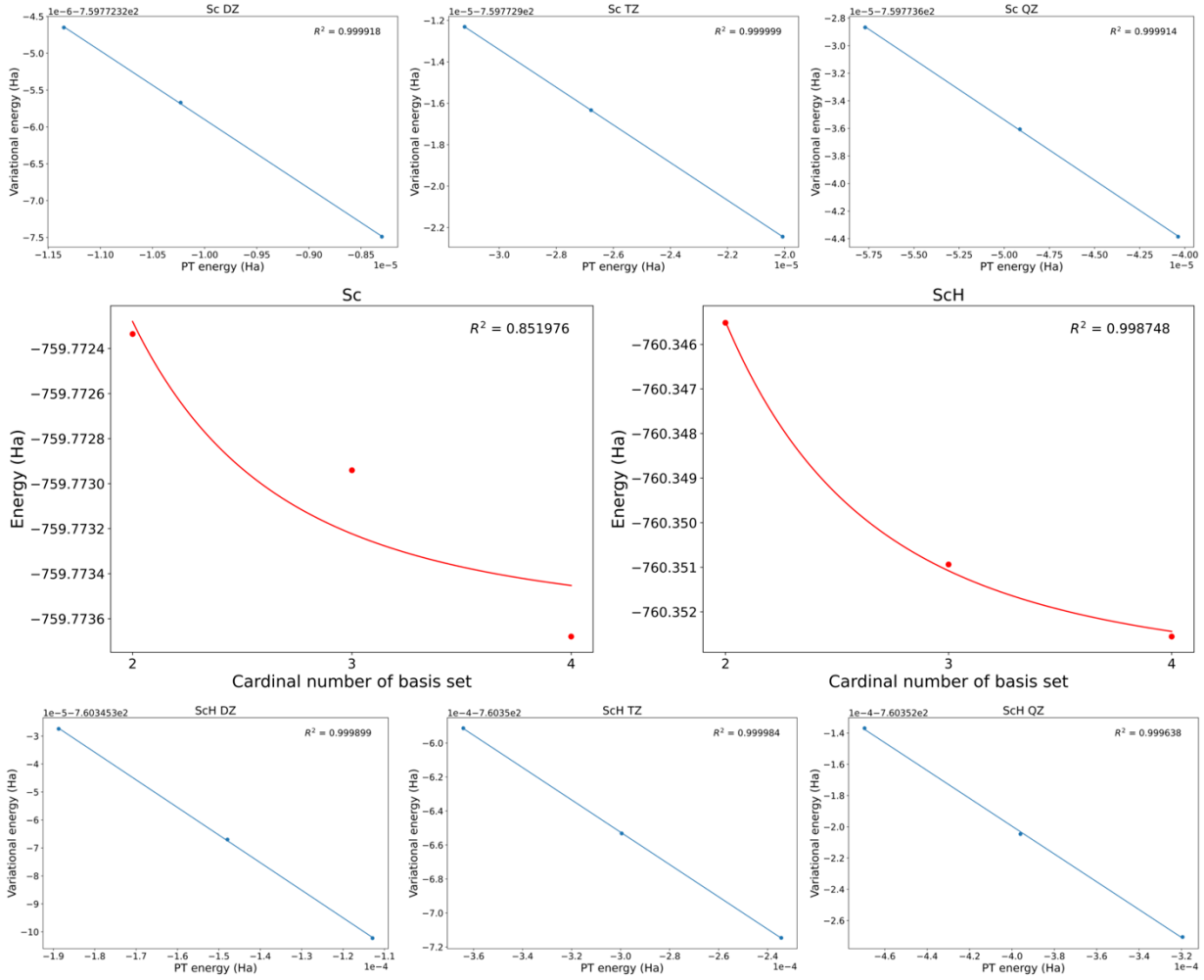

Figure 3.8: FCI extrapolation for Sc (top) and ScH (bottom) as well as CBS extrapolation for both systems (middle). Energies are in Hartree.

Since ScH has only 12 electrons correlated, it is feasible to run an extrapolation in the cc-pwCVXZ basis (where X here is T and Q), directly including semi-core contributions into every

calculation in the composite method. The procedure to directly include the semi-core is then: FCI extrapolate in the CVTZ and CVQZ basis sets for the TZ reference and CBS correction, then run a semi-core relativistic calculation in the cc-pwCVTZ-DK basis at $\varepsilon_{var} = 1.25 \times 10^{-4}$ for the relativistic correction. The cc-pwCV∞Z CBS extrapolation can be found in the SI (Figure B.2). Energies are given for each contribution in the composite calculation and compared to an experimental literature value (which accounts for the ZPVE) as well as another theoretical prediction (Table 3.2).

Table 3.2: Total energies, TZ, and correction contributions for the Sc and ScH systems are given in Ha. BDEs are given in the bottom half of the table (in kcal/mol), differences between the Sc and ScH corrections are also given (in kcal/mol).

Methods (ScH (Ha))	TZ	CBS	Semi-core	Relativistic	Total Energy
cc-pVTZ	-760.3509	-0.00250	-0.3443	-3.4111	-764.1088
cc-pwCVTZ	-760.7017	-0.0234	-	-3.3485	-764.0736
Methods (Sc (Ha))					
cc-pVTZ	-759.7729	-0.000739	-0.3411	-3.4104	-763.5251
cc-pwCVTZ	-760.1171	-0.0220	-	-3.3471	-763.4862

Methods (kcal/mol)		Sc(CBS)-ScH(CBS)	Sc(Semi)-ScH(Semi)	Sc(Rel)-ScH(Rel)	BDE
cc-pVTZ		1.104	4.402	0.4393	54.9
cc-pwCVTZ		0.8785	4.142	0.8785	54.8
CCSD(T)[a]					52.3
Expt.[b]					55.0(±3)

[a] CBS, semi-core, ZPVE, Relativistic and spin-orbit effects included, non-relativistic energy in awc5z basis. [225]

[b]Ref. 226

The energies for Sc and ScH are given in Hartree, and here we can see the relativistic effects contribute the most in terms of magnitude to the total energies for Sc and ScH. In the lower half of the table, the BDEs (in kcal/mol) are predicted to within TM thermochemical accuracy (+/- 3 kcal/mol) while only correlating the valence space. The differences between the Sc and ScH

corrections for the valence/cc-pVTZ and semi-core/cc-pwCVTZ methods are also given to estimate where the differences in the predicted BDEs arise (energies are given in kcal/mol). The semi-core contribution to the energy was included in the TZ energy for the cc-pwCVTZ method, and so when calculating the differences, the following expression was used to populate the semi-core correction column.

$$\big(CVTZ(Sc) - VTZ(Sc)\big) - \big(CVTZ(ScH) - VTZ(ScH)\big) \tag{3.4}$$

The differences between the cc-pVTZ and cc-pwCVTZ methods for each correction are of roughly the same magnitude, in different directions. More systems will need to be studied to determine the errors of corrections over a broad set of TM systems; however, these results provide a framework for future testing and modifications to the HBCI composite approach. Alternative methods for handling these corrections, such as consideration of 2-electron X2C and spin-orbit coupling, or alternative forms of FCI or CBS extrapolation, could bring this procedure towards reliable TM chemical accuracy (+/- 3 kcal/mol) and perhaps even chemical accuracy (+/- 1 kcal/mol).

3.5 Conclusion

This chapter presented a framework for a new composite method using HBCI. Challenges with incorporation of CBS extrapolation, 1eX2C, the RI approximation, and semi-core correlation were discussed with suggestions on improvement. Some possibilities include the use of X2C methods which consider 2-electron contribution and spin-orbit effects. This work does not test the use of larger RI basis sets; using the cc-pVQZ-RIFIT auxiliary basis, errors of ~20 mHa were present for ScH; in principle, with a larger auxiliary basis, this error should decrease. The method outlined in section 3.2.4 was applied to the ScH system and resulted in BDE prediction (54.9 kcal/mol) which lies within TM thermochemical accuracy (Experiment: 55.0 kcal/mol). Correction differences between the cc-pVTZ and cc-pwCVTZ methods were found to be of similar magnitude (~0.1-0.5 kcal/mol). Future iterations of this composite procedure will focus on finding more effective ways to incorporate relativistic effects, CBS extrapolation, and semi-core contribution into the BDE.

This procedure pioneers the way towards TM thermochemical accuracy (+/- 3 kcal/mol) and beyond for 3d TM systems. There are also possibilities for unique analysis of the excitation pattern of these TM systems compared to main group systems using the HBCI method. If more is understood about specific excitation contributions to the wavefunction, it could inspire variations

on the HBCI method. This work also assists in the acquisition of exchange-correlation potentials via inversion methods, as reliable procedures for FCI methods are required to obtain accurate densities for inverse density functional theory.

Chapter 4
The Kohn-Sham Potential and Bonding at a Conical Intersection

This chapter gives the first view of the Kohn-Sham potential at a conical intersection (CI) using an inverse DFT procedure, which modifies the orbital averaging procedure developed by Khanna et al.[1] The Kohn-Sham potential, Kohn-Sham orbitals, and classical turning surface are all analyzed to determine if the bonding is indicative of dissociation of the H_3 and NH_3 systems at a CI. The dynamics of the H_3 and NH_3 systems are known to dissociate through a CI, which is helpful to inform the analysis of the KS potential. It is determined that the KS potentials at a CI contain dissociative features at certain linear combinations of both adiabatic wavefunctions in the H_3 and NH_3 systems and resemble KS potentials which would be observed for dissociative geometries which occur away from a CI.

4.1 Introduction

In the adiabatic framework, conical intersections (CI)[227] are points where two adiabatic potential energy surfaces (PES) are energetically degenerate. At a conical intersection, the electronic and nuclear motion are strongly coupled, resulting in a breakdown of the Born-Oppenheimer (BO) approximation. CIs are represented as a 2D subspace of the 3N-6 coordinates of a molecule, known as the branching plane, forming a cone-shaped PES centered at the degeneracy. The branching plane is specifically composed of the gradient difference (DG) vector ($g_{IJ}(R) = \nabla \mathrm{E}_J(R) - \nabla \mathrm{E}_I(R)$) and the non-adiabatic coupling (NAC) vector ($f_{IJ}(R) = \frac{\langle \Psi_I(r,R) | \nabla \mathrm{H} | \Psi_J(r,R) \rangle}{E_J - E_I}$) where r is electronic position, and R is nuclear position; these vectors couple electronic and nuclear motion and define the branching plane. The remaining $N-2$ internal degrees of freedom (DOF) define the seam space orthogonal to the branching vectors. Motion within the seam space moves a CI but does not break degeneracy, such that the seam space DOF can be optimized to a point known as the minimum energy CI (MECI).

As pointed out by Yarkony, CIs are not exceptional, but a normal feature of BO potential energy surfaces.[228] Considerable effort has been made to improve the accuracy with which CIs can be described while at the same time reducing computational costs so larger systems can be studied.[229] The accuracy of a method can be gauged by whether it is able to correctly define the topology and topography of a CI. The term topology refers to the dimensionality of the seam space, while the term topography refers to the shape of the PESs near a CI. CIs have significant static correlation due to the inherent degeneracy, requiring methods which can describe both states on an equal footing. Full configuration interaction (FCI) is conceptually simple and can handle the degeneracy of a CI by recovering all correlation. FCI works by incorporating all possible configurations in a basis into the wavefunction, which scales combinatorially with system size. CASSCF is a cheaper alternative which is popular because it can directly couple both configurations at a CI and optimizes the orbitals accordingly. While CASSCF scales the same as FCI (if the active space is defined as all orbitals and all electrons), it gives the freedom to choose an active space where all configurations are considered in a range of user-defined orbitals. The Hamiltonian from these multireference methods is Hermitian, which was shown by Hättig[230] to be essential for a method to correctly predict the topology and topography of a CI.

Density functional theory (DFT) methods stand out for their low cost; however, special care must be taken at conical intersections to ensure an accurate description.[231–233] In principle, there is a Kohn-Sham DFT (KS-DFT) solution which exactly accounts for the exchange and correlation and results in an exact solution; in practice, however, most DFT functionals struggle to define the topography/topology of a CI. In the case of linear response time-dependent density functional theory (LR-TDDFT),[234] the elements which couple both states are expressed in a way which causes negative coupling elements to appear when approaching a CI, resulting in catastrophic surfaces.[235] TDA-TDDFT uses the Casida formulation similar to LR-TDDFT but sets the coupling elements to 0; the intersections of a CI in these cases occur in $N-1$ dimensions. Despite not describing the topology or topography of a CI properly, TDA-TDDFT can predict the energy gap at a MECI geometry of butadiene as 0.3 eV, which is similar to predictions with CASSCF.[231] DFT methods (and single reference methods in general) are most commonly modified to describe CIs by considering coupling between both states in some way.[235–240] This raises the question of how well these functional approximations capture the exchange-correlation (XC) contribution at a CI. In this work, we will explore the form of the exact v_{KS} to get more information

about the effects of correlation on electronic structure near CIs and obtain reference KS potentials for comparison of functional performance at CIs.

The Kohn-Sham (KS) formalism of DFT is widely used in electronic structure theory and reaction path discovery due to the low dimensionality of the KS equations.[49,51] A key part of the reduction in complexity is that, as opposed to wavefunction theory where interactions between electrons are taken into account explicitly, these interactions are instead treated with an effective potential

$$\left[-\frac{1}{2}\nabla^2 + v_{KS}(r)\right]\phi_i = \varepsilon_i\phi_i \tag{4.1}$$

With the KS potential being defined as

$$v_{KS}(r) = v_{ext}(r) + v_H(r) + v_{xc}(r) \tag{4.2}$$

Where the ∇^2 term is the Laplacian, v_{ext} is the external potential, v_H is the Hartree potential, and v_{xc} is the exchange-correlation potential. The non-interacting kinetic energy, external potential, and Hartree potential are known exactly and represent classical interactions, whereas the XC potential includes quantum effects. If the XC potential is known exactly, the KS solution will also be exact.[49,241,242] The exact form that the XC potential takes is unknown, but it is defined as the functional derivative of the XC energy.

$$v_{xc}(r) = \frac{\delta E_{xc}[\rho(r)]}{\delta\rho(r)} \tag{4.3}$$

It is thus of great interest to study how approximations to the XC potential can be improved. One approach to this problem is through inverse DFT methods, where densities from wavefunction theory are used to produce the XC potential. A sufficiently accurate wavefunction theory density can be inverted to produce a near-exact XC potential.

Recent approaches to the inverse DFT problem are able to obtain exact XC potentials in a complete basis.[69] For general application in atom-centered basis sets, the Ryabinkin-Kohut-Staroverov (RKS) method is able to obtain accurate XC potentials in a Gaussian basis.[70] Further work has been done to improve the robustness of finite basis inversion methods. The most recent of these advances[1] expanded upon previous works[59–61,70–72,243,244] to improve the description of XC potentials in Slater and Gaussian basis sets. The method used in this work utilizes the optimization procedure from Rask et al.[72] to find the KS orbitals, which are then applied to the orbital averaging strategy adapted through refs. 59–61 to obtain their associated eigenvalues. The KS eigenstates are then used to obtain the v_{xc} through an energy balance equation. Other inversion procedures which

solve the KS equations directly would struggle here as they would attempt to iteratively find a single Slater determinant solution to a problem requiring the description of multiple determinants. In principle, though a single KS determinant solution exists and can yield the correct density, which approximations fail to produce.[245,246] The procedure used in this work results in highly accurate XC potentials within a finite Slater basis set and has the ability to resolve KS potentials for degenerate states.

In this chapter, we will show the first glimpse of a KS potential at a CI and how it changes with different linear combinations of both adiabatic wavefunctions. This information allows for previously unavailable insight into the bonding character of systems, which will be analyzed using the classical turning surface (CTS), KS orbitals, and KS potential for the H_3 and NH_3 systems.

4.2 Methods

4.2.1 Inversion Procedure

The inversion procedure used in this work builds off work by Khanna et al.[1] and solves for v_{xc} via an energy balance equation that equates KS and WF quantities. This procedure starts by using the density fitting expression developed by Rask et al.[72]

$$\Phi_{KS} = argmin\left(\int |\rho_{WF}(r) - \rho_{KS}(r)|^n dr + \lambda\langle\Phi_{KS}|\hat{T}|\Phi_{KS}\rangle\right) \tag{4.4}$$

Where ρ_{WF} and ρ_{KS} are the wavefunction and KS densities with exponent n, which can be used to modify the optimization surface. The density fitting is paired with minimization of the kinetic energy since this procedure is not directly solving the KS equations. The λ parameter is used to balance the kinetic energy and density fitting components, where a large λ more heavily weighs kinetic energy minimization. In practice, λ is small since the density is near-exact when a sufficient amount of correlation is recovered. KS eigenvalues are then obtained via the method defined in Khanna et al.[1], which builds upon the orbital averaging expressions developed by Baerends et al.[59,60] and used in an inversion method.[61] After obtaining the eigenvalues, one can directly solve for v_{xc} by using the energy balance equation

$$v_{xc}(r) = v_{KS}^{WF}(r) + \bar{\varepsilon}^{KS}(r) - \bar{\varepsilon}^{WF}(r) + \frac{\tau^{WF}(r)}{\rho^{WF}(r)} - \frac{\tau^{KS}(r)}{\rho^{KS}(r)} \tag{4.5}$$

Where $\bar{\varepsilon}$ are the averaged orbital eigenvalues and $\frac{\tau}{\rho}$ is the kinetic energy density. To emphasize the point, this procedure can obtain v_{xc}, and therefore the KS potential, for strongly

correlated/degenerate systems so long as the wavefunction theory is capable of handling the correlation. This is because the densities for both states can be obtained via configuration interaction and separately fit using the density fitting expression (Equation 4.5). Since both sets of KS orbitals are obtained separately and every subsequent step in the procedure is non-iterative, the root flipping problem is avoided.

4.2.2 Theta

One can represent the geometry of a system around a CI as a linear combination of the NAC and DG vectors which compose a CI. This can be described by some rotation θ between vectors, where if one takes any circle enclosing a CI, one can describe the mixing of the vectors composing the branching plane by

$$f(R,\theta) = g(R)\sin\theta + h(R)\cos\theta \tag{4.6}$$

Figure 4.1 illustrates the Branching plane vectors for H_3 and shows energies for different fixed radii R around a CI for H_3. If g and h reach 0 (at a CI), the wavefunction can be represented as any linear combination of states composing a CI.

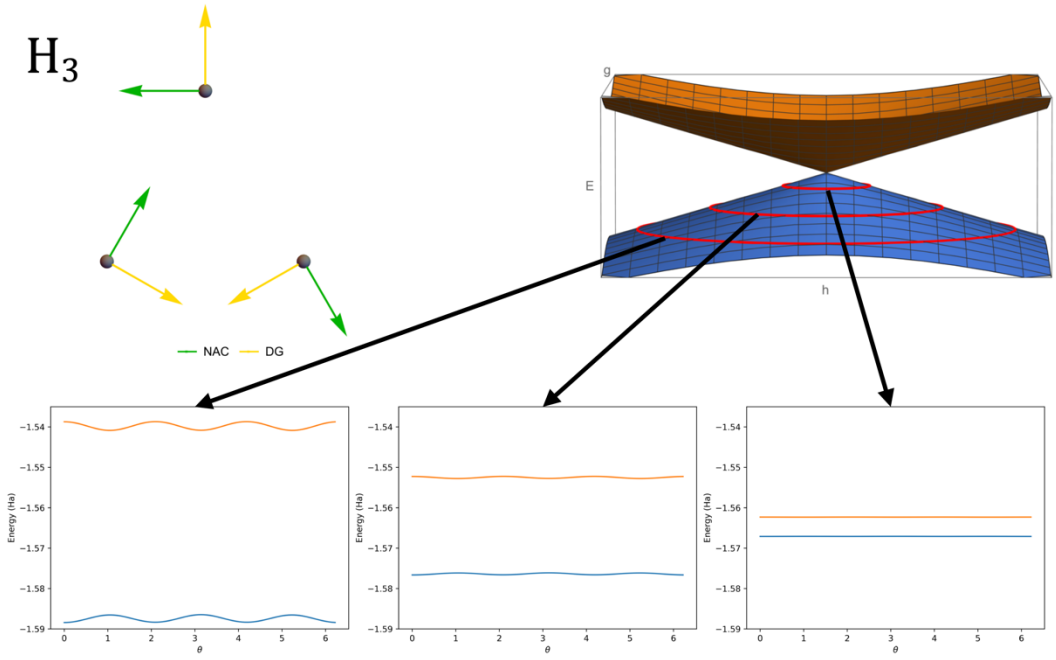

Figure 4.1: Unit vectors with the directionality of the non-adiabatic coupling and difference gradient vectors for H_3 (top-left). Conical intersection constructed using standard model equation with three circles indicating geometries around the CI (top). Plots showing energies for H_3 geometries around a CI obtained by using equation 4.6 and setting a desired radius for the circle, here the radii are 0.1, 0.05, and 0.01Å (top-right and bottom).

This is achieved by obtaining two wavefunctions for both states involved in a CI, which allows us to make a new wavefunction composed of some linear combination of both states varying by θ.

$$|\Psi_\theta\rangle = \sin\theta\,|\Psi_0\rangle + \cos\theta\,|\Psi_1\rangle \tag{4.7}$$

Where 0 and 1 indicate both states present at a CI. A density for any value of θ can then be constructed, and the inversion procedure outlined above can be used for any θ state. It is important to note that the density (and thus the KS potential) is unlike the wavefunction and does not accumulate geometric phase. Since a 2π rotation about a CI has the result of multiplying the wavefunction by -1, it is trivially seen that the same will not be true for density, which is proportional to $|\phi|^2$. For the rest of this chapter, the linear combination in equation 4.7 which varies the KS potential with θ will be referred to as theta and can be thought of as rotating the electronic description at a CI, similar to the rotation around the red circles in Figure 4.1.

4.2.3 Methodology

Bonding character information at a conical intersection can be especially useful to compare the differences in the KS potential away from, and at a CI. To analyze the bonding, the classical KS turning surface[247,248] will be utilized, which is defined as the surface where

$$v_{KS} = \varepsilon_{HOMO} \tag{4.8}$$

The classical turning surface (CTS) is named as such since a classically acting electron in the system will not have sufficient energy to escape this surface and will be pulled back. The classical turning surface has been shown to be a robust description for the bonding character between 2 atoms. The analysis of bonding character in previous works[247–249] has been conducted using

$$\beta = \frac{d_{AB}}{R_A + R_B} \tag{4.9}$$

Where d_{AB} is the internuclear distance between atoms A and B, and $R_{A,B}$ are the radii of the classical turning surface for A and B individually. This β value is unable to describe bonding at a conical intersection, as it will remain constant with varying θ. A qualitative description, which was also given in refs. 247–249, will be used in this work to analyze the changes in bonding with θ.

To facilitate analysis of the CTS for H_3 and NH_3, the H_2 system is used to show features of the CTS for a covalently bound equilibrium geometry and for a dissociating geometry. At equilibrium, the CTS is some relatively smooth spheroid; when the system starts to dissociate a

neck (where the volume of the classically allowed region (CAR) between nuclei decreases) starts to form between both nuclei, giving both nuclei a more spherical and individual character than when covalently bound. Examples of this and other processes and types of bonds can be explored in ref. 247, but for the purposes of this work, the covalent and dissociative models are sufficient.

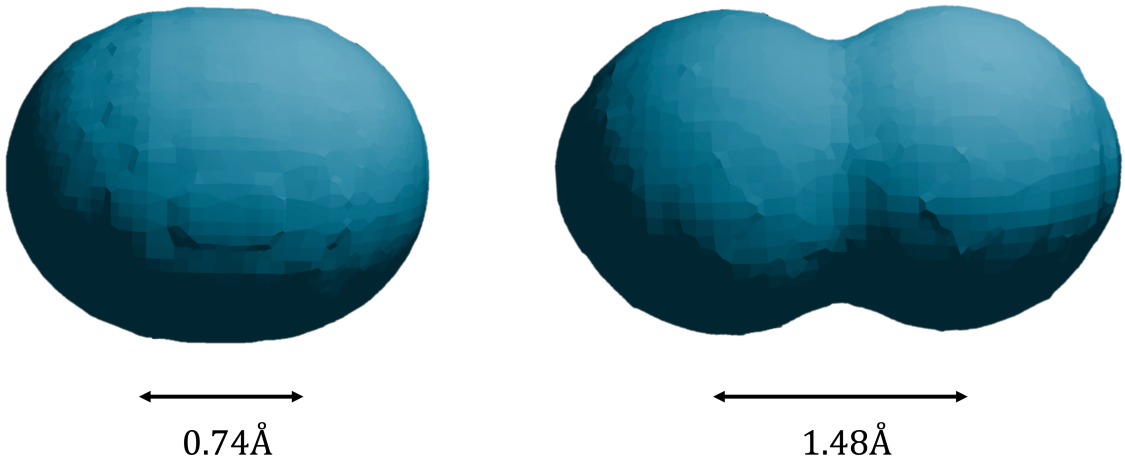

Figure 4.2: The classical turning surface of the H_2 system as equilibrium bond distance (0.74Å) and 2 times equilibrium bond distance (1.48Å).

4.2.4 Computational Details

In this work, the H_3 and NH_3 systems will be analyzed in a custom 5Z Slater basis which is specified in Table C.1. The Prolate Spheroidal method discussed in Chapter 2 is used to compute integral quantities, and the HBCI method is used to obtain an accurate wavefunction and energies for the neutral and ionized systems. The HBCI method works by starting with a reference wavefunction and incrementally adding singly and doubly excited configurations. Configurations are added to the wavefunction if they exceed an energy threshold ε_{var} set by the user; in this work, $\varepsilon_{var} = 1 \times 10^{-5}$ Ha for H_3 and $\varepsilon_{var} = 1 \times 10^{-4}$ Ha for NH_3. Details about the HBCI procedure can be found in refs. 42,44,45. For the density fitting step, λ is 0.00003 for H_3 and 0.00002 for NH_3. 11 values of θ from 0 to $\frac{\pi}{2}$ were used; for compactness only 4 values will be shown in the main text; the full scan will be available in Figures C.1-C.8.

4.3 Results and Discussion

4.3.1 H_3

The H_3 system was chosen since it is the simplest molecule which has a conical intersection and as such is well studied.[250–254] The geometry analyzed here has an H-H bond length of 1.20Å

and has CIs due to the D_{3h} symmetry of the system. The dynamics of the H_3 system have been studied where a dissociation process occurs through a CI resulting in $H+H_2$.[253,254] Since the KS potential changes with theta at a CI, different potentials are important based upon the angle of approach to a CI. The work presented here does not discuss any findings related to the dynamics of the systems analyzed; rather, the existing literature about the dynamics of H_3 and NH_3 is used to justify observations made at a CI. The KS potential with varying θ is shown, where a valley can be observed along the red lines in Figure 4.3. This observation is directly related to the KS orbitals (KSO) of the system, where the KS potential has valleys overlapping with the nodes in the singly occupied KSOs (SOKSO) (Figure 4.4). These valleys rotate with θ and make a full 90º rotation between the node in the $\theta = \frac{10\pi}{20}$ and $\theta = \frac{0\pi}{20}$ SOKSO.

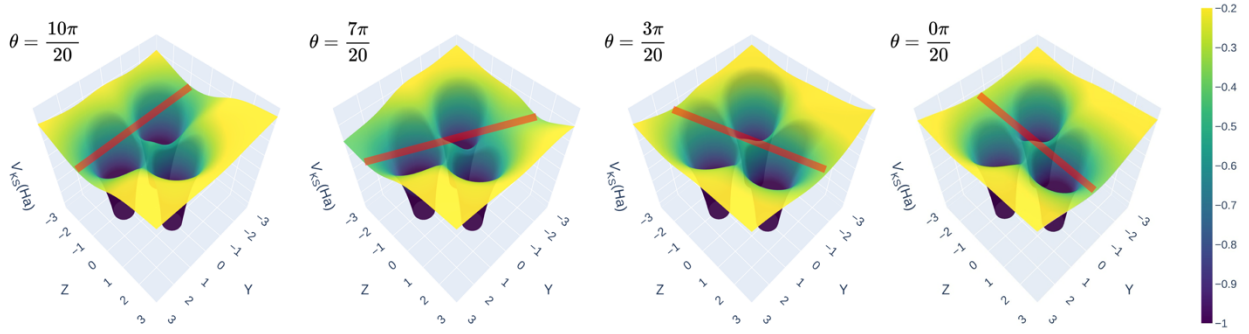

Figure 4.3: The Kohn-Sham potential for H_3 at $\theta = \frac{10\pi}{20}, \frac{7\pi}{20}, \frac{3\pi}{20}, \frac{0\pi}{20}$ along the YZ plane in which the geometry also exists. The coorinates are in a.u. and the H_3 geometry can be found in the SI (Table C.2).

A decrease in the KS potential at a node is expected, as the kinetic energy density for the SOKSO will tend towards infinity at regions of low density, such as a node. The density, however, is constructed as a sum of all orbital contributions, so it is minimized at nodes which have significant amplitude contributions from other KSOs. In the H_3 system, only two KSOs and 3 electrons are contributing to the KS potential, so the minimization of the KS potential is more pronounced in contrast to a system with more core orbitals. It is important to also note that this KS potential is constructed from points purely on the YZ plane of the grid, which also happens to be the plane on which the geometry lies. Since the node is perpendicular to the geometric plane the analysis is fairly straightforward, and changes with θ can easily be observed.

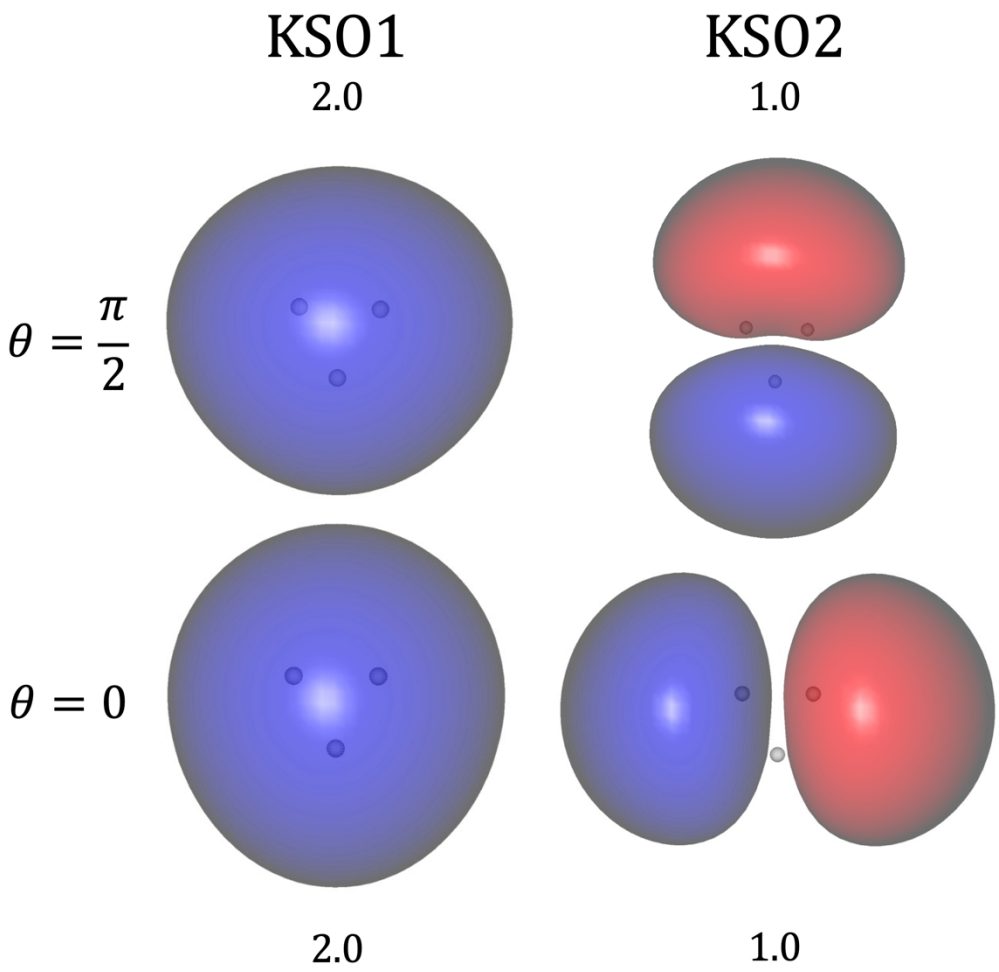

Figure 4.4: The first 2 Kohn-Sham orbitals obtained from the inversion procedure for the $\theta = 0$ and $\theta = \frac{\pi}{2}$ states of H_3. Isovalue of 0.05 was used and occupation numbers are given.

The H_3 system contains both covalent and dissociative character depending on θ, where at $\theta = \frac{10\pi}{20}$ in Figure 4.5 the CTS for all three of the hydrogens has distinct spheres, and the turning surface volume is mostly concentrated around two of the nuclei. When $\theta = \frac{0\pi}{20}$, a covalent type of bond is observed between two of the hydrogens, while the third hydrogen has dissociative character. $\theta = \frac{3\pi}{20}$ and $\theta = \frac{7\pi}{20}$ look to be analogs to the $\frac{10\pi}{20}$ and $\frac{0\pi}{20}$ cases, although this cannot be definitively shown due to the CTS becoming unstable at the node at moderate distances from the centers.

The surface is seen to be unstable along nodes due to the pronounced decrease in KS potential for H_3 along a node. This is believed to occur due to the energy balance terms which, for kinetic energy density will have zero contribution from the SOKSO at the node, meaning only

KSO1 is contributing to the density. When the density from KSO1 drops below a certain threshold, the kinetic energy density terms will become large, increasing in error, and tending towards positive or negative infinity. This is the reason why, in the case of $\theta = \frac{3\pi}{20}$, the CTS is closed, but at other θ values the node causes the surface to open. In the H_3 system, the density decreases faster than the KS potential surpasses the HOMO orbital energy, resulting in the open surfaces seen in the CTS. To visualize the movement of the node, the SOKSO orbital in the H_3 system is plotted with varying theta and can be found in the SI (Figure C.3). Figure C.3 also offers more evidence to the claim that $\theta = \frac{3\pi}{20}$ and $\theta = \frac{7\pi}{20}$ are analogs to $\frac{10\pi}{20}$ and $\frac{0\pi}{20}$, respectively, as each theta has an associated node which look to be similar for the analogs.

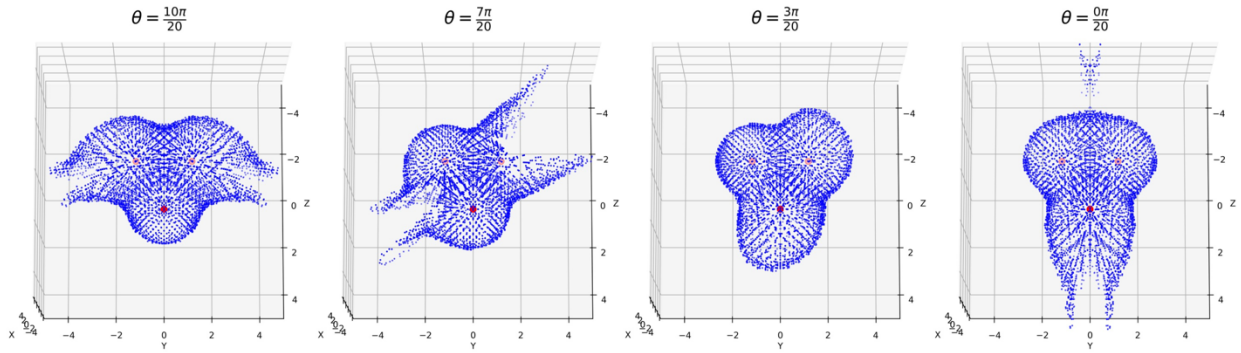

Figure 4.5: Classical turning surface for H_3, points which do not exceed a tolerance of 0.015 Ha of the ionization potential (-0.275 Ha) and points which have density greater than 1×10^{-4} are included. The coordinates are in a.u.

Since at a CI the states are not uniquely defined and any linear combination of said states is an eigenstate, the electron density can move with θ to locations where previously there was a node. $\theta = \frac{10\pi}{20}$ shows a state with dissociative character between all three hydrogens, while $\theta = 0$ resembles a covalent bond between two hydrogens and the dissociation of the third. The CTS produced gives evidence that for H_3 at a CI, KS potentials which are indicative of dissociative bonding exist at certain θ.

4.3.2 NH_3

The NH_3 geometry, which dissociates through a CI and has C_{2v} symmetry, was chosen here and has been studied previously experimentally and theoretically.[255–259] This geometry is particularly interesting as the 6 internal modes are composed of 5 in-plane modes and 1 out-of-plane mode; the branching plane is composed of 1 in-plane and 1 out-of-plane mode. This will be emphasized in the CTS analysis but can be seen in the KS potential surface as well; from $\frac{10\pi}{20}$ to $\frac{0\pi}{20}$

the KS potential surface is decreasing around the NH_2 substituent and increasing perpendicular to the dissociating N-H bond (Figure 4.6). In contrast to the H_3 dissociation, the regions of potential which increase and decrease are not perpendicular to the plane. Where you see smooth rotation of the valley in H_3, in NH_3 two distinct regions are increasing and decreasing (the N-H dissociating bond and the NH_2 substituent, respectively).

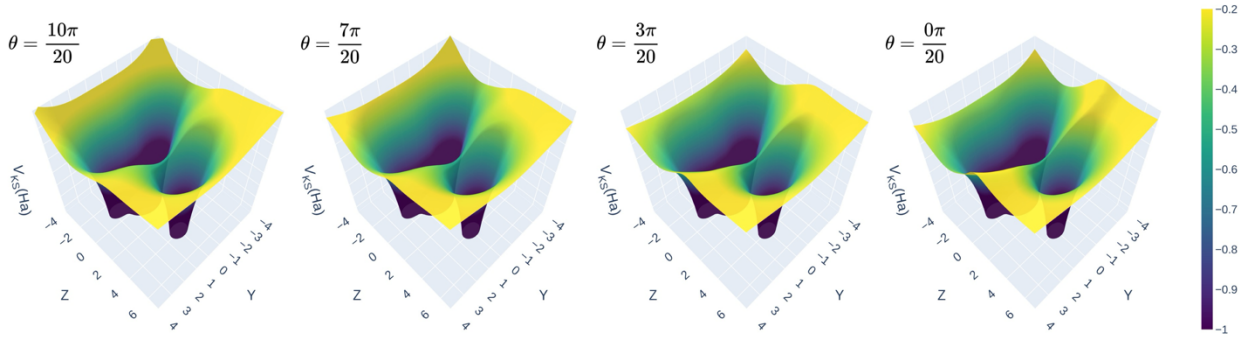

Figure 4.6: The Kohn-Sham potential for NH_3 at $\theta = \frac{10\pi}{20}, \frac{7\pi}{20}, \frac{3\pi}{20}, \frac{0\pi}{20}$ along the YZ plane in which the geometry also exists. The coordinates are in a.u. and the NH_3 geometry can be found in the SI (Table C.2).

The NOs of the NH_3 system emphasize the highly multireference nature of this CI as one of the states at the CI (Ψ_1) has natural orbital occupation numbers (NOON) of 1.716 and 0.275 for its two highest occupied orbitals as opposed to the other state (Ψ_0) with NOONs around 1 for the highest occupied orbitals (Figure C.10). KSO1-KSO3 for both $\theta = \frac{0\pi}{20}$ and $\theta = \frac{10\pi}{20}$ are qualitatively similar (Figure 4.7), however, special attention must be brought to KSO4 where for $\theta = \frac{0\pi}{20}$ the orbital looks to be σ bonding between the dissociating hydrogen and NH_2, and for $\theta = \frac{10\pi}{20}$ the σ bond is becoming weaker as the nitrogen p orbital rotates away from the dissociating hydrogen. The KSO5 and KSO6 orbitals look to be bonding/nonbonding and antibonding, respectively. The KSO5 of $\theta = 0$ is nonbonding and localized on the NH_2, while at $\theta = \frac{10\pi}{20}$ the dissociating hydrogen and NH_2 become bound. KSO6 at both $\theta = 0$ and $\theta = \frac{10\pi}{20}$ is antibonding, although at $\theta = 0$ it seems that more of the amplitude of the orbital lies on the dissociating hydrogen, and less on the NH_2 substituent than in $\theta = \frac{10\pi}{20}$.

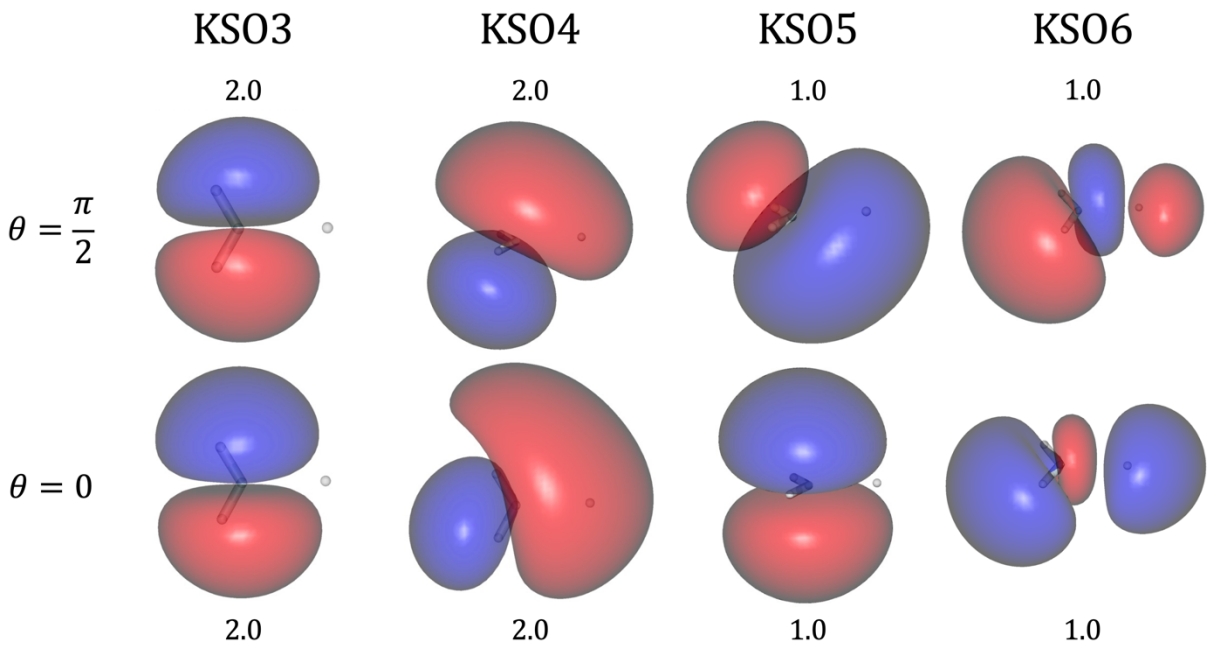

Figure 4.7: Kohn-Sham orbitals 3-6 obtained from the inversion procedure for the $\theta = 0$ and $\theta = \frac{\pi}{2}$ states of NH_3. The coordinates are in a.u., an isovalue of 0.05 was used and occupation numbers are given.

It is immediately obvious from Figure 4.8 that the CTS of the NH_3 system does not suffer from the same nodal defects which are present on the H_3 surface. This is consistent with the earlier hypothesis that, as more core orbitals are contributing to the density, the KS potential surpasses the HOMO orbital energy faster than the density becomes error prone. The CTS gives a clear visualization of the out-of-plane region from $\theta = \frac{10\pi}{20}$ to $\theta = \frac{0\pi}{20}$, in which a reduction in the length of the surface along the x-axis by ~2 Bohr is observed. The dissociating hydrogen in the N-H bond also has a more pronounced spherical character as θ evolves towards $\frac{0\pi}{20}$.

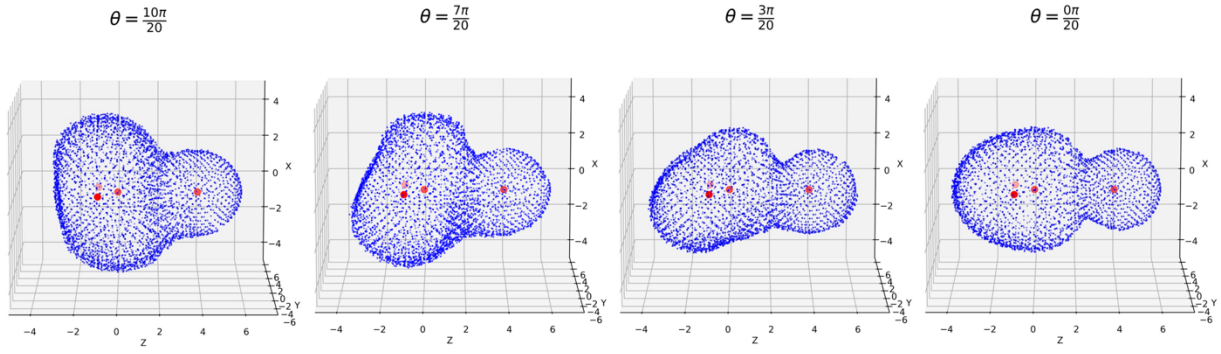

Figure 4.8: Classical turning surface for NH_3, points which do not exceed a tolerance of 0.015 Ha of the ionization potential (-0.328 Ha) and points which have density greater than 1×10^{-5} are included. The coordinates are in a.u.

Comparing these CTSs to the KSOs it appears that most of the out-of-plane orbital contribution at $\theta = \frac{10\pi}{20}$ is due to greater amplitude on the nitrogen from KSO6 and the p orbitals which are rotated out of the bonding axis on nitrogen in KSO4 and KSO5. The only out-of-plane orbital contribution associated with $\theta = 0$ is the KSO5 nonbonding orbital. The CTS of the dissociating hydrogen has weaker bonding character at $\theta = 0$ since both KSO4 and KSO5 are bound at $\theta = \frac{10\pi}{20}$, while KSO5 is nonbonding at $\theta = 0$. This is not a trivial conclusion though, as KSO6 is also less antibonding at $\theta = 0$ compared to at $\theta = \frac{10\pi}{20}$. The CTS is able to inform us then that the relatively stronger bonding of KSO4 and KSO5 at $\theta = \frac{10\pi}{20}$ contribute more to the bonding than the antibonding disrupts, at least compared to $\theta = \frac{0\pi}{20}$. Similar to H_3, the electronic structure of NH_3 provides evidence of the KS potential at a CI having dissociative bonding at certain θ similar to the KS potential of dissociating systems which are not at a CI.

4.4 Conclusion

This work provides the first look into accurate Kohn-Sham potentials at conical intersections. The H_3 and NH_3 systems, which dissociate through a conical intersection, are analyzed; the KS potential, KS orbitals, and classical turning surfaces are utilized for analysis. It was determined that there are KS potentials at certain theta values at a CI which look to be dissociative; these resemble KS potentials for dissociating systems away from a CI. The current metrics that exist to characterize bonding using CTSs are insufficient to quantitatively analyze the bonding characteristics of these KS potentials.[247] Fluctuation of the KS potential is observed to occur both in and out-of-plane depending on the system, making the KS orbitals and CTS useful tools to fully describe the electronic structure at a CI. The openings in the CTS of the H_3 system due to nodes warrants further investigation into the inversion procedure; it is predicted that this will only be a problem for small systems.

Many improvements can be made in this area, notably a new scheme is currently in the works to quantitatively describe the bonding nature of the CTS using topographical data analysis. The inversion method used in this work is limited by the size of the system, as the HBCI method scales exponentially; a basis of at least quadruple zeta quality is suggested to obtain accurate KS potentials. It could be interesting to analyze non-dissociative processes which occur at CIs, such as in PSB3, which truncates the retinal chromophore of rhodopsins and is a well-studied CI which

induces isomerization rather than dissociation.[260–262] This and future inversion studies will be useful in gaining more information towards developing an accurate density functional which can account for exotic states.

Chapter 5
Final Remarks

5.1 Conclusion

This work has outlined to the reader the complexities of electronic structure theory, in which approximation is weighed against accuracy to gain greater insight into the description of chemical systems. This thesis addressed the development and application of cutting-edge methods which will facilitate future theoretical development and description of the chemical world.

Chapter 2 discussed the development of a novel integration scheme which can accurately integrate Slater functions over a prolate spheroidal (PS) grid with a third center incorporated. Building off the GPU-accelerated integral evaluation library SlaterGPU, which has the ability to use Becke partitioning for Slater integral analysis. We reduce the RMSE of 2-center integral evaluation by ~3 orders of magnitude relative to Becke partitioning. The Becke Partitioning accuracy caused SCF convergence issues due to the RMSE being around the same order of magnitude as the smallest overlap matrix eigenvalue in large basis sets. The increase in 2-center integration accuracy allowed for the use of larger basis sets, as the smallest eigenvalues had greater resolution. Through the use of the RI approximation, only 3 centers are necessary, which allows this procedure to be general for polyatomics. To demonstrate the generality, SCF and FCI methods are applied to the propanediyl system using integrals generated via the prolate spheroidal method.

Chapter 3 detailed a composite method which uses the HBCI algorithm to compute the BDE for the ScH system. The method considers semi-core correlation, scalar relativistic effects, and is extrapolated to the CBS limit. Relativistic and semi-core contributions were tested when incorporated directly with the basis set extrapolation calculations. Both relativistic and semi-core considerations, when incorporated directly, disturbed the basis set extrapolation fit, which motivated the semi-core and relativistic effects to be added as a correction instead. For the ScH system, transition metal (TM) thermochemical accuracy (within 3 kcal/mol of experiment) was achieved. Comparison to a modified composite HBCI method which includes semi-core correlation directly (semi-core) rather than adding a correction for the semi-core correlation

(valence), showed that all corrections (CBS, relativistic, and semi-core) differed between the valence and semi-core implementations by ~0.1-0.5 kcal/mol.

Chapter 4 explored the form a KS potential takes at a conical intersection using an inversion procedure based on work by Khanna et al.[1] The H_3 and NH_3 systems were studied, which both dissociate through a CI based upon earlier dynamics work.[250–259] This allows for comparison of KS potentials formed at a CI to KS potentials of dissociating systems away from a CI. The KS potential, KS orbitals, and CTS were all used to probe the electronic/bonding characteristics at a CI with varying linear combinations of the two states (theta). The CTS was qualitatively analyzed since no adequate metric has yet been produced to quantitatively describe the bonding at a CI. The KS potential varies with theta for H_3 and NH_3 in two different ways; it fluctuates perpendicular to the geometric plane of H_3 (in-plane) while it fluctuates parallel to the geometric plane of NH_3 (out-of-plane). The KS orbitals give insight into the bonding and antibonding the system experiences with varying theta. For NH_3, the KSOs increase antibonding, decrease bonding, or a mixture of both, as the wavefunction tends towards $\theta = \frac{0\pi}{20}$. It was observed that the CTS of both systems at specific theta values are indicative of dissociative bonding, with similar characteristics to that of a CTS for a dissociating system away from a CI.

5.2 Future Directions

The conclusions outlined above have illustrated the progress that has been contributed to developing and applying precision quantum chemistry. There are many directions to take these projects; this section will address future directions geared towards the goals of the Zimmerman group and otherwise.

The overarching goal of the Zimmerman group is to leverage accurate electronic structure theory methods to probe the physical principles which govern chemistry, as well as to improve these methods, to unlock more interesting problems. A large project being undertaken is the development of an accurate density functional. Much of the work here can be tied to this goal; for example, the prolate spheroidal integration scheme allows for accurate integration over larger Slater basis sets than were previously achievable with SlaterGPU. The PS method allows for the use of a QZ (or greater) basis when obtaining exchange-correlation (XC) potentials through inversion, and larger basis sets result in more accurate densities. The composite HBCI method, while it cannot be directly applied to inversion, has given insight into the methodology which must

be used to calculate these large, highly correlated systems, which will be useful for future inversion studies on TMs. The KS potential at a CI is also directly tied to this goal; the form of the KS potential at a CI gives insight into the bonding at a CI, which has the potential to change our understanding of the description of the XC potential itself.

A problem which may become interesting when applying inversion to TM systems is that, in Chapter 3, it was found that the QZ auxiliary basis produced an error of ~20 mHa. The prolate spheroidal method relies on the RI approximation to evaluate the integral quantities for general polyatomic systems. It would be useful to ascertain whether this issue appears using a Slater basis or with the auxiliary basis generation present in SlaterGPU.

In Chapter 4, the CTS for certain theta values at a CI is consistent with the CTS description of a dissociating system away from a CI, for both H_3 and NH_3. There are other interesting processes where the KS potential should be explored at CIs. An example of this is PSB3, which truncates the retinal chromophore of rhodopsins, where isomerization takes place through a CI.[260–262]

The HBCI composite method can serve as a starting point for many further studies. First are improvements which provide greater accuracy for corrections such as 2-electron X2C methods and alternative extrapolation procedures for CBS and semi-core. The cost of directly incorporating, for example, semi-core correlation is not a problem for ScH, but is not feasible for larger systems. A large calculation which tested the limits of HBCI scaling was performed on an iron complex (22e-,168o) over 32 nodes (4096 cores)[45] by Dang et al. For larger TM diatomics of interest such as semi-core correlated CrO in a cc-pwCVQZ basis (20e-,159o), the composite procedure can become expensive. A more thorough look at the impact of the corrections obtained in the HBCI composite procedure for other, more strongly correlated, systems can be conducted to inform an accurate and reliable correction procedure. Second, an excitation analysis of the HBCI method past tracking what level of excitation is occurring, and towards which orbitals are becoming occupied and unoccupied for different configurations which contribute to the wavefunction is desirable. Also, considering how these distributions change with respect to each variational iteration could be useful for informing an HBCI implementation which more effectively searches the Hilbert space for TMs.

Appendices

Appendix A:
Supporting Information for Chapter 2

A.1 Slater Basis sets

Appendix Table A.1: Slater basis exponents for TZ, QZ, and 5Z basis functions applied to molecules in Figures 2.3, 2.4, 2.5, 2.7 and A.1 and Tables 2.1, 2.2, 2.3, and 2.4.

TZ		QZ		5Z	
H					
1s	2.280	1s	4.000	1s	4.100
1s	1.520	1s	2.500	1s	2.929
1s	1.013	1s	1.5625	1s	2.092
2p	2.100	1s	0.977	1s	1.494
2p	1.500	2p	3.200	1s	1.067
		2p	2.286	2p	4.000
		2p	1.633	2p	2.353
		3d	2.200	2p	1.384
				2p	0.814
				3d	3.400
				3d	1.700
C					
1s	8.689	1s	11.271	1s	15.000
1s	5.323	1s	7.653	1s	10.714
1s	3.261	1s	5.196	1s	7.653
1s	1.998	1s	3.528	1s	5.466
1s	1.224	1s	2.396	1s	3.905
1s	0.750	1s	1.627	1s	2.789
2p	4.000	1s	1.105	1s	1.992
2p	2.051	1s	0.750	1s	1.423
2p	1.052	2p	7.667	1s	1.016

3d	3.400	2p	3.932	2p	11.667
3d	1.900	2p	2.016	2p	6.306
		2p	1.034	2p	3.409
		3d	5.000	2p	1.843
		3d	3.125	2p	0.996
		3d	1.953	3d	5.900
		4f	2.600	3d	4.214
				3d	3.010
				3d	2.150
				4f	3.600
				4f	1.800
N					
1s	10.820	1s	14.453	1s	12.393
1s	6.345	1s	9.471	1s	8.728
1s	3.720	1s	6.206	1s	6.147
1s	2.181	1s	4.067	1s	4.329
1s	1.279	1s	2.665	1s	3.049
1s	0.750	1s	1.747	1s	2.147
2p	4.400	1s	1.145	1s	1.512
2p	2.588	1s	0.750	1s	1.065
2p	1.522	2p	6.533	1s	0.750
3d	4.000	2p	3.960	2p	4.933
3d	2.000	2p	2.400	2p	3.524
		2p	1.454	2p	2.517
		3d	5.500	2p	1.798
		3d	3.235	2p	1.284
		3d	1.903	3d	5.800
		4f	2.200	3d	4.143
				3d	2.959
				3d	2.114
				4f	4.200
				4f	2.100
O					
1s	13.351	1s	18.099	1s	14.948
1s	7.506	1s	11.485	1s	10.283
1s	4.220	1s	7.288	1s	7.075

1s	2.373	1s	4.625	1s	4.867
1s	1.334	1s	2.935	1s	3.348
1s	0.750	1s	1.862	1s	2.303
2p	5.700	1s	1.182	1s	1.585
2p	2.850	1s	0.750	1s	1.090
2p	1.425	2p	7.000	1s	0.750
3d	4.000	2p	4.000	2p	8.667
3d	2.000	2p	2.286	2p	5.417
		2p	1.306	2p	3.385
		3d	6.000	2p	2.116
		3d	3.529	2p	1.322
		3d	2.076	3d	5.600
		4f	2.600	3d	4.000
				3d	2.857
				3d	2.041
				4f	4.400
				4f	2.200
F					
1s	15.520	1s	21.908	1s	17.972
1s	8.466	1s	13.528	1s	12.082
1s	4.619	1s	8.354	1s	8.123
1s	2.520	1s	5.158	1s	5.461
1s	1.375	1s	3.185	1s	3.671
1s	0.750	1s	1.967	1s	2.468
2p	5.667	1s	1.215	1s	1.659
2p	3.063	1s	0.750	1s	1.116
2p	1.656	2p	5.667	1s	0.750
3d	4.000	2p	3.542	2p	7.000
3d	2.000	2p	2.214	2p	4.828
		2p	1.383	2p	3.329
		3d	5.000	2p	2.296
		3d	3.226	2p	1.584
		3d	2.081	3d	6.500
		4f	2.300	3d	4.333
				3d	2.889
				3d	1.926

				4f	5.400
				4f	2.700
Si					
1s	19.317	1s	31.922	1s	31.922
1s	12.870	1s	22.699	1s	22.699
1s	8.575	1s	16.140	1s	16.140
1s	5.713	1s	11.477	1s	11.477
1s	3.806	1s	8.161	1s	8.161
1s	2.536	1s	5.803	1s	5.803
1s	1.690	1s	4.126	1s	4.126
1s	1.126	1s	2.934	1s	2.934
1s	0.750	1s	2.086	1s	2.086
2p	11.333	1s	1.483	1s	1.483
2p	6.869	1s	1.055	1s	1.055
2p	4.163	1s	0.750	1s	0.750
2p	2.523	2p	10.667	2p	13.600
2p	1.529	2p	7.619	2p	9.714
2p	0.927	2p	5.442	2p	6.939
3d	3.400	2p	3.887	2p	4.956
3d	2.000	2p	2.777	2p	3.540
		2p	1.983	2p	2.529
		2p	1.417	2p	1.806
		2p	1.012	2p	1.290
		3d	3.500	2p	0.922
		3d	2.500	2p	0.658
		3d	1.786	3d	5.400
		4f	2.200	3d	3.857
				3d	2.755
				3d	1.968
				4f	4.400
				4f	2.200
S					
1s	23.379	1s	31.547	1s	31.547
1s	15.209	1s	22.456	1s	22.456
1s	9.894	1s	15.985	1s	15.985
1s	6.437	1s	11.380	1s	11.378

1s	4.187	1s	8.099	1s	8.099
1s	2.724	1s	5.765	1s	5.765
1s	1.772	1s	4.104	1s	4.104
1s	1.153	1s	2.921	1s	2.921
1s	0.750	1s	2.079	1s	2.079
2p	12.800	1s	1.480	1s	1.480
2p	8.000	1s	1.054	1s	1.054
2p	5.000	1s	0.750	1s	0.750
2p	3.125	2p	13.067	2p	17.067
2p	1.953	2p	9.333	2p	12.190
2p	1.221	2p	6.667	2p	8.707
3d	3.700	2p	4.762	2p	6.220
3d	2.000	2p	3.401	2p	4.443
		2p	2.430	2p	3.173
		2p	1.735	2p	2.267
		2p	1.240	2p	1.619
		3d	3.500	2p	1.156
		3d	2.500	2p	0.826
		3d	1.786	3d	4.600
		4f	2.300	3d	3.286
				3d	2.347
				3d	1.676
				4f	2.800
				4f	1.400
Cl					
1s	21.825	1s	31.403	1s	31.747
1s	15.156	1s	22.363	1s	22.585
1s	10.525	1s	15.925	1s	16.068
1s	7.309	1s	11.341	1s	11.431
1s	5.076	1s	8.076	1s	8.132
1s	3.525	1s	5.751	1s	5.785
1s	2.448	1s	4.095	1s	4.116
1s	1.700	1s	2.916	1s	2.928
1s	1.180	1s	2.077	1s	2.083
2p	22.000	1s	1.479	1s	1.482
2p	12.571	1s	1.053	1s	1.054

2p	7.184	1s	0.750	1s	0.750
2p	4.105	2p	14.667	2p	18.600
2p	2.346	2p	10.476	2p	13.286
2p	1.340	2p	7.483	2p	9.490
3d	3.7	2p	5.345	2p	6.778
3d	2.0	2p	3.818	2p	4.842
		2p	2.727	2p	3.458
		2p	1.948	2p	2.470
		2p	1.391	2p	1.764
		3d	4.000	2p	1.260
		3d	2.857	2p	0.900
		3d	2.041	3d	5.100
		4f	2.200	3d	3.643
				3d	2.602
				3d	1.859
				4f	2.400
				4f	1.200

A.2 Geometries

Appendix Table A.2: Geometries in Ångstrom for systems used in Figures 2.3, 2.4, 2.5, 2.7 and Tables 2.1, 2.2, and 2.3 as well as the large bond distance OF_2 structure used to obtain Figure A.1. Geometries with 3 or greater atoms were optimized using DFT with a ωB97X functional in a cc-pVQZ basis, unless specified elsewhere. The 1,3 propanediyl system was optimized with the B3LYP functional in a 6-31G* basis.

Molecule	Atom	X	Y	Z
HF				
	H	0.0	0.0	0.0
	F	0.0	0.0	0.9170
C_2				
	C	0.0	0.0	0.0
	C	0.0	0.0	1.147
N_2				
	N	0.0	0.0	0.0
	N	0.0	0.0	1.098
CO				
	C	0.0	0.0	0.0
	O	0.0	0.0	1.128
NO				

	N	0.0	0.0	0.0
	O	0.0	0.0	1.054
O_2				
	O	0.0	0.0	0.0
	O	0.0	0.0	1.208
HCl				
	H	0.0	0.0	0.0
	Cl	0.0	0.0	1.275
CS				
	C	0.0	0.0	0.0
	S	0.0	0.0	1.535
SiO				
	Si	0.0	0.0	0.0
	O	0.0	0.0	1.510
ClF				
	Cl	0.0	0.0	1.628
	F	0.0	0.0	0.0
Cl_2				
	Cl	0.0	0.0	0.0
	Cl	0.0	0.0	1.988
H_2O				
	H	0.03662	0.2867	-0.7420
	H	0.006501	1.1120	0.5315
	O	-0.003118	0.2113	0.2105
HCN				
	H	-0.008949	0.01992	1.092
	C	0.01279	0.05594	0.02497
	N	0.03616	0.09413	-1.117
OFH				
	O	-0.004260	0.02793	0.1246
	F	0.005461	1.316	0.6854
	H	0.03880	0.2657	-0.8100
N_3				
	N	0.01331	0.5362	0.0003591
	N	-0.005540	1.255	0.9236
	N	0.03223	-0.1809	-0.9239

N_2O				
	N	0.03390	-0.1616	-1.002
	N	0.01371	0.3602	-0.01847
	O	-0.007608	0.9114	1.020
NO_2				
	N	-0.008446	-0.02460	0.1907
	O	0.003103	1.029	0.8568
	O	0.04534	0.1060	-1.0475
SFH				
	S	-0.01224	-0.07200	0.2630
	F	0.005247	1.462	0.7820
	H	0.04700	0.2196	-1.045
OF_2				
	O	-0.01081	0.06083	0.3100
	F	0.004032	1.367	0.7531
	F	0.04678	0.1819	-1.063
SO_2				
	S	-0.01091	-0.06565	0.2156
	O	0.001496	1.134	0.9929
	O	0.04941	0.04196	-1.208
CS_2				
	C	0.01333	0.5366	0.00005083
	S	-0.01564	1.410	1.275
	S	0.04231	-0.3368	-1.275
OF_2 (long bond)				
	O	0.0	0.0	0.0
	F	0.0	0.0	1.380
	F	0.0	40.23	-9.810
1,3 Propanediyl				
	C	1.278	0.0	0.2597
	C	0.0	0.0	-0.5852
	C	-1.278	0.0	0.2597
	H	1.325	-0.8846	0.9073
	H	1.325	0.8846	0.9073
	H	0.0	0.8776	-1.246
	H	0.0	-0.8776	-1.246

	H	-1.325	-0.8846	0.9073
	H	-1.325	0.8846	0.9073

A.3 PS Grid Sizes

Appendix Table A.3: Grid sizes used for Figures 2.3 and 2.4 (left) and Figure 2.5 (right). All combinations of radial and angular number of points were considered (left). Each row of values represents parameters for a single calculation in the generation of Figure 2.5 (right).

N_μ	N_ν	N_ϕ
26	20	8
27	22	9
28	24	10
29	26	11
30	28	12
31	30	13
32	32	14
33	34	15
34	36	16
35	38	17
36	40	18
37	42	19
38	44	20

N_μ	N_ν	N_ϕ
13	20	8
14	20	8
15	22	9
16	22	9
17	24	10
18	24	10
19	26	11
20	26	11
21	28	12
22	28	12
23	30	13
24	30	13
25	32	14
26	32	14
27	34	15
28	34	15
29	36	16
30	36	16
31	38	17
32	38	17
33	40	18
34	40	18
35	42	19
36	42	19
37	44	20
38	44	20

A.4 Long Bond Distance N_{SP}

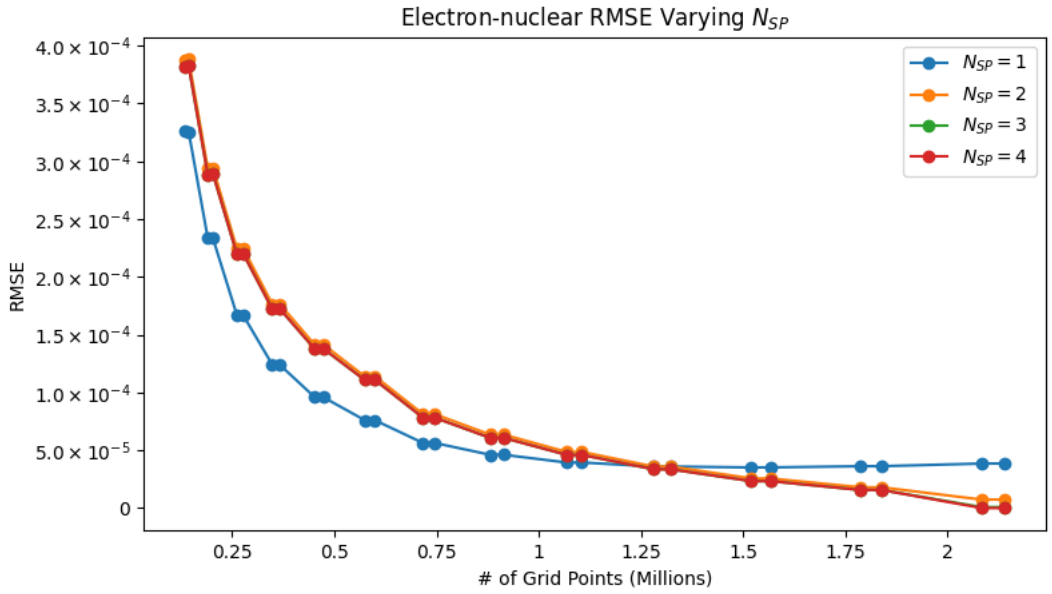

Appendix Figure A.1: Comparison of the RMSE (Ha) of the electron-nuclear attraction elements for different divisions of the third center within the PS integration grid. Calculations performed on the OF_2 system with one OF bond as a 41.41Å distance.

The RMSE of the electron-nuclear attraction integral for OF_2 with an OF bond at ~30 times equilibrium bond length confirms the error is reduced at large grid discretization up to $N_{SP} = 3$. At smaller grid sizes when $N_{SP} > 1$ the RMSE of the electron-nuclear attraction integral increases, this phenomenon is believed to be caused by a cancellation of error when the grid around the third center is coarser.

A.5 Full 2-Center Coulomb Displacement

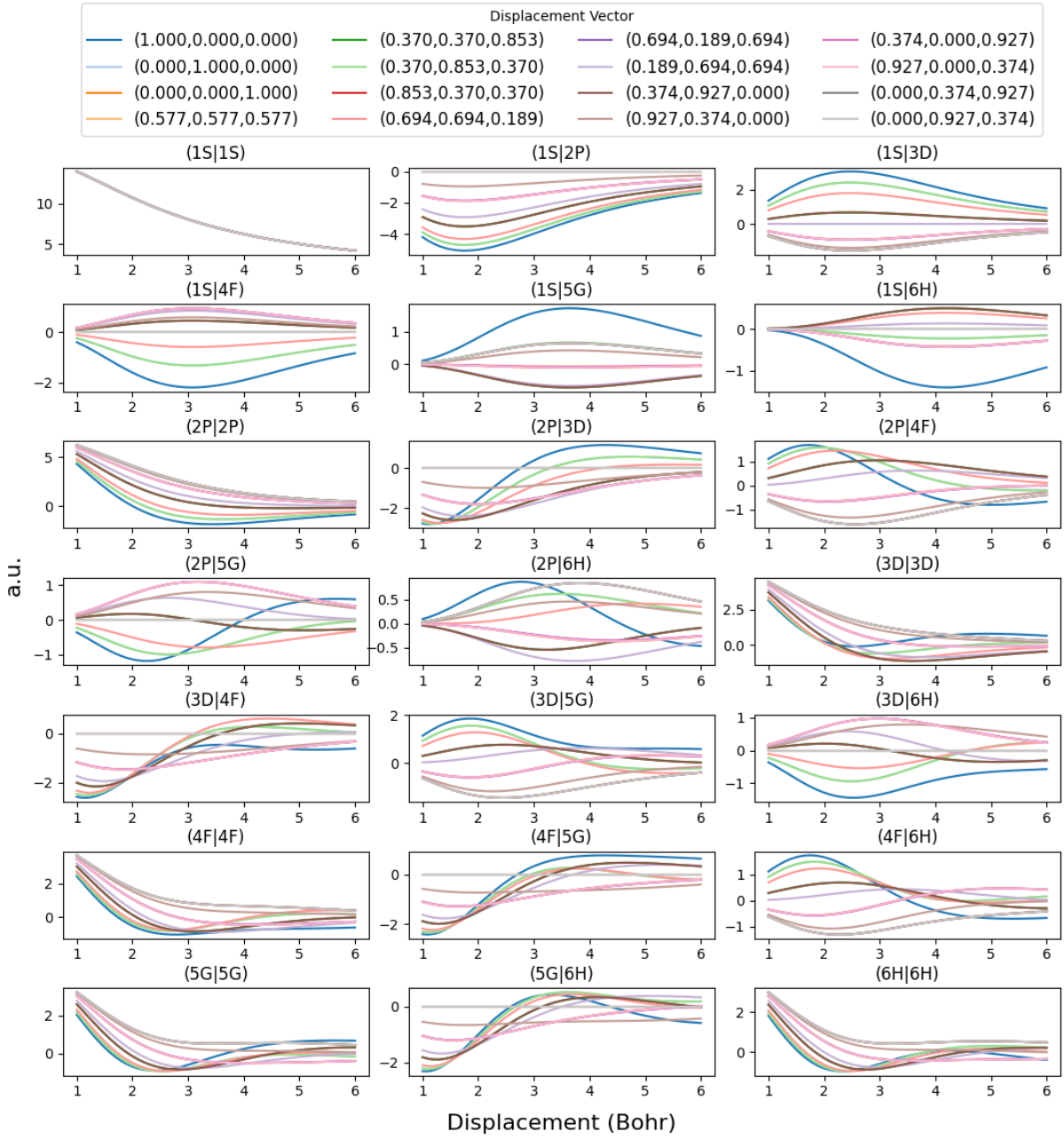

Appendix Figure A.2: All combinations of 2-center Coulomb integrals plotted along 16 vector directions[92] as the two centers are separated. The legend indicates unit vectors for all 16 directions tested, all basis functions used have the exponent $\zeta = 1$, and all basis functions were chosen to have $m = 0$.

A.6 FCI Extrapolation for CH_2 in GTO and STO Basis Sets

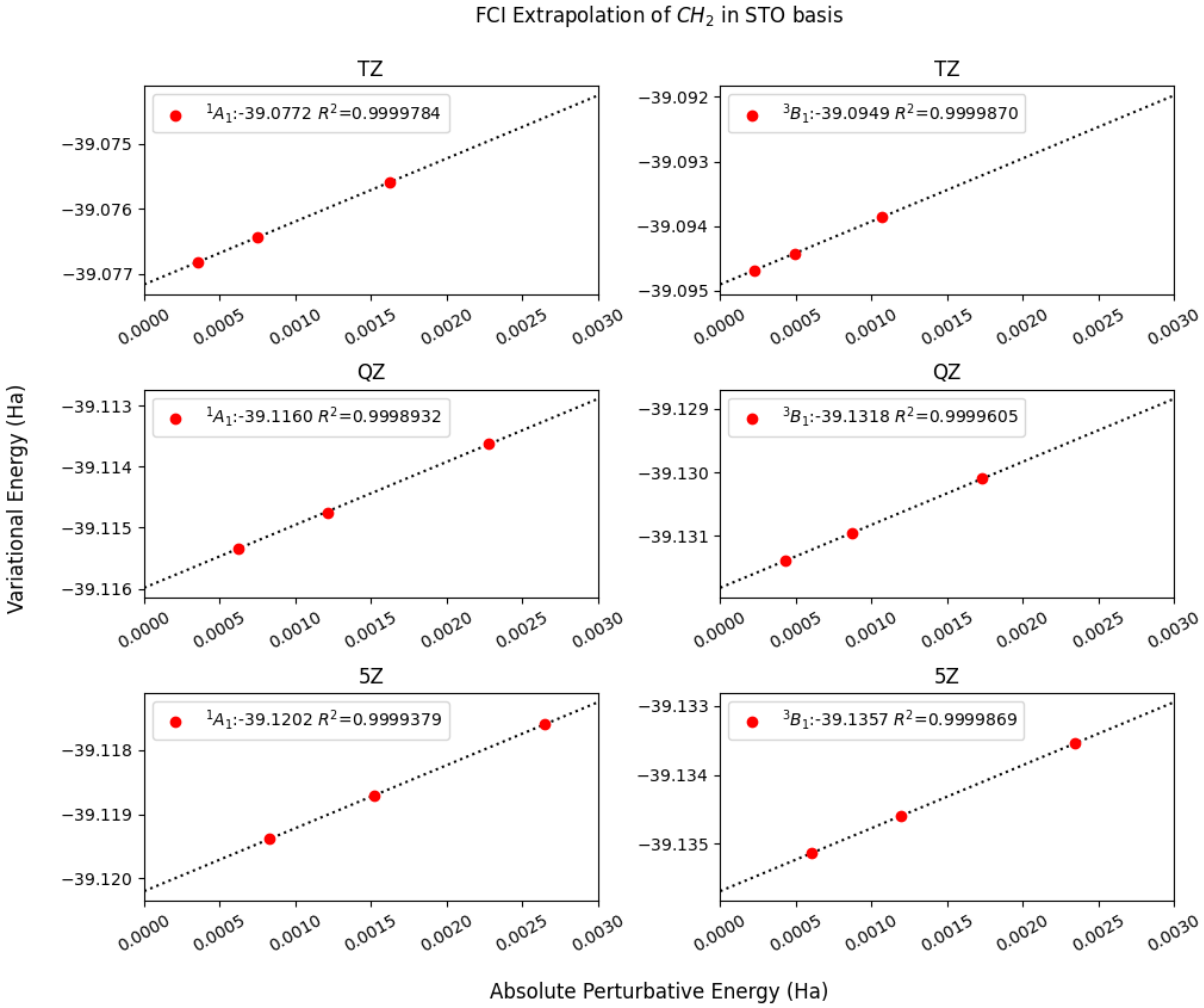

Appendix Figure A.3: FCI Extrapolation energies for methylene in the TZ, QZ, and 5Z basis for both the $^1A_1$ and $^3B_1$ states using STOs.

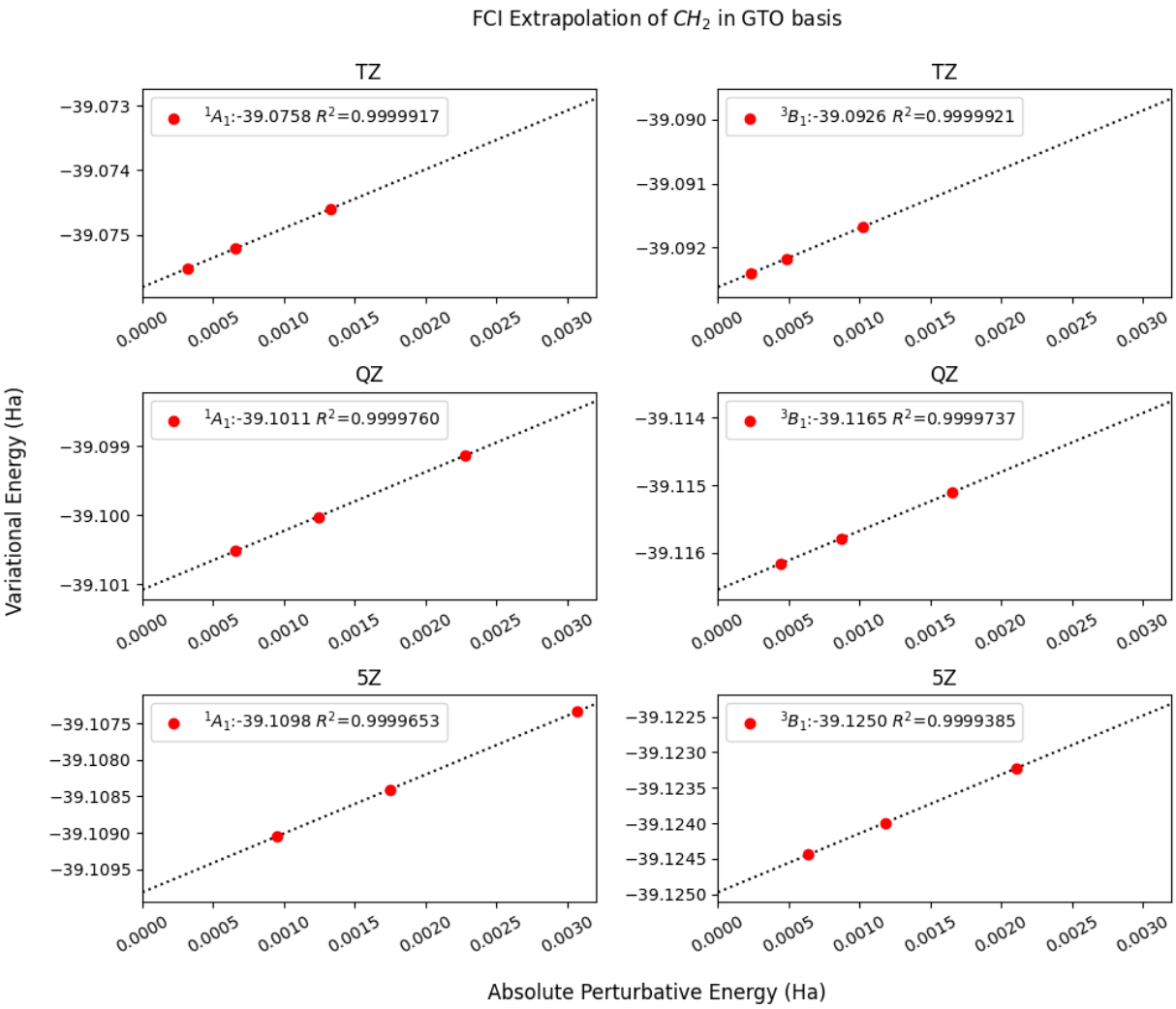

Appendix Figure A.4: FCI Extrapolation energies for methylene in the cc-pVTZ (TZ), cc-pVQZ (QZ), and cc-pV5Z (5Z) basis for both the $^1A_1$ and $^3B_1$ states using GTOs.

To obtain singlet-triplet gap energies for methylene with basis XZ (where X = T, Q, 5) three calculations are performed with varying ε_{var} values ($\varepsilon_{var} = 2 \times 10^{-4}, 1 \times 10^{-4}, 0.5 \times 10^{-4}$ Ha and $\varepsilon_{PT} = 5 \times 10^{-7}$ Ha) for the singlet and the triplet systems. The energies obtained from the extrapolations are then subtracted to find the singlet-triplet gap.

Appendix B:
Supplemental Information for Chapter 3

B.1 FCI Extrapolation cc-pwCVTZ

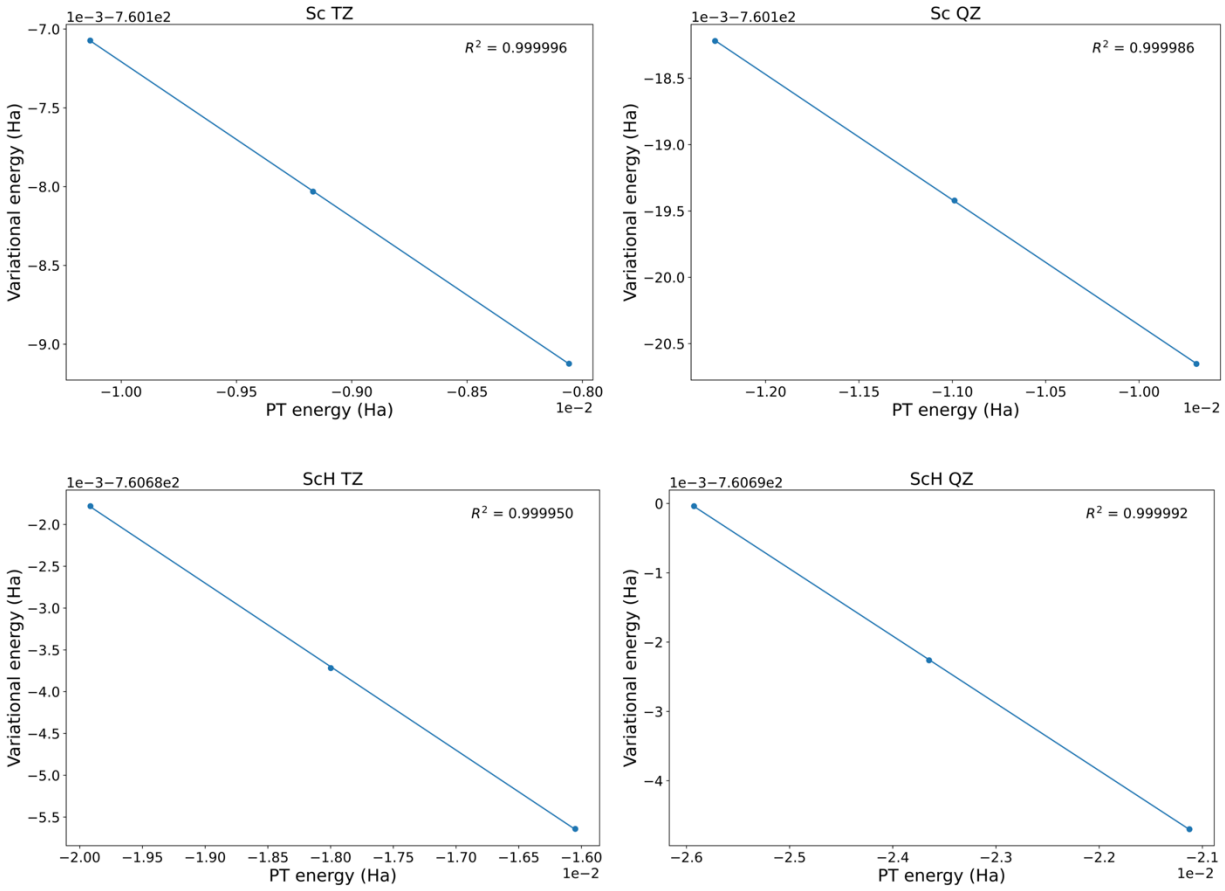

Appendix Figure B.1: FCI Extrapolation for neutral Sc (top) and ScH (bottom) in the cc-pwCVTZ (left) and cc-pwCVQZ (right) basis sets, energies are in Hartree.

B.2 CBS Extrapolation cc-pwCVTZ

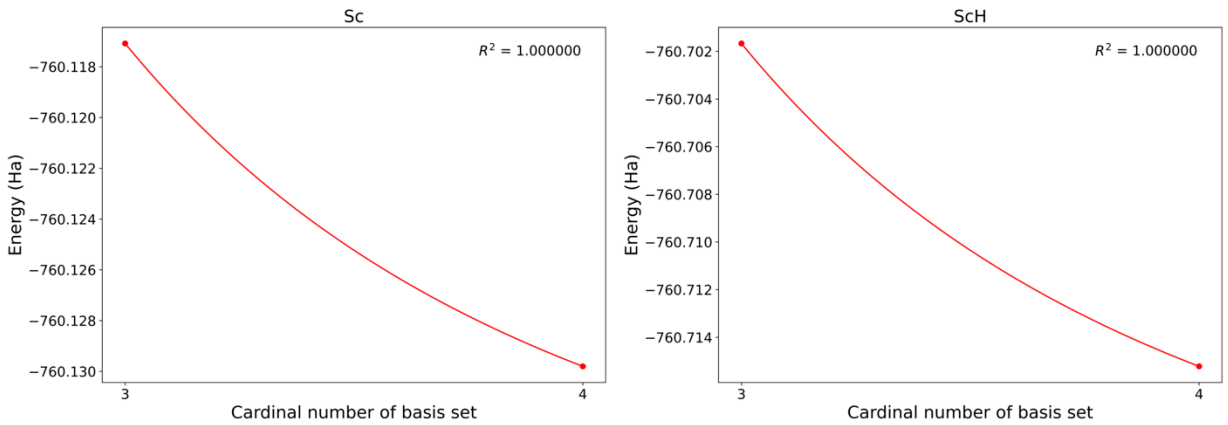

Appendix Figure B.2: CBS Extrapolation for neutral Sc (left) and ScH (right) using the cc-pwCVXZ basis (X=T,Q), energies are in Hartree.

Appendix C:
Supplemental Information for Chapter 4

C.1 Basis Sets

Appendix Table C.1: Slater basis set exponents and associated functions for H_3 and NH_3.

H_3		NH_3	
H		N	
1s	2.74	1s	12.85
1s	1.96	1s	7.65
1s	1.40	1s	5.75
1s	1.00	2s	6.85
1s	0.71	2s	3.20
2p	2.70	2s	2.05
2p	1.80	2s	1.40
2p	1.20	2s	0.70
2p	0.80	2p	6.00
3d	3.20	2p	3.60
3d	2.00	2p	2.40
3d	1.33	2p	1.60
		2p	0.90
		3d	2.50
		3d	1.50
		H	
		1s	3.50
		1s	2.30
		1s	1.50

	1s	1.00
	1s	0.70
	2p	2.30
	2p	1.60
	2p	1.00

C.2 Geometries

Appendix Table C.2: Geometries for the H_3 and NH_3 systems in Å.

Atom	X	Y	Z
H_3			
H	0.520	0.0	0.0
H	-0.520	0.600	0.0
H	-0.520	-0.600	0.0
NH_3			
N	0.0	0.0	0.0
H	-0.512	0.886	0.0
H	-0.512	-0.886	0.0
H	2.06	0.0	0.0

C.3 Full Scan KS Potentials

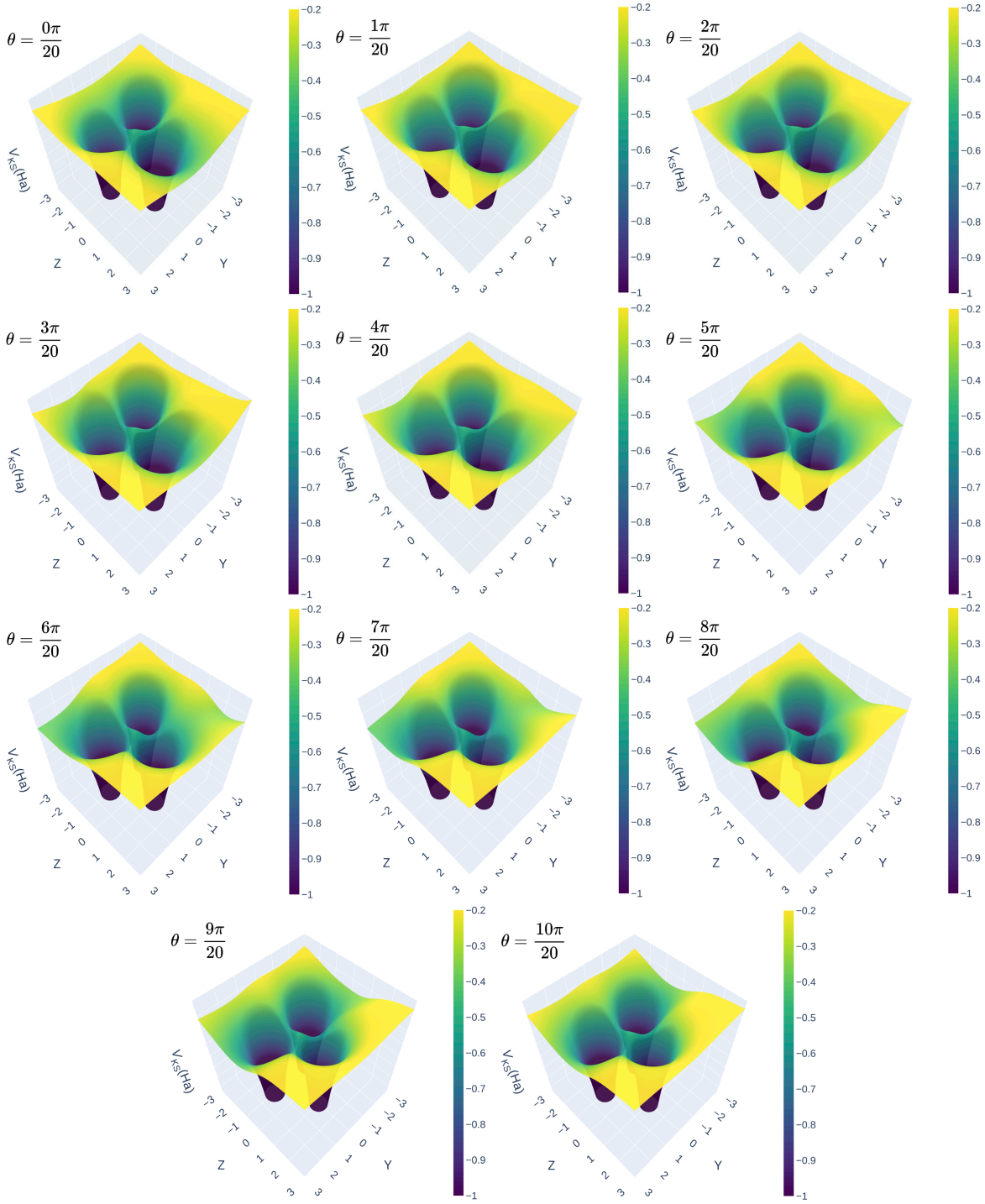

Appendix Figure C.1: The Kohn-Sham potential for H_3 at different theta along the YZ plane in which the geometry also exists. The coorinates are in a.u.

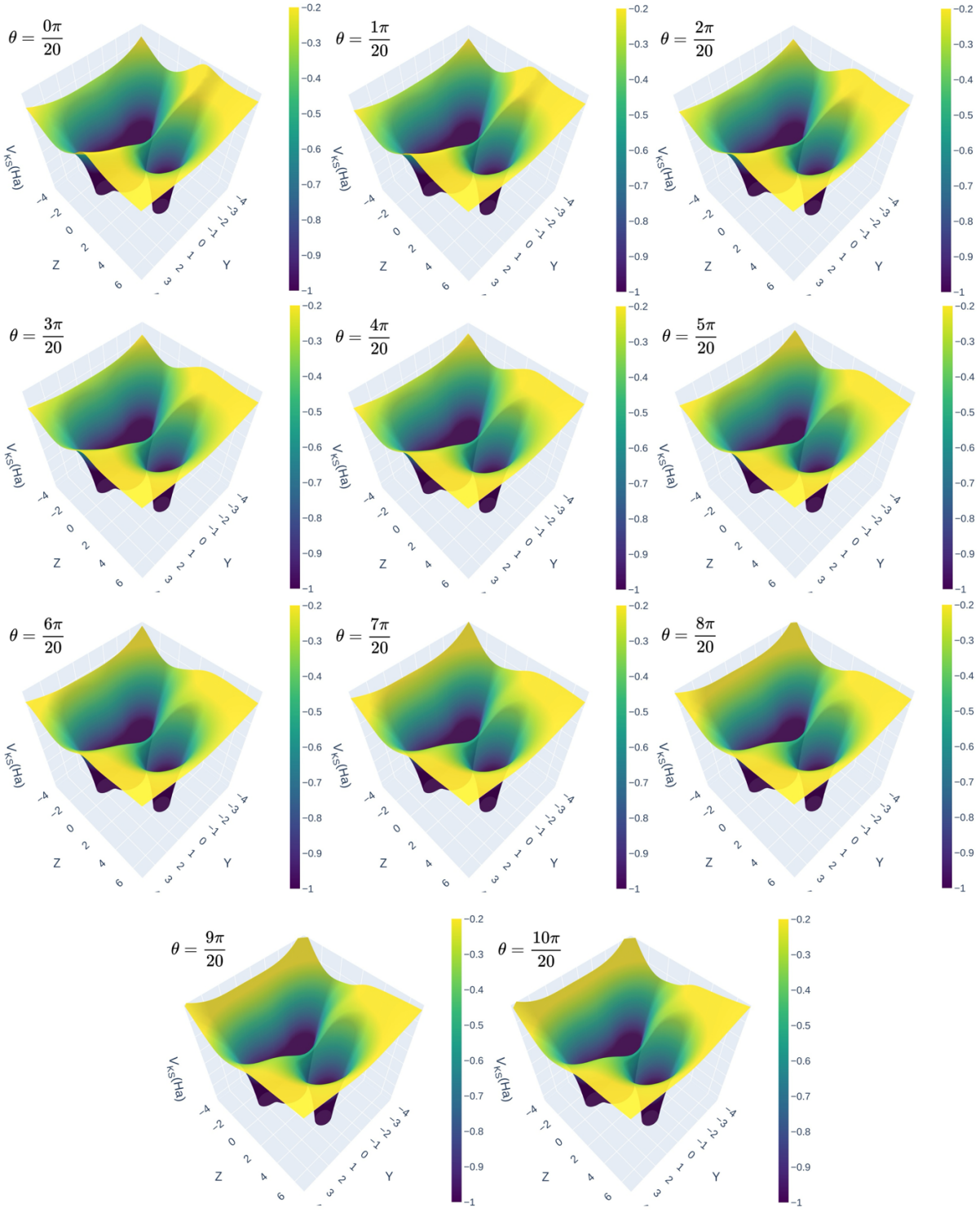

Appendix Figure C.2: The Kohn-Sham potential for NH_3 at different theta along the YZ plane in which the geometry also exists. The coordinates are in a.u.

C.4 Full Scan KS Orbitals

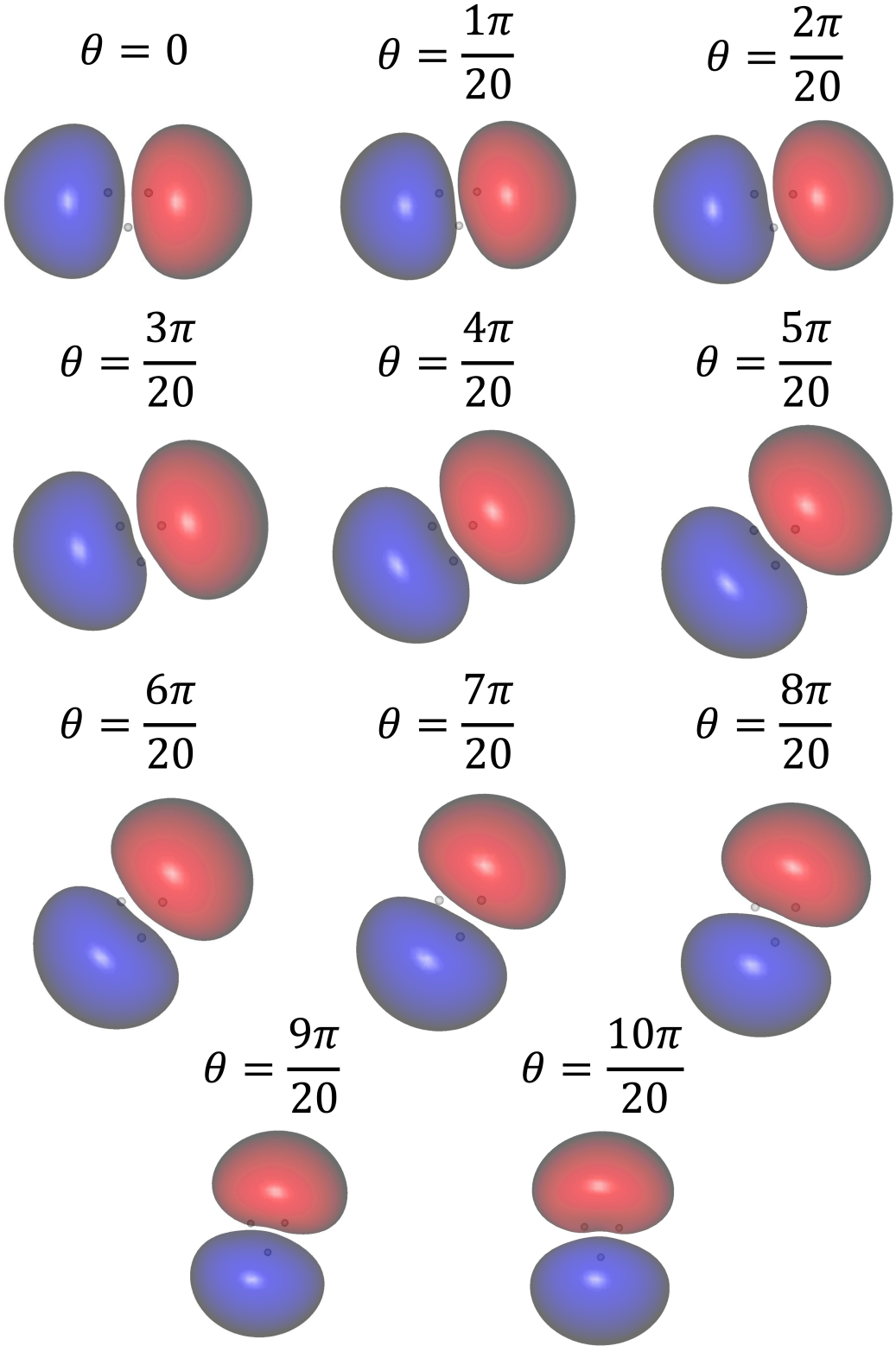

Appendix Figure C.3: KSO2 for the H_3 system with varying theta.

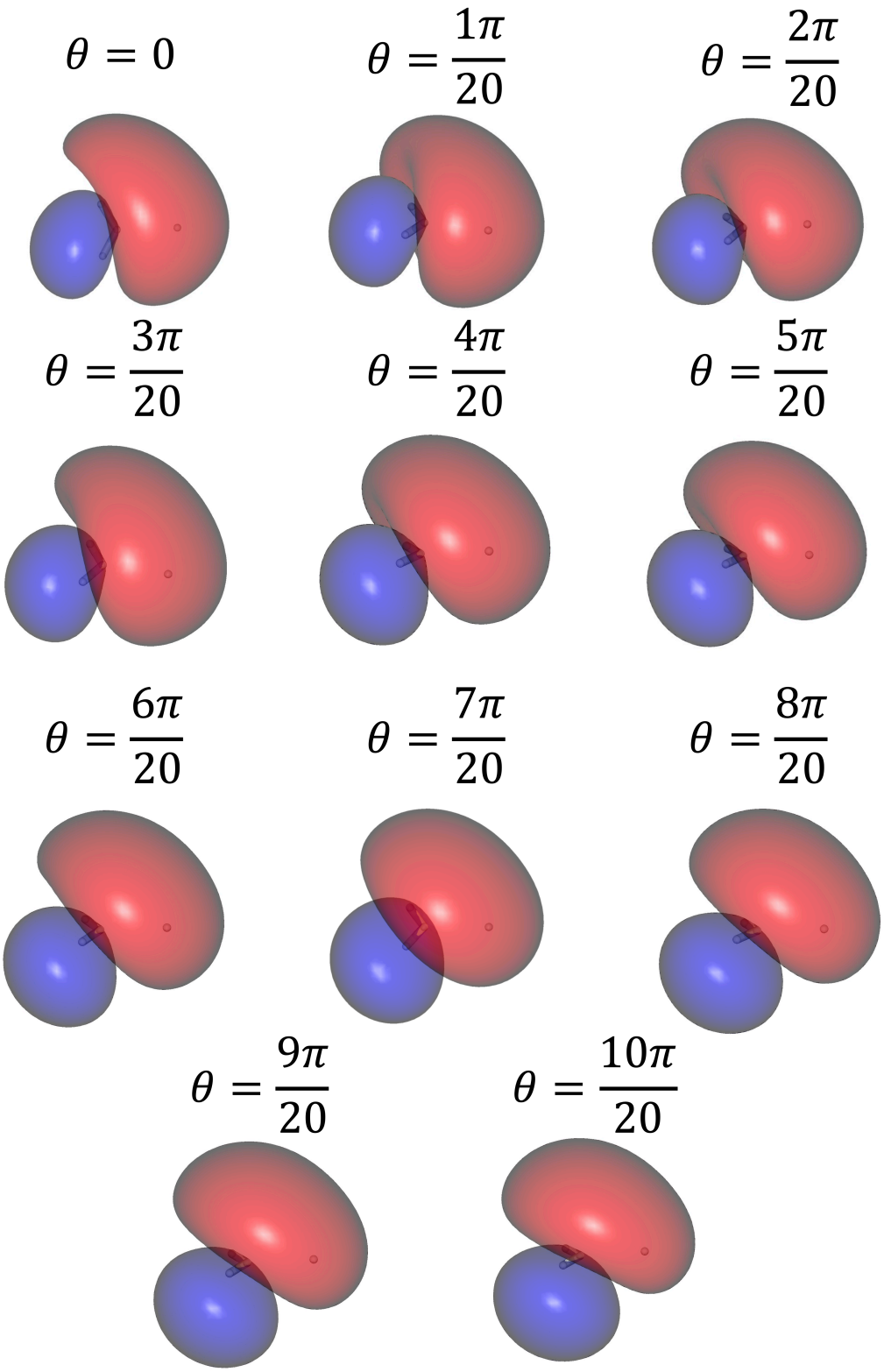

Appendix Figure C.4: KSO4 for the NH_3 system with varying theta.

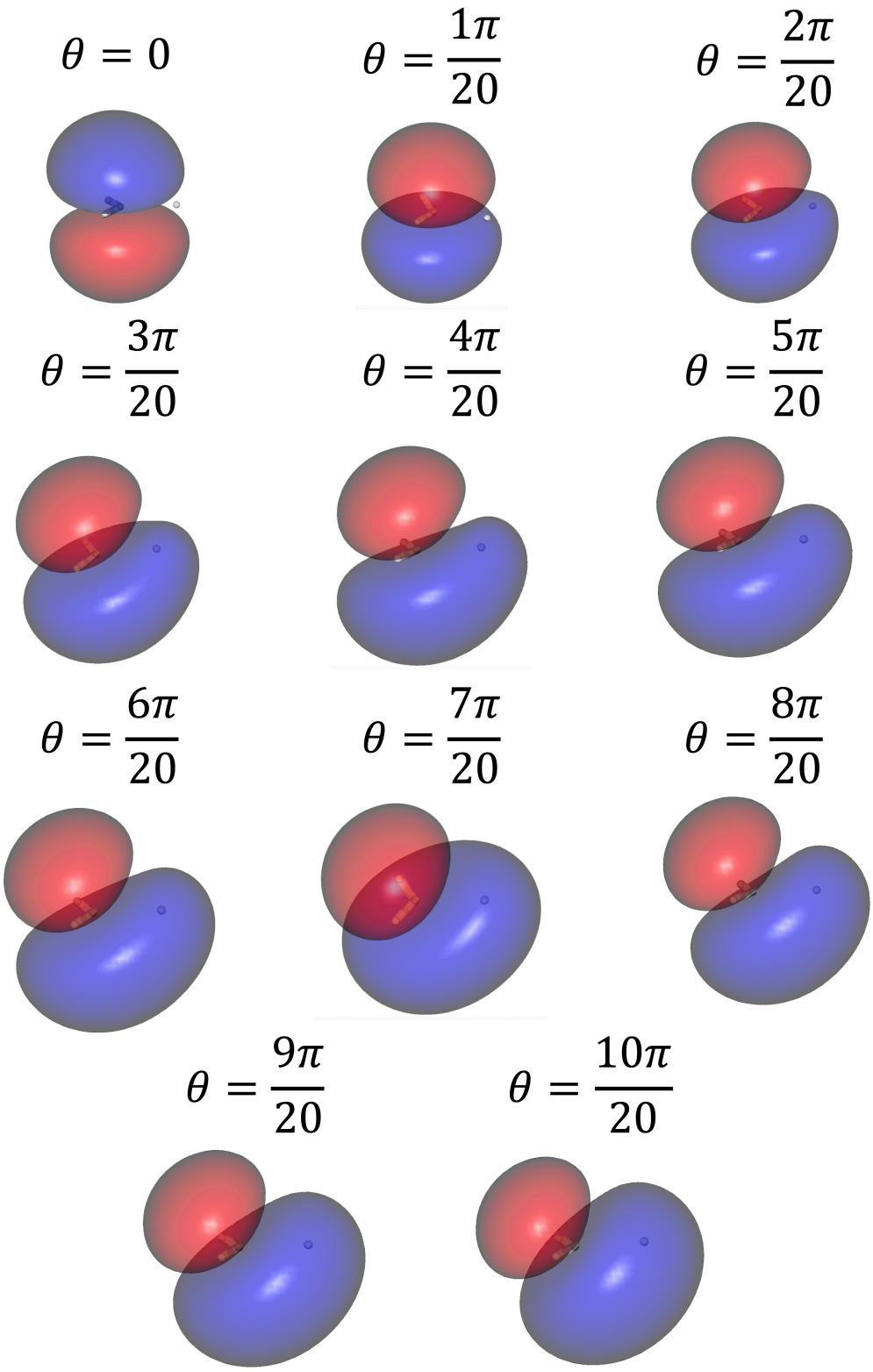

Appendix Figure C.5: KSO5 for the NH_3 system with varying theta.

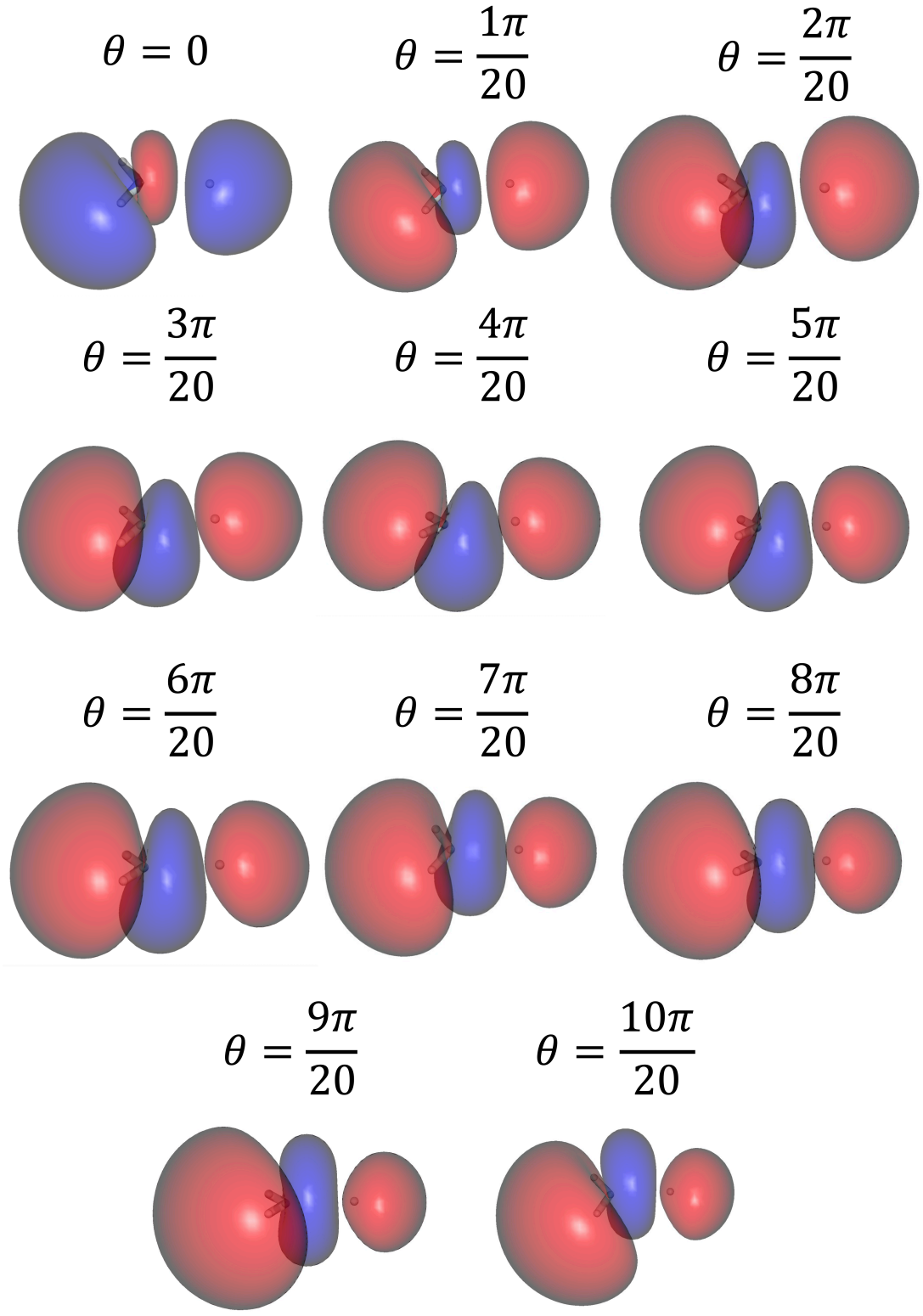

Appendix Figure C.6: KSO6 for the NH_3 system with varying theta.

C.5 Full Scan Classical Turning Surfaces

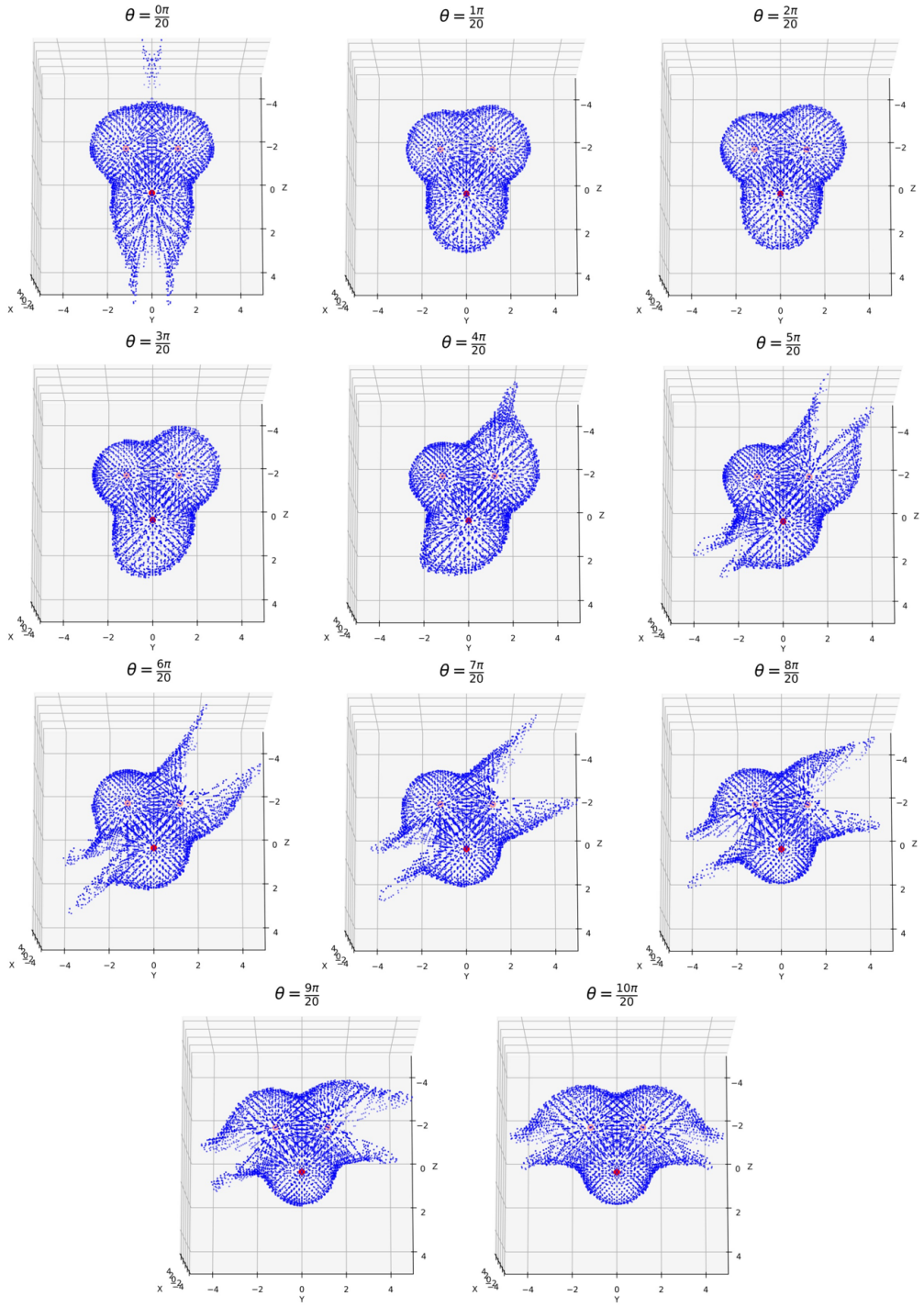

Appendix Figure C.7: Classical turning surface for H_3, the points are at a tolerance of 0.015 Ha of the ionization potential (-0.275 Ha) and points which density greater than 1×10^{-4} are included. The coordinates are in a.u.

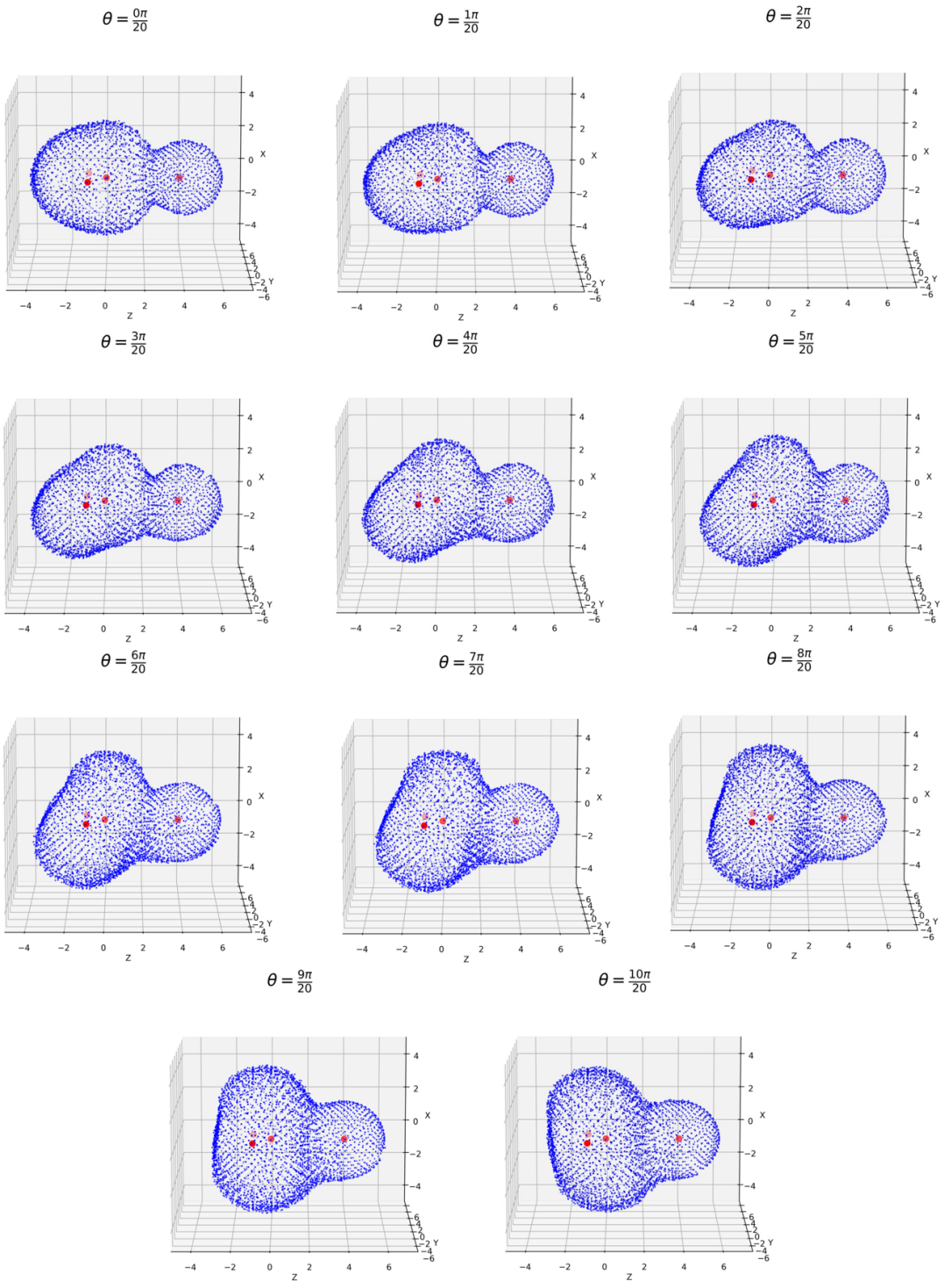

Appendix Figure C.8: Classical turning surface for NH_3, the points are at a tolerance of 0.015 Ha of the ionization potential (-0.328 Ha) and points which density greater than 1×10^{-5} are included. The coordinates are in a.u.

C.6 Natural Orbitals

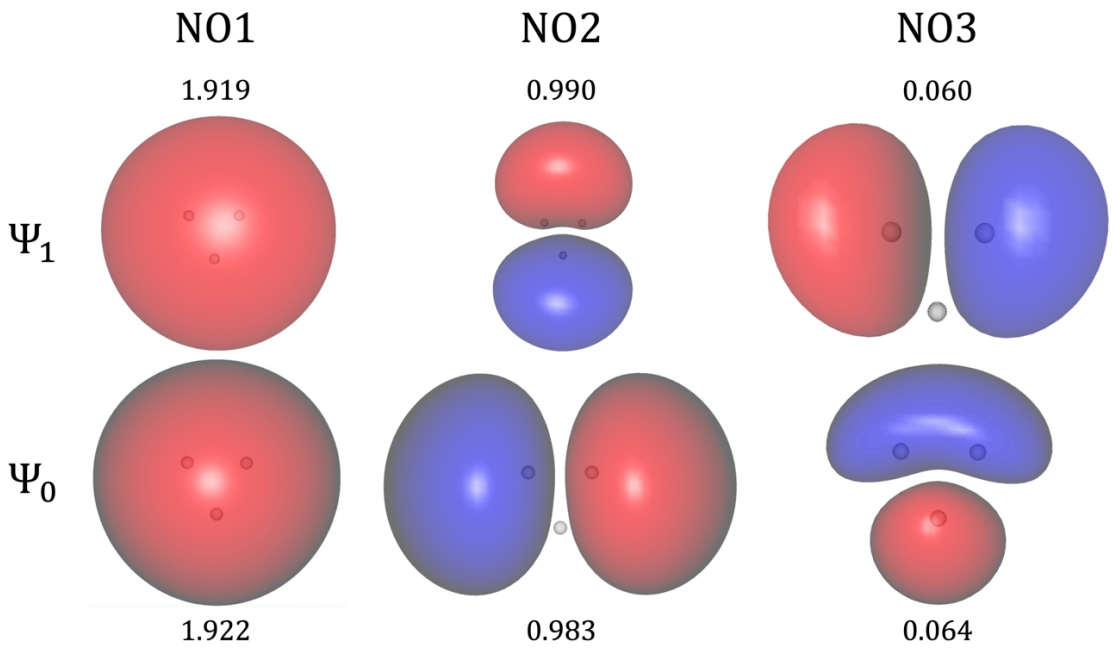

Appendix Figure C.9: The first 3 natural orbitals obtained from HBCI for the Ψ_0 and Ψ_1 states of H_3. An isovalue of 0.05 was used and occupancies are given.

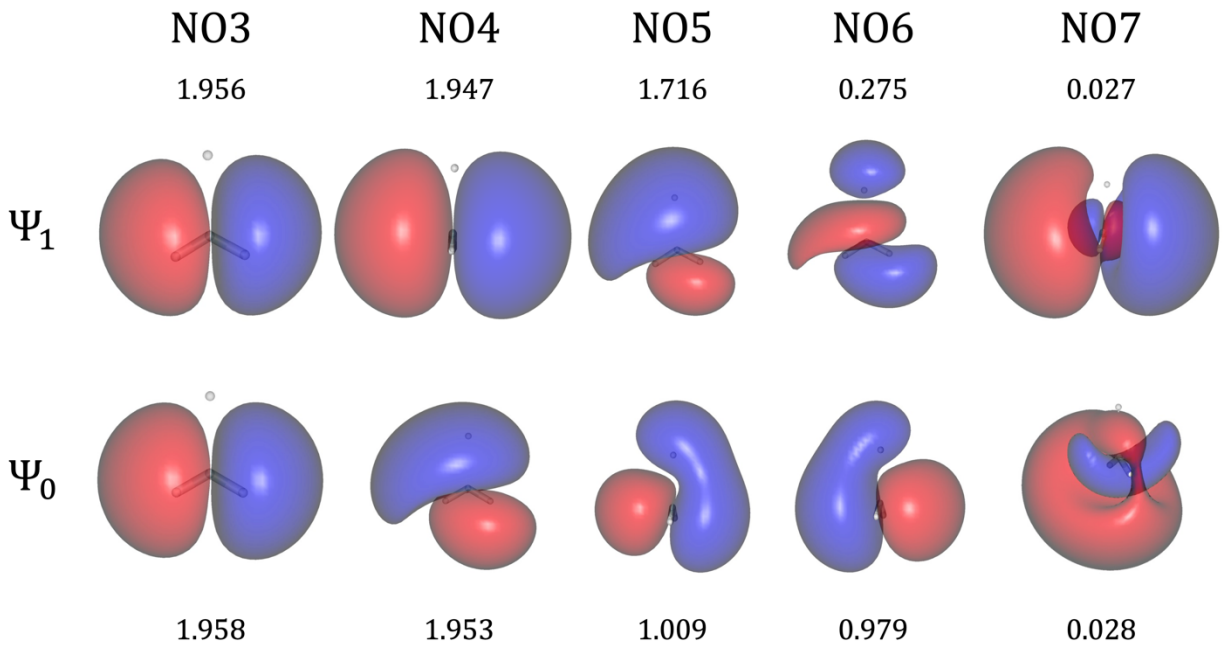

Appendix Figure C.10: Natural orbitals 3-7 obtained from HBCI for the Ψ_0 and Ψ_1 states of NH_3. An isovalue of 0.05 was used and occupancies are given.

Bibliography

1. Khanna, V.; Kanungo, B.; Hatch, J.; Kammeraad, J.; Zimmerman, P. M. Exchange-Correlation Potentials and Energy Densities through Orbital Averaging and Aufbau Integration. *J. Phys. Chem. A* **2025**, *129* (18), 4162–4173. https://doi.org/10.1021/acs.jpca.5c01288
2. Szabo, A.; Ostlund, N. S. *Modern Quantum Chemistry: Introduction to Advanced Electronic Structure Theory*. Dover Publications, Inc., first edition, **1996**.
3. Helgaker, T.; Jørgensen, P.; Olsen, J. *Molecular Electronic Structure Theory*; John Wiley & Sons, Ltd., **2000**.
4. Schrödinger, E. Quantisierung Als Eigenwertproblem. *Annalen der Physik* **1926**, *384* (4), 361–376. https://doi.org/10.1002/andp.19263840404
5. Born, M.; Oppenheimer, R. Zur Quantentheorie Der Molekeln. *Annalen der Physik* **1927**, *389* (20), 457–484. https://doi.org/10.1002/andp.19273892002
6. Slater, J. C. Analytic Atomic Wave Functions. *Phys. Rev.* **1932**, *42* (1), 33–43. https://doi.org/10.1103/PhysRev.42.33
7. Yu, T.; Si, Y.; Zhou, J. General Expressions of Molecular Multicenter Integrals for Slater-Type Orbitals. *International Journal of Quantum Chemistry* **2023**, *123* (15), e27128. https://doi.org/10.1002/qua.27128
8. Boys, S. F.; Egerton, A. C. Electronic Wave Functions - I. A General Method of Calculation for the Stationary States of Any Molecular System. *Proceedings of the Royal Society of London. Series A. Mathematical and Physical Sciences* **1950**, *200* (1063), 542–554. https://doi.org/10.1098/rspa.1950.0036
9. Ireland, R. T.; McKemmish, L. K. On the Specialization of Gaussian Basis Sets for Core-Dependent Properties. *J. Chem. Phys.* **2023**, *159* (6), 064102. https://doi.org/10.1063/5.0159119
10. Slater, J. C. The Theory of Complex Spectra. *Phys. Rev.* **1929**, *34* (10), 1293–1322. https://doi.org/10.1103/PhysRev.34.1293

11. Hall, G. G. The Molecular Orbital Theory of Chemical Valency VIII. A Method of Calculating Ionization Potentials. *Proc. A* **1951**, *205* (1083), 541–552. https://doi.org/10.1098/rspa.1951.0048
12. Roothaan, C. C. J. New Developments in Molecular Orbital Theory. *Rev. Mod. Phys.* **1951**, *23* (2), 69–89. https://doi.org/10.1103/RevModPhys.23.69
13. Löwdin, P.-O. Quantum Theory of Many-Particle Systems. III. Extension of the Hartree-Fock Scheme to Include Degenerate Systems and Correlation Effects. *Phys. Rev.* **1955**, *97* (6), 1509–1520. https://doi.org/10.1103/PhysRev.97.1509
14. Dirac, P. A. M. The Quantum Theory of the Electron. *Proceedings of the Royal Society of London. Series A, Containing Papers of a Mathematical and Physical Character* **1928**, *117* (778), 610–624. https://doi.org/10.1098/rspa.1928.0023
15. Saue, T. Relativistic Hamiltonians for Chemistry: A Primer. *ChemPhysChem* **2011**, *12* (17), 3077–3094. https://doi.org/10.1002/cphc.201100682
16. Peng, D.; Reiher, M. Exact Decoupling of the Relativistic Fock Operator. *Theor Chem Acc* **2012**, *131* (1), 1081. https://doi.org/10.1007/s00214-011-1081-y
17. Liu, W.; Peng, D. Infinite-Order Quasirelativistic Density Functional Method Based on the Exact Matrix Quasirelativistic Theory. *The Journal of Chemical Physics* **2006**, *125* (4), 044102. https://doi.org/10.1063/1.2222365
18. Iliaš, M.; Saue, T. An Infinite-Order Two-Component Relativistic Hamiltonian by a Simple One-Step Transformation. *The Journal of Chemical Physics* **2007**, *126* (6), 064102. https://doi.org/10.1063/1.2436882
19. Wenjian, L.; Daoling, P. Exact Two-Component Hamiltonians Revisited. *Journal of Chemical Physics* **2009**, *131* (3). https://doi.org/10.1063/1.3159445
20. Knecht, S.; Repisky, M.; Jensen, H. J. A.; Saue, T. Exact Two-Component Hamiltonians for Relativistic Quantum Chemistry: Two-Electron Picture-Change Corrections Made Simple. *The Journal of Chemical Physics* **2022**, *157* (11), 114106. https://doi.org/10.1063/5.0095112
21. Dyall, K. G. Interfacing Relativistic and Nonrelativistic Methods. I. Normalized Elimination of the Small Component in the Modified Dirac Equation. *J. Chem. Phys.* **1997**, *106* (23), 9618–9626. https://doi.org/10.1063/1.473860

22. Löwdin, P.-O.; Shull, H. Natural Orbitals in the Quantum Theory of Two-Electron Systems. *Phys. Rev.* **1956**, *101* (6), 1730–1739. https://doi.org/10.1103/PhysRev.101.1730
23. Davidson, E. R. Properties and Uses of Natural Orbitals. *Rev. Mod. Phys.* **1972**, *44* (3), 451–464. https://doi.org/10.1103/RevModPhys.44.451
24. Illas, F.; Rubio, J.; Ricart, J. M. Approximate Natural Orbitals and the Convergence of a Second Order Multireference Many-body Perturbation Theory (CIPSI) Algorithm. *The Journal of Chemical Physics* **1988**, *89* (10), 6376–6384. https://doi.org/10.1063/1.455405
25. Löwdin, P.-O. Quantum Theory of Many-Particle Systems. I. Physical Interpretations by Means of Density Matrices, Natural Spin-Orbitals, and Convergence Problems in the Method of Configurational Interaction. *Phys. Rev.* **1955**, *97* (6), 1474–1489. https://doi.org/10.1103/PhysRev.97.1474
26. Williams, C. I.; Suba, S.; Whitehead, M. A. Electron Correlation and Natural Orbitals: Fractional Orbital Occupancy Numbers, Configuration Interaction Expansion Coefficients and One-Particle Energies. *Journal of Molecular Structure: THEOCHEM* **1999**, *491* (1), 265–273. https://doi.org/10.1016/S0166-1280(99)00129-3
27. Piris, M. Global Natural Orbital Functional: Towards the Complete Description of the Electron Correlation. *Phys. Rev. Lett.* **2021**, *127* (23), 233001. https://doi.org/10.1103/PhysRevLett.127.233001
28. Materia, D.; Ratini, L.; Angeli, C.; Guidoni, L. Quantum Information Reveals That Orbital-Wise Correlation Is Essentially Classical in Natural Orbitals. *J. Chem. Phys.* **2024**, *161* (24), 244108. https://doi.org/10.1063/5.0220306
29. Hylleraas, E. A. Über den Grundzustand des Heliumatoms. *Z. Physik* **1928**, *48* (7), 469–494. https://doi.org/10.1007/BF01340013
30. Boys, S. F. The Integral Formulae for the Variational Solution of the Molecular Many-Electron Wave Equation in Terms of Gaussian Functions with Direct Electronic Correlation. *Proc. A* **1960**, *258* (1294), 402–411. https://doi.org/10.1098/rspa.1960.0195
31. Gao, H.; Imamura, S.; Kasagi, A.; Yoshida, E. Distributed Implementation of Full Configuration Interaction for One Trillion Determinants. *J. Chem. Theory Comput.* **2024**, *20* (3), 1185–1192. https://doi.org/10.1021/acs.jctc.3c01190

32. Shayit, A.; Liao, C.; Upadhyay, S.; Hu, H.; Zhang, T.; DePrince III, A. E.; Yang, C.; Li, X. Numerically Exact Configuration Interaction at Quadrillion-Determinant Scale. *Nat Commun* **2025**, *16* (1), 11016. https://doi.org/10.1038/s41467-025-65967-7

33. Harrison, R. J. Approximating Full Configuration Interaction with Selected Configuration Interaction and Perturbation Theory. *The Journal of Chemical Physics* **1991**, *94* (7), 5021–5031. https://doi.org/10.1063/1.460537

34. Eriksen, J. J. The Shape of Full Configuration Interaction to Come. *J. Phys. Chem. Lett.* **2021**, *12* (1), 418–432. https://doi.org/10.1021/acs.jpclett.0c03225

35. Huron, B.; Malrieu, J. P.; Rancurel, P. Iterative Perturbation Calculations of Ground and Excited State Energies from Multiconfigurational Zeroth-order Wavefunctions. *J. Chem. Phys.* **1973**, *58* (12), 5745–5759. https://doi.org/10.1063/1.1679199

36. Evangelisti, S.; Daudey, J.-P.; Malrieu, J.-P. Convergence of an Improved CIPSI Algorithm. *Chemical Physics* **1983**, *75* (1), 91–102. https://doi.org/10.1016/0301-0104(83)85011-3

37. Cimiraglia, R.; Persico, M. Recent Advances in Multireference Second Order Perturbation CI: The CIPSI Method Revisited. *Journal of Computational Chemistry* **1987**, *8* (1), 39–47. https://doi.org/10.1002/jcc.540080105

38. Garniron, Y.; Scemama, A.; Giner, E.; Caffarel, M.; Loos, P.-F. Selected Configuration Interaction Dressed by Perturbation. *The Journal of Chemical Physics* **2018**, *149* (6), 064103. https://doi.org/10.1063/1.5044503

39. Tubman, N. M.; Lee, J.; Takeshita, T. Y.; Head-Gordon, M.; Whaley, K. B. A Deterministic Alternative to the Full Configuration Interaction Quantum Monte Carlo Method. *J. Chem. Phys.* **2016**, *145* (4), 044112. https://doi.org/10.1063/1.4955109

40. Tubman, N. M.; Freeman, C. D.; Levine, D. S.; Hait, D.; Head-Gordon, M.; Whaley, K. B. Modern Approaches to Exact Diagonalization and Selected Configuration Interaction with the Adaptive Sampling CI Method. *J. Chem. Theory Comput.* **2020**, *16* (4), 2139–2159. https://doi.org/10.1021/acs.jctc.8b00536

41. Williams-Young, D. B.; Tubman, N. M.; Mejuto-Zaera, C.; de Jong, W. A. A Parallel, Distributed Memory Implementation of the Adaptive Sampling Configuration Interaction Method. *The Journal of Chemical Physics* **2023**, *158* (21), 214109. https://doi.org/10.1063/5.0148650

42. Holmes, A. A.; Tubman, N. M.; Umrigar, C. J. Heat-Bath Configuration Interaction: An Efficient Selected Configuration Interaction Algorithm Inspired by Heat-Bath Sampling. *J. Chem. Theory Comput.* **2016**, *12* (8), 3674–3680. https://doi.org/10.1021/acs.jctc.6b00407

43. Sharma, S.; Holmes, A. A.; Jeanmairet, G.; Alavi, A.; Umrigar, C. J. Semistochastic Heat-Bath Configuration Interaction Method: Selected Configuration Interaction with Semistochastic Perturbation Theory. *J. Chem. Theory Comput.* **2017**, *13* (4), 1595–1604. https://doi.org/10.1021/acs.jctc.6b01028

44. Li, J.; Otten, M.; Holmes, A. A.; Sharma, S.; Umrigar, C. J. Fast Semistochastic Heat-Bath Configuration Interaction. *J. Chem. Phys.* **2018**, *149* (21), 214110. https://doi.org/10.1063/1.5055390

45. Dang, D.-K.; Kammeraad, J. A.; Zimmerman, P. M. Advances in Parallel Heat Bath Configuration Interaction. *J. Phys. Chem. A* **2023**, *127* (1), 400–411. https://doi.org/10.1021/acs.jpca.2c07949

46. Nesbet, R. K.; Hartree, D. R. Configuration Interaction in Orbital Theories. *Proceedings of the Royal Society of London. Series A. Mathematical and Physical Sciences* **1955**, *230* (1182), 312–321. https://doi.org/10.1098/rspa.1955.0134

47. Chien, A. D.; Holmes, A. A.; Otten, M.; Umrigar, C. J.; Sharma, S.; Zimmerman, P. M. Excited States of Methylene, Polyenes, and Ozone from Heat-Bath Configuration Interaction. *J. Phys. Chem. A* **2018**, *122* (10), 2714–2722. https://doi.org/10.1021/acs.jpca.8b01554

48. Löwdin, P.-O. Studies in Perturbation Theory. X. Lower Bounds to Energy Eigenvalues in Perturbation-Theory Ground State. *Phys. Rev.* **1965**, *139* (2A), A357–A372. https://doi.org/10.1103/PhysRev.139.A357

49. Hohenberg, P.; Kohn, W. Inhomogeneous Electron Gas. *Phys. Rev.* **1964**, *136* (3B), B864–B871. https://doi.org/10.1103/PhysRev.136.B864

50. Levy, M. Universal Variational Functionals of Electron Densities, First-Order Density Matrices, and Natural Spin-Orbitals and Solution of the v-Representability Problem. *Proceedings of the National Academy of Sciences* **1979**, *76* (12), 6062–6065. https://doi.org/10.1073/pnas.76.12.6062

51. Kohn, W.; Sham, L. J. Self-Consistent Equations Including Exchange and Correlation Effects. *Phys. Rev.* **1965**, *140* (4A), A1133–A1138. https://doi.org/10.1103/PhysRev.140.A1133

52. Gritsenko, O. V.; Baerends, E. J. Effect of Molecular Dissociation on the Exchange-Correlation Kohn-Sham Potential. *Phys. Rev. A* **1957**, *54* (3), 1957–1972. https://doi.org/10.1103/PhysRevA.54.1957

53. Gritsenko, O.; van Leeuwen, R.; Baerends, E. J. Analysis of Electron Interaction and Atomic Shell Structure in Terms of Local Potentials. *J. Chem. Phys.* **1994**, *101* (10), 8955–8963. https://doi.org/10.1063/1.468024

54. Gritsenko, O. V.; Leeuwen, R. van; Baerends, E. J. Molecular Exchange-correlation Kohn–Sham Potential and Energy Density from Ab Initio First- and Second-order Density Matrices: Examples for XH (X=Li, B, F). *J. Chem. Phys.* **1996**, *104* (21), 8535–8545. https://doi.org/10.1063/1.471602

55. Gritsenko, O. V.; Schipper, P. R. T.; Baerends, E. J. Effect of Pauli Repulsion on the Molecular Exchange-Correlation Kohn-Sham Potential: A Comparative Calculation of Ne_2 and N_2. *Phys. Rev. A* **1998**, *57* (5), 3450–3457. https://doi.org/10.1103/PhysRevA.57.3450

56. Gritsenko, O.; Baerends, E. J. Correct Dissociation Limit for the Exchange-Correlation Energy and Potential. *International Journal of Quantum Chemistry* **2006**, *106* (15), 3167–3177. https://doi.org/10.1002/qua.21100

57. Kohut, S. V.; Polgar, A. M.; Staroverov, V. N. Origin of the Step Structure of Molecular Exchange–Correlation Potentials. *Phys. Chem. Chem. Phys.* **2016**, *18* (31), 20938–20944. https://doi.org/10.1039/C6CP00878J

58. Shi, Y.; Wasserman, A. Inverse Kohn–Sham Density Functional Theory: Progress and Challenges. *J. Phys. Chem. Lett.* **2021**, *12* (22), 5308–5318. https://doi.org/10.1021/acs.jpclett.1c00752

59. van Leeuwen, R.; Baerends, E. J. Exchange-Correlation Potential with Correct Asymptotic Behavior. *Phys. Rev. A* **1994**, *49* (4), 2421–2431. https://doi.org/10.1103/PhysRevA.49.2421

60. Gritsenko, O. V.; van Leeuwen, R.; Baerends, E. J. Molecular Kohn-Sham Exchange-Correlation Potential from the Correlated Ab Initio Electron Density. *Phys. Rev. A* **1995**, *52* (3), 1870–1874. https://doi.org/10.1103/PhysRevA.52.1870

61. Kananenka, A. A.; Kohut, S. V.; Gaiduk, A. P.; Ryabinkin, I. G.; Staroverov, V. N. Efficient Construction of Exchange and Correlation Potentials by Inverting the Kohn–Sham Equations. *J. Chem. Phys.* **2013**, *139* (7), 074112. https://doi.org/10.1063/1.4817942

62. Talman, J. D.; Shadwick, W. F. Optimized Effective Atomic Central Potential. *Phys. Rev. A* **1976**, *14* (1), 36–40. https://doi.org/10.1103/PhysRevA.14.36

63. Ivanov, S.; Hirata, S.; Bartlett, R. J. Exact Exchange Treatment for Molecules in Finite-Basis-Set Kohn-Sham Theory. *Phys. Rev. Lett.* **1999**, *83* (26), 5455–5458. https://doi.org/10.1103/PhysRevLett.83.5455

64. Hirata, S.; Ivanov, S.; Grabowski, I.; Bartlett, R. J.; Burke, K.; Talman, J. D. Can Optimized Effective Potentials Be Determined Uniquely? *J. Chem. Phys.* **2001**, *115* (4), 1635–1649. https://doi.org/10.1063/1.1381013

65. Kümmel, S.; Perdew, J. P. Simple Iterative Construction of the Optimized Effective Potential for Orbital Functionals, Including Exact Exchange. *Phys. Rev. Lett.* **2003**, *90* (4), 043004. https://doi.org/10.1103/PhysRevLett.90.043004

66. Casida, M. E. Generalization of the Optimized-Effective-Potential Model to Include Electron Correlation: A Variational Derivation of the Sham-Schlüter Equation for the Exact Exchange-Correlation Potential. *Phys. Rev. A* **1995**, *51* (3), 2005–2013. https://doi.org/10.1103/PhysRevA.51.2005

67. Riemelmoser, S.; Kaltak, M.; Kresse, G. Optimized Effective Potentials from the Random-Phase Approximation: Accuracy of the Quasiparticle Approximation. *J. Chem. Phys.* **2021**, *154* (15), 154103. https://doi.org/10.1063/5.0045400

68. Hadamard, J. Sur les Problemes Aux Derivees Partielles et Leur Signification Physique. *Princeton Univ. Bull.* **1902**, *13*, 49–52.

69. Kanungo, B.; Zimmerman, P. M.; Gavini, V. Exact Exchange-Correlation Potentials from Ground-State Electron Densities. *Nat Commun* **2019**, *10* (1), 4497. https://doi.org/10.1038/s41467-019-12467-0

70. Ryabinkin, I. G.; Kohut, S. V.; Staroverov, V. N. Reduction of Electronic Wave Functions to Kohn-Sham Effective Potentials. *Phys. Rev. Lett.* **2015**, *115* (8), 083001. https://doi.org/10.1103/PhysRevLett.115.083001

71. Tribedi, S.; Dang, D.-K.; Kanungo, B.; Gavini, V.; Zimmerman, P. M. Exchange Correlation Potentials from Full Configuration Interaction in a Slater Orbital Basis. *The Journal of Chemical Physics* **2023**, *159* (5), 054106. https://doi.org/10.1063/5.0157942

72. Rask, A. E.; Li, L.; Zimmerman, P. M. Kohn–Sham Density in a Slater Orbital Basis Set. *J. Phys. Chem. A* **2024**, *128* (16), 3194–3204. https://doi.org/10.1021/acs.jpca.3c08303

73. Levy, M.; Perdew, J. P. Hellmann-Feynman, Virial, and Scaling Requisites for the Exact Universal Density Functionals. Shape of the Correlation Potential and Diamagnetic Susceptibility for Atoms. *Phys. Rev. A* **1985**, *32* (4), 2010–2021. https://doi.org/10.1103/PhysRevA.32.2010

74. Schmidt, T.; Kraisler, E.; Kronik, L.; Kümmel, S. One-Electron Self-Interaction and the Asymptotics of the Kohn–Sham Potential: An Impaired Relation. *Phys. Chem. Chem. Phys.* **2014**, *16* (28), 14357–14367. https://doi.org/10.1039/C3CP55433C

75. Wu, Q.; Ayers, P. W.; Yang, W. Density-Functional Theory Calculations with Correct Long-Range Potentials. *J. Chem. Phys.* **2003**, *119* (6), 2978–2990. https://doi.org/10.1063/1.1590631

76. Kraisler, E. Asymptotic Behavior of the Exchange-Correlation Energy Density and the Kohn-Sham Potential in Density Functional Theory: Exact Results and Strategy for Approximations. *Israel Journal of Chemistry* **2020**, *60* (8–9), 805–822. https://doi.org/10.1002/ijch.201900103

77. Stark, A.; Meier, N.; Hatch, J.; Kammeraad, J. A.; Dang, D.-K.; Zimmerman, P. M. Numerical Integration of Slater Basis Functions Over Prolate Spheroidal Grids. *Journal of Computational Chemistry* **2026**, *47* (1), e70291. https://doi.org/10.1002/jcc.70291

78. Slater, J. C. Central Fields and Rydberg Formulas in Wave Mechanics. *Phys. Rev.* **1928**, *31* (3), 333–343. https://doi.org/10.1103/PhysRev.31.333

79. Kato, T. On the Eigenfunctions of Many-Particle Systems in Quantum Mechanics. *Communications on Pure and Applied Mathematics* **1957**, *10* (2), 151–177. https://doi.org/10.1002/cpa.3160100201

80. Kurokawa, Y. I.; Nakashima, H.; Nakatsuji, H. General Coalescence Conditions for the Exact Wave Functions. II. Higher-Order Relations for Many-Particle Systems. *J. Chem. Phys.* **2014**, *140* (21), 214103. https://doi.org/10.1063/1.4879266

81. Reinhardt, P.; Hoggan, P. E. Cusps and Derivatives for Wave-Functions Expanded in Slater Orbitals: A Density Study. *International Journal of Quantum Chemistry* **2009**, *109* (14), 3191–3198. https://doi.org/10.1002/qua.22156

82. Chong, D. P.; Grüning, M.; Baerends, E. J. STO and GTO Field-Induced Polarization Functions for H to Kr. *Journal of Computational Chemistry* **2003**, *24* (13), 1582–1591. https://doi.org/10.1002/jcc.10310

83. Hoggan, P. E. Choice of Atomic Orbitals to Evaluate Sensitive Properties of Molecules: An Example of NMR Chemical Shifts. *International Journal of Quantum Chemistry* **2004**, *100* (2), 214–220. https://doi.org/10.1002/qua.20226

84. Watson, M. A.; Handy, N. C.; Cohen, A. J.; Helgaker, T. Density-Functional Generalized-Gradient and Hybrid Calculations of Electromagnetic Properties Using Slater Basis Sets. *The Journal of Chemical Physics* **2004**, *120* (16), 7252–7261. https://doi.org/10.1063/1.1668633

85. Roothaan, C. C. J. A Study of Two-Center Integrals Useful in Calculations on Molecular Structure. I. *J. Chem. Phys.* **1951**, *19* (12), 1445–1458. https://doi.org/10.1063/1.1748100

86. Absi, N.; Hoggan, P. Analytical Evaluation of Molecular Electronic Integrals Using Poisson's Equation: Exponential-Type Orbitals and Atom Pairs. *International Journal of Quantum Chemistry* **2006**, *106* (14), 2881–2888. https://doi.org/10.1002/qua.21114

87. Weatherford, C. A.; Red, E.; Joseph, D.; Hoggan, P. Poisson's Equation Solution of Coulomb Integrals in Atoms and Molecules†. *Molecular Physics* **2006**, *104* (9), 1385–1389. https://doi.org/10.1080/00268970500462248

88. Gill, P. M. W.; Head-Gordon, Martin.; Pople, J. A. Efficient Computation of Two-Electron - Repulsion Integrals and Their Nth-Order Derivatives Using Contracted Gaussian Basis Sets. *J. Phys. Chem.* **1990**, *94* (14), 5564–5572. https://doi.org/10.1021/j100377a031

89. Obara, S.; Saika, A. General Recurrence Formulas for Molecular Integrals over Cartesian Gaussian Functions. *The Journal of Chemical Physics* **1988**, *89* (3), 1540–1559. https://doi.org/10.1063/1.455717

90. Obara, S.; Saika, A. Efficient Recursive Computation of Molecular Integrals over Cartesian Gaussian Functions. *The Journal of Chemical Physics* **1986**, *84* (7), 3963–3974. https://doi.org/10.1063/1.450106
91. Head-Gordon, M.; Pople, J. A. A Method for Two-electron Gaussian Integral and Integral Derivative Evaluation Using Recurrence Relations. *The Journal of Chemical Physics* **1988**, *89* (9), 5777–5786. https://doi.org/10.1063/1.455553
92. Dang, D.-K.; Wilson, L. W.; Zimmerman, P. M. The Numerical Evaluation of Slater Integrals on Graphics Processing Units. *Journal of Computational Chemistry* **2022**, *43* (25), 1680–1689. https://doi.org/10.1002/jcc.26968
93. te Velde, G.; Baerends, E. J. Numerical Integration for Polyatomic Systems. *Journal of Computational Physics* **1992**, *99* (1), 84–98. https://doi.org/10.1016/0021-9991(92)90277-6
94. Boerrigter, P. M.; Te Velde, G.; Baerends, J. E. Three-Dimensional Numerical Integration for Electronic Structure Calculations. *International Journal of Quantum Chemistry* **1988**, *33* (2), 87–113. https://doi.org/10.1002/qua.560330204
95. Spadetto, E.; Philipsen, P. H. T.; Förster, A.; Visscher, L. Toward Pair Atomic Density Fitting for Correlation Energies with Benchmark Accuracy. *J. Chem. Theory Comput.* **2023**, *19* (5), 1499–1516. https://doi.org/10.1021/acs.jctc.2c01201
96. Baerends, E. J.; Aguirre, N. F.; Austin, N. D.; Autschbach, J.; Bickelhaupt, F. M.; Bulo, R.; Cappelli, C.; Van Duin, A. C. T.; Egidi, F.; Fonseca Guerra, C.; Förster, A. et al. The Amsterdam Modeling Suite. *The Journal of Chemical Physics* **2025**, *162* (16), 162501. https://doi.org/10.1063/5.0258496
97. Franchini, M.; Philipsen, P. H. T.; Visscher, L. The Becke Fuzzy Cells Integration Scheme in the Amsterdam Density Functional Program Suite. *Journal of Computational Chemistry* **2013**, *34* (21), 1819–1827. https://doi.org/10.1002/jcc.23323
98. Becke, A. D. A Multicenter Numerical Integration Scheme for Polyatomic Molecules. *The Journal of Chemical Physics* **1988**, *88* (4), 2547–2553. https://doi.org/10.1063/1.454033
99. Sen, S.; Senjean, B.; Visscher, L. Characterization of Excited States in Time-Dependent Density Functional Theory Using Localized Molecular Orbitals. *The Journal of Chemical Physics* **2023**, *158* (5), 054115. https://doi.org/10.1063/5.0137729

100. Grimmel, S. A.; Teodoro, T. Q.; Visscher, L. Is It Worthwhile to Go beyond the Local-Density Approximation in Subsystem Density Functional Theory? *International Journal of Quantum Chemistry* **2020**, *120* (21), e26111. https://doi.org/10.1002/qua.26111

101. Förster, A.; Visscher, L. GW100: A Slater-Type Orbital Perspective. *J. Chem. Theory Comput.* **2021**, *17* (8), 5080–5097. https://doi.org/10.1021/acs.jctc.1c00308

102. Förster, A.; van Lenthe, E.; Spadetto, E.; Visscher, L. Two-Component GW Calculations: Cubic Scaling Implementation and Comparison of Vertex-Corrected and Partially Self-Consistent GW Variants. *J. Chem. Theory Comput.* **2023**, *19* (17), 5958–5976. https://doi.org/10.1021/acs.jctc.3c00512

103. Förster, A.; Visscher, L. Low-Order Scaling G0W0 by Pair Atomic Density Fitting. *J. Chem. Theory Comput.* **2020**, *16* (12), 7381–7399. https://doi.org/10.1021/acs.jctc.0c00693

104. Förster, A.; Visscher, L. Low-Order Scaling Quasiparticle Self-Consistent GW for Molecules. *Front. Chem.* **2021**, *9*. https://doi.org/10.3389/fchem.2021.736591

105. Förster, A.; Visscher, L. Quasiparticle Self-Consistent GW-Bethe–Salpeter Equation Calculations for Large Chromophoric Systems. *J. Chem. Theory Comput.* **2022**, *18* (11), 6779–6793. https://doi.org/10.1021/acs.jctc.2c00531

106. Dunlap, B. I.; Connolly, J. W. D.; Sabin, J. R. On Some Approximations in Applications of Xα Theory. *The Journal of Chemical Physics* **1979**, *71* (8), 3396–3402. https://doi.org/10.1063/1.438728

107. Eichkorn, K.; Treutler, O.; Öhm, H.; Häser, M.; Ahlrichs, R. Auxiliary Basis Sets to Approximate Coulomb Potentials. *Chemical Physics Letters* **1995**, *240* (4), 283–290. https://doi.org/10.1016/0009-2614(95)00621-A

108. Distasio JR., R. A.; Steele, R. P.; Rhee, Y. M.; Shao, Y.; Head-Gordon, M. An Improved Algorithm for Analytical Gradient Evaluation in Resolution-of-the-Identity Second-Order Møller-Plesset Perturbation Theory: Application to Alanine Tetrapeptide Conformational Analysis. *Journal of Computational Chemistry* **2007**, *28* (5), 839–856. https://doi.org/10.1002/jcc.20604

109. Becke, A. D. Numerical Hartree–Fock–Slater Calculations on Diatomic Molecules. *The Journal of Chemical Physics* **1982**, *76* (12), 6037–6045. https://doi.org/10.1063/1.442958

110. Mura, M. E.; Knowles, P. J. Improved Radial Grids for Quadrature in Molecular Density-functional Calculations. *The Journal of Chemical Physics* **1996**, *104* (24), 9848–9858. https://doi.org/10.1063/1.471749

111. Lebedev, V. I. Quadratures on a Sphere. *USSR Computational Mathematics and Mathematical Physics* **1976**, *16* (2), 10–24. https://doi.org/10.1016/0041-5553(76)90100-2

112. Trefethen, L. N. Exactness of Quadrature Formulas. *SIAM Rev.* **2022**, *64* (1), 132–150. https://doi.org/10.1137/20M1389522

113. Lehtola, S. Automatic Generation of Accurate and Cost-Efficient Auxiliary Basis Sets. *J. Chem. Theory Comput.* **2023**, *19* (18), 6242–6254. https://doi.org/10.1021/acs.jctc.3c00670

114. Lehtola, S. Straightforward and Accurate Automatic Auxiliary Basis Set Generation for Molecular Calculations with Atomic Orbital Basis Sets. *J. Chem. Theory Comput.* **2021**, *17* (11), 6886–6900. https://doi.org/10.1021/acs.jctc.1c00607

115. Raffenetti, R. C. Even-tempered Atomic Orbitals. II. Atomic SCF Wavefunctions in Terms of Even-tempered Exponential Bases. *The Journal of Chemical Physics* **1973**, *59* (11), 5936–5949. https://doi.org/10.1063/1.1679962

116. Chong, D. P.; Van Lenthe, E.; Van Gisbergen, S.; Baerends, E. J. Even-tempered slater-type orbitals revisited: From hydrogen to krypton. *Journal of Computational Chemistry* **2004**, *25* (8), 1030–1036. https://doi.org/10.1002/jcc.20030

117. Limpanuparb, T.; Gill, P. M. W. Resolutions of the Coulomb Operator. *Phys. Chem. Chem. Phys.* **2009**, *11* (40), 9176–9181. https://doi.org/10.1039/B910613H

118. Hoggan, P. E. General Two-Electron Exponential Type Orbital Integrals in Polyatomics without Orbital Translations. *International Journal of Quantum Chemistry* **2009**, *109* (13), 2926–2932. https://doi.org/10.1002/qua.22128

119. Cohen, A. J.; Handy, N. C. Density Functional Generalized Gradient Calculations Using Slater Basis Sets. *J. Chem. Phys.* **2002**, *117* (4), 1470–1478. https://doi.org/10.1063/1.1485073

120. Epifanovsky, E.; Gilbert, A. T. B.; Feng, X.; Lee, J.; Mao, Y.; Mardirossian, N.; Pokhilko, P.; White, A. F.; Coons, M. P.; Dempwolff, A. L. et al. Software for the Frontiers of Quantum Chemistry: An Overview of Developments in the Q-Chem 5

Package. *The Journal of Chemical Physics* **2021**, *155* (8), 084801. https://doi.org/10.1063/5.0055522

121. Zimmerman, P. M. Incremental Full Configuration Interaction. *The Journal of Chemical Physics* **2017**, *146* (10), 104102. https://doi.org/10.1063/1.4977727

122. Zimmerman, P. M. Singlet–Triplet Gaps through Incremental Full Configuration Interaction. *J. Phys. Chem. A* **2017**, *121* (24), 4712–4720. https://doi.org/10.1021/acs.jpca.7b03998

123. Zimmerman, P. M. Strong Correlation in Incremental Full Configuration Interaction. *J. Chem. Phys.* **2017**, *146* (22), 224104. https://doi.org/10.1063/1.4985566

124. Hatch, J.; Zimmerman, P. M. Taming the Virtual Space for Incremental Full Configuration Interaction. *The Journal of Chemical Physics* **2025**, *163* (5), 054105. https://doi.org/10.1063/5.0267021

125. Hatch, J.; Rask, A. E.; Dang, D.-K.; Zimmerman, P. M. Many-Body Basis Set Amelioration Method for Incremental Full Configuration Interaction. *J. Phys. Chem. A* **2025**, *129* (16), 3743–3753. https://doi.org/10.1021/acs.jpca.5c01521

126. Čížek, J. On the Correlation Problem in Atomic and Molecular Systems. Calculation of Wavefunction Components in Ursell-Type Expansion Using Quantum-Field Theoretical Methods. *J. Chem. Phys.* **1966**, *45* (11), 4256–4266. https://doi.org/10.1063/1.1727484

127. Stanton, J. F. Why CCSD(T) Works: A Different Perspective. *Chemical Physics Letters* **1997**, *281* (1), 130–134. https://doi.org/10.1016/S0009-2614(97)01144-5

128. Neese, F.; Wennmohs, F.; Becker, U.; Riplinger, C. The ORCA Quantum Chemistry Program Package. *J. Chem. Phys.* **2020**, *152* (22), 224108. https://doi.org/10.1063/5.0004608

129. Neese, F. Software Update: The ORCA Program System—Version 5.0. *WIREs Computational Molecular Science* **2022**, *12* (5), e1606. https://doi.org/10.1002/wcms.1606

130. Neese, F. The SHARK Integral Generation and Digestion System. *Journal of Computational Chemistry* **2023**, *44* (3), 381–396. https://doi.org/10.1002/jcc.26942

131. Neese, F. The ORCA Program System. *WIREs Computational Molecular Science* **2012**, *2* (1), 73–78. https://doi.org/10.1002/wcms.81

132. Romanowski, Z. Numerical Calculation of Overlap and Kinetic Integrals in Prolate Spheroidal Coordinates. II. *International Journal of Quantum Chemistry* **2008**, *108* (3), 487–492. https://doi.org/10.1002/qua.21515

133. Sims, J. S.; Hagstrom, S. A. High Precision Variational Calculations for the Born-Oppenheimer Energies of the Ground State of the Hydrogen Molecule. *J. Chem. Phys.* **2006**, *124* (9), 094101. https://doi.org/10.1063/1.2173250

134. Gu, J.-P.; Hirsch, G.; Buenker, R. J.; Brumm, M.; Osmann, G.; Bunker, P. R.; Jensen, P. A Theoretical Study of the Absorption Spectrum of Singlet CH2. *Journal of Molecular Structure* **2000**, *517–518*, 247–264. https://doi.org/10.1016/S0022-2860(99)00256-2

135. Jensen, P.; Bunker, P. R. The Potential Surface and Stretching Frequencies of $\tilde{X}$ 3B1 Methylene (CH2) Determined from Experiment Using the Morse Oscillator-rigid Bender Internal Dynamics Hamiltonian. *The Journal of Chemical Physics* **1988**, *89* (3), 1327–1332. https://doi.org/10.1063/1.455184

136. Slipchenko, L. V.; Krylov, A. I. Singlet-Triplet Gaps in Diradicals by the Spin-Flip Approach: A Benchmark Study. *The Journal of Chemical Physics* **2002**, *117* (10), 4694–4708. https://doi.org/10.1063/1.1498819

137. Bernard, Y. A.; Shao, Y.; Krylov, A. I. General Formulation of Spin-Flip Time-Dependent Density Functional Theory Using Non-Collinear Kernels: Theory, Implementation, and Benchmarks. *The Journal of Chemical Physics* **2012**, *136* (20), 204103. https://doi.org/10.1063/1.4714499

138. Zimmerman, P. M.; Toulouse, J.; Zhang, Z.; Musgrave, C. B.; Umrigar, C. J. Excited States of Methylene from Quantum Monte Carlo. *The Journal of Chemical Physics* **2009**, *131* (12), 124103. https://doi.org/10.1063/1.3220671

139. Woon, D. E.; Dunning, T. H., Jr. Gaussian Basis Sets for Use in Correlated Molecular Calculations. V. Core-valence Basis Sets for Boron through Neon. *The Journal of Chemical Physics* **1995**, *103* (11), 4572–4585. https://doi.org/10.1063/1.470645

140. Sherrill, C. D.; Leininger, M. L.; Van Huis, T. J.; Schaefer, H. F., III. Structures and Vibrational Frequencies in the Full Configuration Interaction Limit: Predictions for Four Electronic States of Methylene Using a Triple-Zeta plus Double Polarization (TZ2P) Basis. *The Journal of Chemical Physics* **1998**, *108* (3), 1040–1049. https://doi.org/10.1063/1.475465

141. Yang, Y.; Peng, D.; Davidson, E. R.; Yang, W. Singlet–Triplet Energy Gaps for Diradicals from Particle–Particle Random Phase Approximation. *J. Phys. Chem. A* **2015**, *119* (20), 4923–4932. https://doi.org/10.1021/jp512727a

142. Rittby, M.; Bartlett, R. J. An Open-Shell Spin-Restricted Coupled Cluster Method: Application to Ionization Potentials in Nitrogen. *J. Phys. Chem.* **1988**, *92* (11), 3033–3036. https://doi.org/10.1021/j100322a004

143. Kitsaras, M.-P.; Stopkowicz, S. Spin Contamination in MP2 and CC2, a Surprising Issue. *J. Chem. Phys.* **2021**, *154* (13), 131101. https://doi.org/10.1063/5.0044362

144. Jensen, D. S.; Wasserman, A. Numerical Methods for the Inverse Problem of Density Functional Theory. *International Journal of Quantum Chemistry* **2018**, *118* (1), e25425. https://doi.org/10.1002/qua.25425

145. Aryasetiawan, F.; Stott, M. J. Effective Potentials in Density-Functional Theory. *Phys. Rev. B* **1988**, *38* (5), 2974–2987. https://doi.org/10.1103/PhysRevB.38.2974

146. Görling, A. Kohn-Sham Potentials and Wave Functions from Electron Densities. *Phys. Rev. A* **1992**, *46* (7), 3753–3757. https://doi.org/10.1103/PhysRevA.46.3753

147. Zhao, Q.; Parr, R. G. Quantities $T_s[n]$ and $T_c[n]$ in Density-Functional Theory. *Phys. Rev. A* **1992**, *46* (5), 2337–2343. https://doi.org/10.1103/PhysRevA.46.2337

148. Zhao, Q.; Parr, R. G. Constrained-search Method to Determine Electronic Wave Functions from Electronic Densities. *The Journal of Chemical Physics* **1993**, *98* (1), 543–548. https://doi.org/10.1063/1.465093

149. Wang, Y.; Parr, R. G. Construction of Exact Kohn-Sham Orbitals from a given Electron Density. *Phys. Rev. A* **1993**, *47* (3), R1591–R1593. https://doi.org/10.1103/PhysRevA.47.R1591

150. Peirs, K.; Van Neck, D.; Waroquier, M. Algorithm to Derive Exact Exchange-Correlation Potentials from Correlated Densities in Atoms. *Phys. Rev. A* **2003**, *67* (1), 012505. https://doi.org/10.1103/PhysRevA.67.012505

151. Helgaker, T.; Coriani, S.; Jørgensen, P.; Kristensen, K.; Olsen, J.; Ruud, K. Recent Advances in Wave Function-Based Methods of Molecular-Property Calculations. *Chem. Rev.* **2012**, *112* (1), 543–631. https://doi.org/10.1021/cr2002239

152. Sana, M.; Leroy, G.; Wilante, C. Enthalpies of Formation and Bond Energies in Lithium, Beryllium, and Boron Derivatives. A Theoretical Attempt for Data Rationalization. *Organometallics* **1991**, *10* (1), 264–270. https://doi.org/10.1021/om00047a059

153. Bauschlicher, C. W.; Langhoff, S. R. Quantum Mechanical Calculations to Chemical Accuracy. *Science* **1991**, *254* (5030), 394–398. https://doi.org/10.1126/science.254.5030.394

154. Martin, J. M. L. Ab Initio Total Atomization Energies of Small Molecules — towards the Basis Set Limit. *Chemical Physics Letters* **1996**, *259* (5), 669–678. https://doi.org/10.1016/0009-2614(96)00898-6

155. DeYonker, N. J.; Peterson, K. A.; Steyl, G.; Wilson, A. K.; Cundari, T. R. Quantitative Computational Thermochemistry of Transition Metal Species. *J. Phys. Chem. A* **2007**, *111* (44), 11269–11277. https://doi.org/10.1021/jp0715023

156. Jiang, W.; DeYonker, N. J.; Wilson, A. K. Multireference Character for 3d Transition-Metal-Containing Molecules. *J. Chem. Theory Comput.* **2012**, *8* (2), 460–468. https://doi.org/10.1021/ct2006852

157. Bauschlicher, C. W.; Partridge, H. Cr2 Revisited. *Chemical Physics Letters* **1994**, *231* (2), 277–282. https://doi.org/10.1016/0009-2614(94)01243-1

158. Hait, D.; Tubman, N. M.; Levine, D. S.; Whaley, K. B.; Head-Gordon, M. What Levels of Coupled Cluster Theory Are Appropriate for Transition Metal Systems? A Study Using Near-Exact Quantum Chemical Values for 3d Transition Metal Binary Compounds. *J. Chem. Theory Comput.* **2019**, *15* (10), 5370–5385. https://doi.org/10.1021/acs.jctc.9b00674

159. Vogiatzis, K. D.; Ma, D.; Olsen, J.; Gagliardi, L.; de Jong, W. A. Pushing Configuration-Interaction to the Limit: Towards Massively Parallel MCSCF Calculations. *The Journal of Chemical Physics* **2017**, *147* (18), 184111. https://doi.org/10.1063/1.4989858

160. Siegbahn, P. E. M. A New Direct CI Method for Large CI Expansions in a Small Orbital Space. *Chemical Physics Letters* **1984**, *109* (5), 417–423. https://doi.org/10.1016/0009-2614(84)80336-X

161. Knowles, P. J.; Handy, N. C. A New Determinant-Based Full Configuration Interaction Method. *Chemical Physics Letters* **1984**, *111* (4), 315–321. https://doi.org/10.1016/0009-2614(84)85513-X

162. Knowles, P. J.; Handy, N. C. Unlimited Full Configuration Interaction Calculations. *The Journal of Chemical Physics* **1989**, *91* (4), 2396–2398. https://doi.org/10.1063/1.456997

163. Olsen, J.; Jørgensen, P.; Simons, J. Passing the One-Billion Limit in Full Configuration-Interaction (FCI) Calculations. *Chemical Physics Letters* **1990**, *169* (6), 463–472. https://doi.org/10.1016/0009-2614(90)85633-N

164. Süß, D.; Huber, S. E.; Mauracher, A. On the Impact of Multi-Reference Character of Small Transition Metal Compounds on Their Bond Dissociation Energies. *The Journal of Chemical Physics* **2020**, *152* (11), 114104. https://doi.org/10.1063/1.5143495

165. Kállay, M.; Surján, P. R. Higher Excitations in Coupled-Cluster Theory. *J. Chem. Phys.* **2001**, *115* (7), 2945–2954. https://doi.org/10.1063/1.1383290

166. DeYonker, N. J.; Cundari, T. R.; Wilson, A. K. The Correlation Consistent Composite Approach (ccCA): An Alternative to the Gaussian-n Methods. *The Journal of Chemical Physics* **2006**, *124* (11), 114104. https://doi.org/10.1063/1.2173988

167. Karton, A.; Daon, S.; Martin, J. M. L. W4-11: A High-Confidence Benchmark Dataset for Computational Thermochemistry Derived from First-Principles W4 Data. *Chemical Physics Letters* **2011**, *510* (4), 165–178. https://doi.org/10.1016/j.cplett.2011.05.007

168. Jiang, W.; DeYonker, N. J.; Determan, J. J.; Wilson, A. K. Toward Accurate Theoretical Thermochemistry of First Row Transition Metal Complexes. *J. Phys. Chem. A* **2012**, *116* (2), 870–885. https://doi.org/10.1021/jp205710e

169. Karton, A.; Rabinovich, E.; Martin, J. M. L.; Ruscic, B. W4 Theory for Computational Thermochemistry: In Pursuit of Confident Sub-kJ/Mol Predictions. *The Journal of Chemical Physics* **2006**, *125* (14), 144108. https://doi.org/10.1063/1.2348881

170. Fang, Z.; Vasiliu, M.; Peterson, K. A.; Dixon, D. A. Prediction of Bond Dissociation Energies/Heats of Formation for Diatomic Transition Metal Compounds: CCSD(T) Works. *J. Chem. Theory Comput.* **2017**, *13* (3), 1057–1066. https://doi.org/10.1021/acs.jctc.6b00971

171. Feller, D.; Peterson, K. A.; Ruscic, B. Improved Accuracy Benchmarks of Small Molecules Using Correlation Consistent Basis Sets. *Theor Chem Acc* **2013**, *133* (1), 1407. https://doi.org/10.1007/s00214-013-1407-z

172. Dixon, D. A.; Feller, D.; Peterson, K. A. Chapter One - A Practical Guide to Reliable First Principles Computational Thermochemistry Predictions Across the Periodic Table.

In *Annual Reports in Computational Chemistry*; Wheeler, R. A., Ed.; Annual Reports in Computational Chemistry; Elsevier, 2012; Vol. 8, pp 1–28. https://doi.org/10.1016/B978-0-444-59440-2.00001-6

173. Curtiss, L. A.; Raghavachari, K.; Redfern, P. C.; Pople, J. A. Assessment of Gaussian-2 and Density Functional Theories for the Computation of Enthalpies of Formation. *The Journal of Chemical Physics* **1997**, *106* (3), 1063–1079. https://doi.org/10.1063/1.473182
174. Curtiss, L. A.; Redfern, P. C.; Raghavachari, K. Gaussian-4 Theory. *The Journal of Chemical Physics* **2007**, *126* (8), 084108. https://doi.org/10.1063/1.2436888
175. Welch, B. K.; Almeida, N. M. S.; Wilson, A. K. Super ccCA (s-ccCA): An Approach for Accurate Transition Metal Thermochemistry. *Molecular Physics* **2021**, *119* (21–22), e1963001. https://doi.org/10.1080/00268976.2021.1963001
176. Karton, A. Post-CCSD(T) Contributions to Total Atomization Energies in Multireference Systems. *The Journal of Chemical Physics* **2018**, *149* (3), 034102. https://doi.org/10.1063/1.5036795
177. Karton, A. Basis Set Convergence of High-Order Coupled Cluster Methods up to CCSDTQ567 for a Highly Multireference Molecule. *Chemical Physics Letters* **2019**, *737*, 136810. https://doi.org/10.1016/j.cplett.2019.136810
178. Karton, A.; Sylvetsky, N.; Martin, J. M. L. W4-17: A Diverse and High-Confidence Dataset of Atomization Energies for Benchmarking High-Level Electronic Structure Methods. *Journal of Computational Chemistry* **2017**, *38* (24), 2063–2075. https://doi.org/10.1002/jcc.24854
179. Harding, M. E.; Vázquez, J.; Gauss, J.; Stanton, J. F.; Kállay, M. Towards Highly Accurate Ab Initio Thermochemistry of Larger Systems: Benzene. *The Journal of Chemical Physics* **2011**, *135* (4), 044513. https://doi.org/10.1063/1.3609250
180. Sorensen, J. J.; Persinger, T. D.; Sevy, A.; Franchina, J. A.; Johnson, E. L.; Morse, M. D. Bond Dissociation Energies of Diatomic Transition Metal Selenides: TiSe, ZrSe, HfSe, VSe, NbSe, and TaSe. *J. Chem. Phys.* **2016**, *145* (21), 214308. https://doi.org/10.1063/1.4968601
181. Larsson, H. R.; Zhai, H.; Umrigar, C. J.; Chan, G. K.-L. The Chromium Dimer: Closing a Chapter of Quantum Chemistry. *J. Am. Chem. Soc.* **2022**, *144* (35), 15932–15937. https://doi.org/10.1021/jacs.2c06357

182. White, S. R. Density Matrix Formulation for Quantum Renormalization Groups. *Phys. Rev. Lett.* **1992**, *69* (19), 2863–2866. https://doi.org/10.1103/PhysRevLett.69.2863

183. White, S. R.; Huse, D. A. Numerical Renormalization-Group Study of Low-Lying Eigenstates of the Antiferromagnetic S=1 Heisenberg Chain. *Phys. Rev. B* **1993**, *48* (6), 3844–3852. https://doi.org/10.1103/PhysRevB.48.3844

184. Simard, B.; Lebeault-Dorget, M.-A.; Marijnissen, A.; ter Meulen, J. J. Photoionization Spectroscopy of Dichromium and Dimolybdenum: Ionization Potentials and Bond Energies. *The Journal of Chemical Physics* **1998**, *108* (23), 9668–9674. https://doi.org/10.1063/1.476442

185. Ruipérez, F.; Aquilante, F.; Ugalde, J. M.; Infante, I. Complete vs Restricted Active Space Perturbation Theory Calculation of the Cr_2 Potential Energy Surface. *J. Chem. Theory Comput.* **2011**, *7* (6), 1640–1646. https://doi.org/10.1021/ct200048z

186. Celani, P.; Stoll, H.; Werner, H.-J.; Knowles *, P. J. The CIPT2 Method: Coupling of Multi-Reference Configuration Interaction and Multi-Reference Perturbation Theory. Application to the Chromium Dimer. *Molecular Physics* **2004**, *102* (21–22), 2369–2379. https://doi.org/10.1080/00268970412331317788

187. Giner, E.; Scemama, A.; Caffarel, M. Using Perturbatively Selected Configuration Interaction in Quantum Monte Carlo Calculations. *Can. J. Chem.* **2013**, *91* (9), 879–885. https://doi.org/10.1139/cjc-2013-0017

188. Scribano, Y.; Benoit, D. M. Iterative Active-Space Selection for Vibrational Configuration Interaction Calculations Using a Reduced-Coupling VSCF Basis. *Chemical Physics Letters* **2008**, *458* (4), 384–387. https://doi.org/10.1016/j.cplett.2008.05.001

189. Cimiraglia, R. Second Order Perturbation Correction to CI Energies by Use of Diagrammatic Techniques: An Improvement to the CIPSI Algorithm. *The Journal of Chemical Physics* **1985**, *83* (4), 1746–1749. https://doi.org/10.1063/1.449362

190. Dash, M.; Moroni, S.; Filippi, C.; Scemama, A. Tailoring CIPSI Expansions for QMC Calculations of Electronic Excitations: The Case Study of Thiophene. *J. Chem. Theory Comput.* **2021**, *17* (6), 3426–3434. https://doi.org/10.1021/acs.jctc.1c00212

191. Povill, A.; Rubio, J.; Illas, F. Treating Large Intermediate Spaces in the CIPSI Method through a Direct Selected CI Algorithm. *Theoret. Chim. Acta* **1992**, *82* (3), 229–238. https://doi.org/10.1007/BF01113255

192. Park, J. W. Second-Order Orbital Optimization with Large Active Spaces Using Adaptive Sampling Configuration Interaction (ASCI) and Its Application to Molecular Geometry Optimization. *J. Chem. Theory Comput.* **2021**, *17* (3), 1522–1534. https://doi.org/10.1021/acs.jctc.0c01292

193. Lesko, E.; Ardiansyah, M.; Brorsen, K. R. Vibrational Adaptive Sampling Configuration Interaction. *The Journal of Chemical Physics* **2019**, *151* (16), 164103. https://doi.org/10.1063/1.5126510

194. Schriber, J. B.; Evangelista, F. A. Adaptive Configuration Interaction for Computing Challenging Electronic Excited States with Tunable Accuracy. *J. Chem. Theory Comput.* **2017**, *13* (11), 5354–5366. https://doi.org/10.1021/acs.jctc.7b00725

195. Deustua, J. E.; Magoulas, I.; Shen, J.; Piecuch, P. Communication: Approaching Exact Quantum Chemistry by Cluster Analysis of Full Configuration Interaction Quantum Monte Carlo Wave Functions. *The Journal of Chemical Physics* **2018**, *149* (15), 151101. https://doi.org/10.1063/1.5055769

196. Mejuto-Zaera, C.; Tubman, N. M.; Whaley, K. B. Dynamical Mean Field Theory Simulations with the Adaptive Sampling Configuration Interaction Method. *Phys. Rev. B* **2019**, *100* (12), 125165. https://doi.org/10.1103/PhysRevB.100.125165

197. Booth, G. H.; Thom, A. J. W.; Alavi, A. Fermion Monte Carlo without Fixed Nodes: A Game of Life, Death, and Annihilation in Slater Determinant Space. *The Journal of Chemical Physics* **2009**, *131* (5), 054106. https://doi.org/10.1063/1.3193710

198. Blunt, N. S.; Smart, S. D.; Booth, G. H.; Alavi, A. An Excited-State Approach within Full Configuration Interaction Quantum Monte Carlo. *The Journal of Chemical Physics* **2015**, *143* (13), 134117. https://doi.org/10.1063/1.4932595

199. Janssen, C. L.; Nielsen, I. M. B. New Diagnostics for Coupled-Cluster and Møller–Plesset Perturbation Theory. *Chemical Physics Letters* **1998**, *290* (4), 423–430. https://doi.org/10.1016/S0009-2614(98)00504-1

200. Lee, T. J.; Taylor, P. R. A Diagnostic for Determining the Quality of Single-Reference Electron Correlation Methods. *International Journal of Quantum Chemistry* **1989**, *36* (S23), 199–207. https://doi.org/10.1002/qua.560360824

201. Bartel, C. J. Review of Computational Approaches to Predict the Thermodynamic Stability of Inorganic Solids. *J Mater Sci* **2022**, *57* (23), 10475–10498. https://doi.org/10.1007/s10853-022-06915-4

202. Epstein, P. S. The Stark Effect from the Point of View of Schroedinger's Quantum Theory. *Phys. Rev.* **1926**, *28* (4), 695–710. https://doi.org/10.1103/PhysRev.28.695

203. Burton, H. G. A.; Loos, P.-F. Rationale for the Extrapolation Procedure in Selected Configuration Interaction. *J. Chem. Phys.* **2024**, *160* (10), 104102. https://doi.org/10.1063/5.0192458

204. Lesiuk, M.; Jeziorski, B. Complete Basis Set Extrapolation of Electronic Correlation Energies Using the Riemann Zeta Function. *J. Chem. Theory Comput.* **2019**, *15* (10), 5398–5403. https://doi.org/10.1021/acs.jctc.9b00705

205. Puzzarini, C. Extrapolation to the Complete Basis Set Limit of Structural Parameters: Comparison of Different Approaches. *J. Phys. Chem. A* **2009**, *113* (52), 14530–14535. https://doi.org/10.1021/jp9040327

206. Halkier, A.; Helgaker, T.; Jørgensen, P.; Klopper, W.; Koch, H.; Olsen, J.; Wilson, A. K. Basis-Set Convergence in Correlated Calculations on Ne, N_2, and H_2O. *Chemical Physics Letters* **1998**, *286* (3), 243–252. https://doi.org/10.1016/S0009-2614(98)00111-0

207. Truhlar, D. G. Basis-Set Extrapolation. *Chemical Physics Letters* **1998**, *294* (1), 45–48. https://doi.org/10.1016/S0009-2614(98)00866-5

208. Schuchardt, K. L.; Didier, B. T.; Elsethagen, T.; Sun, L.; Gurumoorthi, V.; Chase, J.; Li, J.; Windus, T. L. Basis Set Exchange: A Community Database for Computational Sciences. *J. Chem. Inf. Model.* **2007**, *47* (3), 1045–1052. https://doi.org/10.1021/ci600510j

209. Pritchard, B. P.; Altarawy, D.; Didier, B.; Gibson, T. D.; Windus, T. L. New Basis Set Exchange: An Open, Up-to-Date Resource for the Molecular Sciences Community. *J. Chem. Inf. Model.* **2019**, *59* (11), 4814–4820. https://doi.org/10.1021/acs.jcim.9b00725

210. Feller, D. The Role of Databases in Support of Computational Chemistry Calculations. *Journal of Computational Chemistry* **1996**, *17* (13), 1571–1586.

https://doi.org/10.1002/(SICI)1096-987X(199610)17:13%3C1571::AID-JCC9%3E3.0.CO;2-P

211. Autschbach, J. Perspective: Relativistic Effects. *The Journal of Chemical Physics* **2012**, *136* (15), 150902. https://doi.org/10.1063/1.3702628

212. 212) Liu, W. Ideas of Relativistic Quantum Chemistry. *Molecular Physics* **2010**, *108* (13), 1679–1706. https://doi.org/10.1080/00268971003781571

213. Desclaux, J. P. Relativistic Dirac-Fock Expectation Values for Atoms with $Z = 1$ to $Z = 120$. *Atomic Data and Nuclear Data Tables* **1973**, *12* (4), 311–406. https://doi.org/10.1016/0092-640X(73)90020-X

214. Kutzelnigg, W.; Liu, W. Quasirelativistic Theory Equivalent to Fully Relativistic Theory. *The Journal of Chemical Physics* **2005**, *123* (24), 241102. https://doi.org/10.1063/1.2137315

215. Kutzelnigg, W.; Liu, W. Quasirelativistic Theory I. Theory in Terms of a Quasi-Relativistic Operator. *Molecular Physics* **2006**, *104* (13–14), 2225–2240. https://doi.org/10.1080/00268970600662481

216. Liu, W.; Kutzelnigg, W. Quasirelativistic Theory. II. Theory at Matrix Level. *The Journal of Chemical Physics* **2007**, *126* (11), 114107. https://doi.org/10.1063/1.2710258

217. Carreras, A.; Jiang, H.; Pokhilko, P.; Krylov, A. I.; Zimmerman, P. M.; Casanova, D. Calculation of Spin–Orbit Couplings Using RASCI Spinless One-Particle Density Matrices: Theory and Applications. *J. Chem. Phys.* **2020**, *153* (21), 214107. https://doi.org/10.1063/5.0029146

218. Peterson, K. A.; Dunning, T. H., Jr. Accurate Correlation Consistent Basis Sets for Molecular Core–Valence Correlation Effects: The Second Row Atoms Al–Ar, and the First Row Atoms B–Ne Revisited. *The Journal of Chemical Physics* **2002**, *117* (23), 10548–10560. https://doi.org/10.1063/1.1520138

219. Balabanov, N. B.; Peterson, K. A. Systematically Convergent Basis Sets for Transition Metals. I. All-Electron Correlation Consistent Basis Sets for the 3d Elements Sc–Zn. *J. Chem. Phys.* **2005**, *123* (6), 064107. https://doi.org/10.1063/1.1998907

220. Dunning, T. H. Gaussian Basis Sets for Use in Correlated Molecular Calculations. I. The Atoms Boron through Neon and Hydrogen. *J. Chem. Phys.* **1989**, *90* (2), 1007–1023. https://doi.org/10.1063/1.456153

221. Woon, D. E.; Dunning, T. H. Gaussian Basis Sets for Use in Correlated Molecular Calculations. III. The Atoms Aluminum through Argon. *J. Chem. Phys.* **1993**, *98* (2), 1358–1371. https://doi.org/10.1063/1.464303

222. Okoshi, M.; Atsumi, T.; Nakai, H. Revisiting the Extrapolation of Correlation Energies to Complete Basis Set Limit. *Journal of Computational Chemistry* **2015**, *36* (14), 1075–1082. https://doi.org/10.1002/jcc.23896

223. Repisky, M.; Komorovsky, S.; Konecny, L.; Kadek, M.; Moitra, T.; Joosten, M.; Misenkova, D.; Vikhamar-Sandberg, R.; Kaupp, M.; Ruud, K.; Malkina, O. L.; Malkin, V. G. X2C Hamiltonian Models in ReSpect: Bridging Accuracy and Efficiency. *J. Phys. Chem. A* **2025**, *129* (34), 7980–7998. https://doi.org/10.1021/acs.jpca.5c02990

224. Surjuse, K. A.; Valeev, E. F. *SAP-X2C: Optimally-Simple Two-Component Relativistic Hamiltonian With Size-Intensive Picture Change*. *arXiv* **2026**. https://arxiv.org/abs/2601.04174v2

225. Lodi, L.; Yurchenko, S. N.; Tennyson, J. The Calculated Rovibronic Spectrum of Scandium Hydride, ScH. *Molecular Physics* **2015**, *113* (13–14), 1998–2011. https://doi.org/10.1080/00268976.2015.1029996

226. Guo, J.; Goodings, J. M. Scandium Ionization Mechanisms in H_2–O_2–N_2 Flames Supported by Calculated Thermodynamic Data. *International Journal of Mass Spectrometry* **2002**, *214* (3), 339–348. https://doi.org/10.1016/S1387-3806(02)00525-0

227. Matsika, S. Electronic Structure Methods for the Description of Nonadiabatic Effects and Conical Intersections. *Chem. Rev.* **2021**, *121* (15), 9407–9449. https://doi.org/10.1021/acs.chemrev.1c00074

228. Yarkony, D. R. Diabolical Conical Intersections. *Rev. Mod. Phys.* **1996**, *68* (4), 985–1013. https://doi.org/10.1103/RevModPhys.68.985

229. Dreuw, A.; Head-Gordon, M. Single-Reference Ab Initio Methods for the Calculation of Excited States of Large Molecules. *Chem. Rev.* **2005**, *105* (11), 4009–4037. https://doi.org/10.1021/cr0505627

230. Hättig, C. Structure Optimizations for Excited States with Correlated Second-Order Methods: CC2 and ADC(2). In *Advances in Quantum Chemistry*; Academic Press, 2005; Vol. 50, pp 37–60. https://doi.org/10.1016/S0065-3276(05)50003-0

231. Levine, B. G.; Ko, C.; Quenneville, J.; MartÍnez, T. J. Conical Intersections and Double Excitations in Time-Dependent Density Functional Theory. *Molecular Physics* **2006**, *104* (5–7), 1039–1051. https://doi.org/10.1080/00268970500417762

232. Cordova, F.; Doriol, L. J.; Ipatov, A.; Casida, M. E.; Filippi, C.; Vela, A. Troubleshooting Time-Dependent Density-Functional Theory for Photochemical Applications: Oxirane. *J. Chem. Phys.* **2007**, *127* (16), 164111. https://doi.org/10.1063/1.2786997

233. Gozem, S.; Melaccio, F.; Valentini, A.; Filatov, M.; Huix-Rotllant, M.; Ferré, N.; Frutos, L. M.; Angeli, C.; Krylov, A. I.; Granovsky, A. A. et al. Shape of Multireference, Equation-of-Motion Coupled-Cluster, and Density Functional Theory Potential Energy Surfaces at a Conical Intersection. *J. Chem. Theory Comput.* **2014**, *10* (8), 3074–3084. https://doi.org/10.1021/ct500154k

234. Casida, M. E.; Huix-Rotllant, M. Progress in Time-Dependent Density-Functional Theory. *Annual Review of Physical Chemistry* **2012**, *63*, 287–323. https://doi.org/10.1146/annurev-physchem-032511-143803

235. Yang, Y.; Shen, L.; Zhang, D.; Yang, W. Conical Intersections from Particle–Particle Random Phase and Tamm–Dancoff Approximations. *J. Phys. Chem. Lett.* **2016**, *7* (13), 2407–2411. https://doi.org/10.1021/acs.jpclett.6b00936

236. Gross, E. K. U.; Oliveira, L. N.; Kohn, W. Density-Functional Theory for Ensembles of Fractionally Occupied States. I. Basic Formalism. *Phys. Rev. A* **1988**, *37* (8), 2809–2820. https://doi.org/10.1103/PhysRevA.37.2809

237. Filatov, M.; Shaik, S. A Spin-Restricted Ensemble-Referenced Kohn–Sham Method and Its Application to Diradicaloid Situations. *Chemical Physics Letters* **1999**, *304* (5), 429–437. https://doi.org/10.1016/S0009-2614(99)00336-X

238. Li, S. L.; Marenich, A. V.; Xu, X.; Truhlar, D. G. Configuration Interaction-Corrected Tamm–Dancoff Approximation: A Time-Dependent Density Functional Method with the Correct Dimensionality of Conical Intersections. *J. Phys. Chem. Lett.* **2014**, *5* (2), 322–328. https://doi.org/10.1021/jz402549p

239. Shu, Y.; Parker, K. A.; Truhlar, D. G. Dual-Functional Tamm–Dancoff Approximation: A Convenient Density Functional Method That Correctly Describes S1/S0 Conical

Intersections. *J. Phys. Chem. Lett.* **2017**, *8* (10), 2107–2112. https://doi.org/10.1021/acs.jpclett.7b00594

240. Bannwarth, C.; Yu, J. K.; Hohenstein, E. G.; Martínez, T. J. Hole–Hole Tamm–Dancoff-Approximated Density Functional Theory: A Highly Efficient Electronic Structure Method Incorporating Dynamic and Static Correlation. *J. Chem. Phys.* **2020**, *153* (2), 024110. https://doi.org/10.1063/5.0003985
241. Runge, E.; Gross, E. K. U. Density-Functional Theory for Time-Dependent Systems. *Phys. Rev. Lett.* **1984**, *52* (12), 997–1000. https://doi.org/10.1103/PhysRevLett.52.997
242. Fukushima, K. Excited-State Theorem in Both Case of a Nuclear Potential and a More General External Potential in Correspondence to the Hohenberg-Kohn Theorem. *Journal of Physics and Chemistry of Solids* **2022**, *161*, 110406. https://doi.org/10.1016/j.jpcs.2021.110406
243. Ospadov, E.; Ryabinkin, I. G.; Staroverov, V. N. Improved Method for Generating Exchange-Correlation Potentials from Electronic Wave Functions. *J. Chem. Phys.* **2017**, *146* (8), 084103. https://doi.org/10.1063/1.4975990
244. Cuevas-Saavedra, R.; Ayers, P. W.; Staroverov, V. N. Kohn–Sham Exchange-Correlation Potentials from Second-Order Reduced Density Matrices. *J. Chem. Phys.* **2015**, *143* (24), 244116. https://doi.org/10.1063/1.4937943
245. Levy, M. Electron Densities in Search of Hamiltonians. *Phys. Rev. A* **1982**, *26* (3), 1200–1208. https://doi.org/10.1103/PhysRevA.26.1200
246. Lieb, E. H. Density Functionals for Coulomb Systems. *International Journal of Quantum Chemistry* **1983**, *24* (3), 243–277. https://doi.org/10.1002/qua.560240302
247. Ospadov, E.; Tao, J.; Staroverov, V. N.; Perdew, J. P. Visualizing Atomic Sizes and Molecular Shapes with the Classical Turning Surface of the Kohn–Sham Potential. *Proceedings of the National Academy of Sciences* **2018**, *115* (50), E11578–E11585. https://doi.org/10.1073/pnas.1814300115
248. Kaplan, A. D.; Clark, S. J.; Burke, K.; Perdew, J. P. Calculation and Interpretation of Classical Turning Surfaces in Solids. *npj Comput Mater* **2021**, *7* (1), 25. https://doi.org/10.1038/s41524-020-00479-0

249. Gould, T.; Liberles, B. T.; Perdew, J. P. What Do We Learn from the Classical Turning Surface of the Kohn–Sham Potential as Electron Number Is Varied Continuously? *J. Chem. Phys.* **2020**, *152* (5), 054105. https://doi.org/10.1063/1.5130693

250. Mead, C. A.; Truhlar, D. G. On the Determination of Born–Oppenheimer Nuclear Motion Wave Functions Including Complications Due to Conical Intersections and Identical Nuclei. *J. Chem. Phys.* **1979**, *70* (5), 2284–2296. https://doi.org/10.1063/1.437734

251. Varandas, A. J. C.; Brown, F. B.; Mead, C. A.; Truhlar, D. G.; Blais, N. C. A Double Many-body Expansion of the Two Lowest-energy Potential Surfaces and Nonadiabatic Coupling for H3. *J. Chem. Phys.* **1987**, *86* (11), 6258–6269. https://doi.org/10.1063/1.452463

252. Boothroyd, A. I.; Keogh, W. J.; Martin, P. G.; Peterson, M. R. A Refined H_3 Potential Energy Surface. *J. Chem. Phys.* **1996**, *104* (18), 7139–7152. https://doi.org/10.1063/1.471430

253. Kendrick, B. K. Geometric Phase Effects in Chemical Reaction Dynamics and Molecular Spectra. *J. Phys. Chem. A* **2003**, *107* (35), 6739–6756. https://doi.org/10.1021/jp021865x

254. Juanes-Marcos, J. C.; Althorpe, S. C. Geometric Phase Effects in the $H+H_2$ Reaction: Quantum Wave-Packet Calculations of Integral and Differential Cross Sections. *J. Chem. Phys.* **2005**, *122* (20), 204324. https://doi.org/10.1063/1.1924411

255. Henck, S. A.; Mason, M. A.; Yan, W.; Lehmann, K. K.; Coy, S. L. Microwave Detected, Microwave-optical Double Resonance of NH_3, NH_2D, NHD_2, and ND_3. II. Predissociation Dynamics of the Ã State. *J. Chem. Phys.* **1995**, *102* (12), 4783–4792. https://doi.org/10.1063/1.469526

256. Yarkony, D. R. Exploring Molecular Complexity: Conical Intersections and NH_3 Photodissociation. *J. Chem. Phys.* **2004**, *121* (2), 628–631. https://doi.org/10.1063/1.1772351

257. Wells, K. L.; Perriam, G.; Stavros, V. G. Time-Resolved Velocity Map Ion Imaging Study of NH_3 Photodissociation. *J. Chem. Phys.* **2009**, *130* (7), 074308. https://doi.org/10.1063/1.3072763

258. Zhu, X.; Yarkony, D. R. On the Construction of Property Based Diabatizations: Diabolical Singular Points. *J. Phys. Chem. A* **2015**, *119* (50), 12383–12391. https://doi.org/10.1021/acs.jpca.5b07705

259. Wang, Y.; Guan, Y.; Guo, H.; Yarkony, D. R. Enabling Complete Multichannel Nonadiabatic Dynamics: A Global Representation of the Two-Channel Coupled, $1,2^1A$ and 1^3A States of NH_3 Using Neural Networks. *J. Chem. Phys.* **2021**, *154* (9), 094121. https://doi.org/10.1063/5.0037684

260. Gozem, S.; Krylov, A. I.; Olivucci, M. Conical Intersection and Potential Energy Surface Features of a Model Retinal Chromophore: Comparison of EOM-CC and Multireference Methods. *J. Chem. Theory Comput.* **2013**, *9* (1), 284–292. https://doi.org/10.1021/ct300759z

261. Gozem, S.; Melaccio, F.; Lindh, R.; Krylov, A. I.; Granovsky, A. A.; Angeli, C.; Olivucci, M. Mapping the Excited State Potential Energy Surface of a Retinal Chromophore Model with Multireference and Equation-of-Motion Coupled-Cluster Methods. *J. Chem. Theory Comput.* **2013**, *9* (10), 4495–4506. https://doi.org/10.1021/ct400460h

262. Gozem, S.; Luk, H. L.; Schapiro, I.; Olivucci, M. Theory and Simulation of the Ultrafast Double-Bond Isomerization of Biological Chromophores. *Chem. Rev.* **2017**, *117* (22), 13502–13565. https://doi.org/10.1021/acs.chemrev.7b00177